The Development of a Small Diesel Engine Test Bench Employing an Electric Dynamometer

by
Eben Grobbelaar

Thesis presented in partial fulfilment of the requirements for the degree of Master of Engineering (Mechanical) in the Faculty of Engineering at Stellenbosch University

Supervisor: Mr Richard Walter Haines

March 2017

DECLARATION

By submitting this thesis electronically, I declare that the entirety of the work contained therein is my own, original work, that I am the sole author thereof (save to the extent explicitly otherwise stated), that reproduction and publication thereof by Stellenbosch University will not infringe any third party rights and that I have not previously in its entirety or in part submitted it for obtaining any qualification.

Date: March 2017

Abstract

Global efforts to combat climate change, reduce greenhouse gas emissions and increase energy security has led to renewed interest in the use of biofuels as an alternative to fossil fuels. Therefore, it has become increasingly important to understand the effects that the use of biofuel has on the performance and emissions of internal combustion engines. The subject of this report is the development of a small diesel engine test bench employing an electric dynamometer. The purpose of the project is to establish an engine testing platform which can be used to test small quantities of biofuel, as well as to expand the testing capabilities of the Biofuel Test Facility at Stellenbosch University. In this report, a review of the literature surrounding various aspects of engine performance testing and engine indicating testing is presented. In addition, literature research regarding the different types of dynamometers available is also presented. A thorough evaluation of the various dynamometer options is performed and a suitable electric dynamometer system is selected for the development of the test bench. Further aspects surrounding the development of the test bench covered in this report include integrating the dynamometer with a small test bench employing a single-cylinder, compression-ignition engine, designing a driveshaft to couple the dynamometer to the test engine, as well as instrumenting the test bench. In addition, this report also details the instrumentation of the test engine with a fibre-optic pressure transducer to measure in-cylinder pressure data, as well as the development of software which is used to measure and record all engine indicating data. The obtained engine indicating data is then used to construct a zero-dimensional, single-zone heat release model. Calibration of the dynamometer system is performed and it is concluded that the dynamometer's signal output exhibits excellent repeatability and displays very little hysteresis. Engine tests are also performed during which it is found that the developed test bench produces accurate and repeatable results, both during engine performance testing and engine indicating testing. It is also concluded that the test setup is sensitive enough to detect small changes in engine performance and engine particulate emissions when switching from petroleum diesel to B10 biodiesel.

Opsomming

Globale pogings om klimaatsverandering te bestry, vrystelling van kweekhuisgasse te verminder en energie sekuriteit te verhoog, het gelei tot hernude belangstelling in die gebruik van biobrandstowwe as 'n alternatief vir fossielbrandstowwe. Gevolglik het dit al hoe belangriker geword om die effek wat die gebruik van biobrandstof op die werkverrigting en uitlaatgasse van binnebrandenjins het te verstaan. Die onderwerp van hierdie verslag is die ontwikkeling van 'n klein dieselenjin toetsbank wat gebruik maak van 'n elektriese enjin rem. Die doel van hierdie projek is om 'n enjin toets platform te ontwikkel wat gebruik kan word om klein hoeveelhede biobrandstof te toets, asook om die toets vermoë van die Biobrandstof Toetsfasiliteit by die Universiteit van Stellenbosch uit te brei. Hierdie verslag verskaf ‘n oorsig van die literatuur wat handel oor die verskeie aspekte van enjin prestasietoetsing, sowel as oor die meting van druk binne die silinder van ‘n enjin. Daarbenewens word literatuurnavorsing oor verskillende tipes enjin remme ook aangebied. 'n Deeglike evaluering van die verskillende enjin rem opsies word gedoen en die mees geskikte elektriese enjin rem stelsel word gekies vir implementering met die toetsbank. Addisionele aspekte rakende die ontwikkeling van die toets bank wat in hierdie verslag aangespreek word sluit in die integrasie van die enjin rem met ‘n beskikbare klein toets bank wat gebruik maak van ‘n enkel-silinder, kompressie-ontstekingsenjin, die ontwerp van 'n dryfas om die enjin rem aan die toets enjin te koppel, sowel as die instrumenting van die toets bank. Verder word besonderhede ook verskaf rondom die instrumentering van die toets enjin met 'n optiese-vesel druk sensor om gevolglik die druk binne die enjin silinder te meet. Die ontwikkeling van die sagteware, wat gebruik word om hierdie gemete druk waardes te stoor, word ook bespreek. Die druk waardes gemeet binne die silinder van die enjin word dan gebruik om 'n nul-dimensionele, enkel-area numeriese model te ontwikkel wat beskryf hoe hitte binne die enjin vrygestel word. Kalibrasie van die enjin rem stelsel word uitgevoer waartydens daar gevind word dat die uittree sein vanaf die enjin rem uitstekende herhaalbaarheid en baie min histerese toon. Enjin toetse word ook uitgevoer waartydens daar bevind word dat die ontwikkelde toets bank baie akkurate en herhaalbare resultate oplewer tydens beide die enjin prestasie toetse sowel as tydens die meet van die silinder druk. Daar word ook tot die gevolgtrekking gekom dat die toets opstelling sensitief genoeg is om klein veranderinge in enjin werkverrigting en enjin uitlaatgasse te identifiseer, wanneer daar vanaf petroleum diesel na B10 biodiesel oorgeskakel word.

Acknowledgements

The author wishes to thank:

- Mr R.W. Haines for his continuous support and guidance throughout this project.
- Mr F. Zietsman and the rest of the personnel at the Department of Mechanical and Mechatronic Engineering workshop for the manufacturing of the designed components.
- Mr G. Lourens from Sasol Advanced Fuels Laboratory for his assistance in setting up the PLC for the dynamometer.
- The Centre for Renewable and Sustainable Energy Studies (CRSES) for the bursary funding which they contributed towards the project.

Table of Contents

List of Figures

List of Tables

Nomenclature

Variables

b	Keyway width
D	Cylinder bore
d	Driveshaft diameter
E	Modulus of elasticity
f	Frequency
H	Dynamic amplifier
h	Instantaneous heat transfer coefficient
l	Connecting rod length
M	Bending moment
m	Mass of cylinder contents
n	Rotational speed
P	Pressure
q	Notch sensitivity (bending)
Re	Reynolds number
r	Fillet radius (keyway)
T	Mean temperature of cylinder charge
t	Keyway depth
V	In-cylinder volume
W	Work
y	Piston displacement from top dead centre
α	Crankshaft angle measured from vertical
γ	Specific heat ratio
θ	Crank angle
ν	Poisson's ratio
ρ	Density
σ	Stefan-Boltzmann constant
τ	Shear stress
$\emptyset$	Oscillation (deflection) of shaft under torsion

Variables with superscripts

R^2	Coefficient of determination
σ'	Maximum von Mises stress

Variables with subscripts

A_s	Instantaneous combustion chamber surface area
A_w	Combustion chamber wall area
C_s	Shaft stiffness
c_p	Specific heat at constant pressure
c_v	Specific heat at constant volume
F_{By}	Force at point B in y-direction
F_G	Gravitational force on driveshaft
F_s	Shear force
f_c	Critical frequency
f_e	Electrical frequency
H_c	Dynamic amplifier at critical frequency
h_{cr}	Enthalpy of flow into and out of crevices
h_f	Sensible enthalpy of fuel injected
$IMEP_{gross}$	Indicated mean effective pressure (gross)
K_1	Service factor (driving machine)
K_2	Service factor (driven machine)
K_f	Fatigue stress concentration factor (bending)
K_{fs}	Fatigue stress concentration factor (shear)
K_t	Bending stress concentration factor
K_{ts}	Shear stress concentration factor
k_a	Surface factor
k_b	Size factor
k_c	Loading factor
k_d	Temperature factor
k_e	Reliability factor
k_f	Miscellaneous effects factor

k_g	Thermal conductivity of combustion gas
M_a	Bending moment (alternating component)
M_m	Bending moment (midrange component)
m_f	Mass of fuel injected
m_{cr}	Mass of charge entering crevice region
m_s	Mass of driveshaft
m_f	Mass of fuel injected
m_B	Mass supported by driveshaft at point B
N_p	Number of poles
n_F	Fatigue factor of safety
n_{fc}	Factor of safety (flexible coupling)
n_p	Polytropic constant
n_{ts}	Factor of safety (torque spikes)
n_{sync}	Synchronous speed
n_{yield}	Factor of safety (yield)
$P_{E,max}$	Maximum power output of test engine
P_{IBDC}	Pressure at intake bottom dead centre
P_m	Cylinder pressure of motored engine
P_{max}	Maximum pressure
P_r	Reference pressure
Q_{ch}	Chemical energy
Q_{LHV}	Lower heating value
Q_w	Heat transferred to cylinder wall
q_s	Notch sensitivity (shear)
R_{Ay}	Reaction force at point A in y-direction
R_{Cy}	Reaction force at point C in y-direction
R_p	Radius to the crank pin
r_c	Compression ratio
S_e	Endurance limit
$S_{e'}$	Endurance limit of the rotating test specimen

S_F	Service factor
S_{ut}	Ultimate tensile strength
S_y	Yield strength
T_A	Torque at point A
T_a	Torque (alternating component)
T_B	Torque at point B
T_m	Torque (midrange component)
T_{design}	Design torque
T_{dyno}	Torque measured by dynamometer
$T_{E,max}$	Maximum nominal torque output of test engine
T_{ex}	Excitation torque
$T_{F,max}$	Maximum torque rating of flexible coupling
$T_{F,nom}$	Nominal torque rating of flexible coupling
T_g	Instantaneous bulk gas temperature
T_r	Reference temperature
T_w	Mean surface temperature of combustion chamber wall
T_x	Torque applied
U_s	Sensible internal energy
u	Internal energy
V_r	Reference volume
V_s	Swept volume
v_p	Mean piston speed
$W_{i,net}$	Indicated work (net)
$W_{i,gross}$	Indicated work (gross)
W_p	Pumping work
$\sigma_{von\ Mises}$	Von Mises stress due to pure shear
$\emptyset_0$	Static deflection of shaft under torsion

Acronyms

AB	Allen-Bradley
AC	Alternating current
BDC	Bottom dead centre
BMEP	Brake mean effective pressure
BSFC	Brake specific fuel consumption
CHR	Cumulative heat release
CI	Compression-ignition
DC	Direct current
DI	Direct-injection
EOI	End of injection
ETA	Engine test automation
FEA	Finite element analysis
FMEP	Friction mean effective pressure
FSN	Filter smoke number
GUI	Graphical user interface
IBDC	Intake bottom dead centre
IMEP	Indicated mean effective pressure
LED	Light-emitting diode
MAP	Manifold Absolute Pressure
NI	National instruments
PLC	Programmable logic controller
ROHR	Rate of heat release
SCADA	Supervisory control and data acquisition
SOC	Start of combustion
SOI	Start of injection
TDC	Top dead centre
VI	Virtual instrument
VSD	Variable speed drive

1 Introduction

The constant increase in the global demand for fossil fuels (BP Statistical Review of World Energy, 2016), coupled with the continued depletion of limited fossil fuel reserves, continues to emphasise the need to find alternative fuel resources. This has sparked renewed interest in the use of biofuels, such as biodiesel, as an alternative to fossil fuels (Huang *et al.* 2012).

Additional factors such as the global efforts to combat climate change reduce greenhouse gas emissions and increase energy security (EPA, 2015) has renewed interest in the use of biofuels. This has led to Congress in the United States implementing programs such as the Renewable Fuel Standard program, which mandates that, per annum, a minimum volume of biofuel must be blended into all transportation fuel sold in the United States. The amount of biofuel introduced in this manner is to be increased each year as stipulated by the annual percentage standards published by the United States Environmental Protection Agency (EPA, 2015).

In South Africa, a Biofuels Industrial Strategy was also submitted to Cabinet in 2007. This strategy's aim was to achieve a 2 % biofuel penetration level into all liquid based fuel sold in the country (Biofuels Industrial Strategy of the Republic of South Africa, 2007). With steps being taken both locally and internationally to promote the use of biofuel, it has become increasing important to study the effects that the use of biofuel has on the performance and emissions of internal combustion (IC) engines.

The Department of Process Engineering at Stellenbosch University already has the capability to produce their own biofuel, but only in small quantities at a time. However, prior to this project, Stellenbosch University's Biofuel Test Facility did not have a test setup which could operate on such small quantities of fuel and could therefore not test the biofuel. There was thus a need to develop a small diesel engine test bench capable of performing fuel-to-fuel evaluations on these small quantities of fuel. The addition of a small diesel engine test setup would also significantly expand the testing capability of the entire test facility. The purpose of this project was thus to develop such a small diesel engine test bench employing a suitable dynamometer system.

The objectives for this project were the following:

- Research and select a suitable dynamometer system (with consideration of future research requirements) for the small diesel engine test bench being developed.
- Integrate the selected dynamometer system with an existing test bench in Stellenbosch University's Biofuel Test Facility.
- Instrument the test bench to measure engine performance, as well as monitor various engine operating parameters.
- Instrument the test engine and develop the required software to enable engine indicating testing to be performed.

- Commission the test setup and validate that the test setup is capable of producing accurate and repeatable results.

2 Literature Study

During the initial stages of the project, a preliminary literature study was performed. This was done in order to determine what research have already been conducted using small capacity compression-ignition engines for biofuel testing. The literature study was then continued to research the various types of dynamometer options available in order to identify a suitable dynamometer system for the test bench being developed. Throughout the duration of the project various aspects surrounding engine testing hardware, engine performance testing and engine indicating testing were researched. Research was also performed regarding combustion analysis of a compression-ignition engine, as well as the development of a heat release model using in-cylinder pressure data.

2.1 Engine testing

The primary aim of engine testing is to measure and compare engine performance at different states of tune. Furthermore, engine testing is also used to compare the performance of different engines when subjected to the same test conditions (Atkins, 2009). Due to the automotive industry's constant commitment towards product development, engine manufacturers continually perform rigorous engine testing, as part of their research and development programmes (Dynamometer Engine Testing, 2011). Whenever engine developers implement new engine technology, an appropriate type of engine test is used to verify the performance of the modified engine or engine components. The newly developed technology can therefore be tested prior to it being mass produced (a benefit of engine testing which greatly reduces the cost of engine development) (Engine Testing Overview, [S.a.]). As opposed to road testing, engine testing quantifies and isolates engine performance parameters from vehicle performance. This enables engine developers to determine exactly what engine modifications lead to improved engine performance, resulting in considerable less testing time (Why You Need an Engine Dynamometer, [S.a.]).

Some form of engine testing almost always forms part of the engine manufacturing process, where engine testing is primarily implemented in the form of either a hot or a cold test. A cold test is normally performed on a near complete engine and employs a cold test rig situated within the assembly line. The purpose of the cold test is to confirm the satisfactory performance of a specific subassembly of the complete engine. A hot test, on the other hand, is generally performed within an engine production test cell and on a complete engine. Here, the aim of the test is to establish (in the shortest amount of time possible) if the engine is complete and runs (Martyr & Plint, 2007).

Apart from the types of engine testing mentioned above, there are numerous other applications of engine testing. Some of the most common types of engine testing

performed include: durability testing, engine performance testing, fuel and lubrication testing, engine emissions testing and exhaust system testing (Atkins, 2009).

2.2 Engine test facilities

Complicated engine test procedures require the strict control of various parameters such as temperatures, pressures, flow rates, etc. In order to conduct these engine tests, a very sophisticated facility is required that houses the advanced testing equipment and instrumentation required to measure engine performance. However, in general, these engine test facilities vary considerably in performance, size and power rating (Martyr & Plint, 2007).

In addition to the instrumentation employed in the engine test facility, the facility must also house the support services and utilities required by the instrumentation. The support services aid in ensuring that the instrumentation performs as expected and that reliable data can be obtained. Typical support services required in the test facility are proper ventilation, cooling water, conditioning systems for fuel, water and exhaust gases, an exhaust gas extraction system and a fuel supply system. Although the aforementioned services are vital to ensure proper operation of the test facility, one of the most important aspects of an engine test facility is ensuring that the proper safety measures are employed. From a safety point of view, additional items such as: emergency lighting and power, a fire suppression system, fire alarms, fire extinguishers, appropriate warning lights and a safe fuel storage area should also be provided by the test facility (Atkins, 2009).

Employing the appropriate safety measures are of particular importance when it comes to the handling and storage of biofuels. Biodiesel and biodiesel blends, for example, tend to be hydrophilic. This leads to the corrosion of fuel lines and storage tanks, due to the condensation of the water contained in the fuel. Furthermore, when biodiesel blends are stored in bulk or in drums for extended periods of time, the additional water absorbed by the fuel leads to increased microbial growth in heated fuel tanks. These growths then form soft masses that plug the filters in the fuel system (Martyr & Plint, 2007).

2.3 Engine test benches

The piece of equipment most central to the engine test facility, as well as to the engine testing procedure itself, is the engine test bench. The primary function of the test bench being to facilitate the mounting of the unit under test, as well as to support all other equipment required to perform the relevant tests. Generally, the design of the test bench varies according to the type of engine test being performed.

General-purpose automotive engine test cells often employ a common tee-slotted bedplate design, which offers maximum flexibility in that it allows both the position of the dynamometer and the engine to be adjusted. When performing hot

and cold tests in an engine production environment, the primary concern is that the test bench used must permit fast engine changeovers. Such a test bench only needs to offer limited flexibility in terms of the mounting arrangements that it supports. For research and development purposes, it is also often required that the test bench makes special provision for the mounting of additional equipment also included in the test procedure. One such example is powertrain testing where the engine is tested along with its directly mounted transmission (Martyr & Plint, 2007).

In addition to the above, the test bench must also be able to withstand the forces imposed upon it by the equipment that it supports. This includes the static forces, due to the weight of the equipment, as well as any dynamic forces generated during the engine test procedure. This requirement generally leads to test benches being very strong and rigidly designed. Provision must, however, still be made for the test bench to be able to absorb as much engine vibration as possible. This is of particular importance when measurements are taken using instrumentation that is mounted directly to the test bench, since any vibration present at the measurement position will show up as noise in the measured data. Special provisions must therefore be made to ensure that the measurement equipment is isolated from excessive vibration. Generally, this can be accomplished by mounting either the engine, or the measurement equipment, on anti-vibration mountings.

Furthermore, the test bench must also employ the necessary safety measures in order to allow the engine testing procedure to be performed safely. All components of the test setup that pose risk of injury should be covered by a safety enclosure or clearly marked with a warning sign if it is not possible to enclose it. Apart from preventing accessibility to the danger zone, these safety covers must also be strong enough to contain the mechanical components of the tests setup in the event that a catastrophic failure should occur during the testing procedure.

2.4 Dynamometers and torque measurement

Second to the engine being tested, the dynamometer can be considered the most important piece of equipment used in the engine testing procedure. The function of the dynamometer is to resist and measure the torque generated by the prime mover to which it is connected. Ideally, the dynamometer should be able to impose variable loading on the engine, while the engine is operated over its entire speed and torque range (Atkins, 2009). Furthermore, the accuracy with which the dynamometer measures both the speed and torque of the engine being tested is vital to all other derived measurements made during the engine testing procedure (Martyr & Plint, 2007). In order to obtain satisfactory results, an appropriate dynamometer must thus be selected that best suits the type of engine testing to be performed.

2.4.1 Dynamometer classification

The two main types of dynamometers used in engine testing are engine dynamometers and chassis dynamometers. An engine dynamometer connects to the crankshaft (or flywheel) of an engine (by means of a driveshaft) and measures the torque developed by the engine alone. A chassis dynamometer, on the other hand, consists of rollers that are driven by the wheels of the vehicle being tested and consequently measures the torque available at the wheels of the vehicle (Shaw, [S.a.]). The discussion which follows will focus on the various types of engine dynamometers encountered most often in practice.

An engine dynamometer can be classified as either being an active or a passive dynamometer. A dynamometer that is only capable of absorbing power is known as an absorption or passive dynamometer. Dynamometers can, however, also be used to measure the amount of power required to operate a driven machine. Such a dynamometer, capable of both absorbing power as well as driving a machine, is known as a universal or active dynamometer (Dynamometer Review, [S.a.]). The various types of dynamometer can be distinguished from each other, based on the way in which they absorb the torque that is applied to them. Even though there are a wide variety of engine dynamometers in use today, the majority of these engine dynamometers can be classified according to two main categories, namely: hydraulic dynamometers and electric dynamometers.

2.4.2 Hydraulic dynamometers

Hydraulic dynamometers have the capability to absorb very large amounts of power as well as to absorb power at very high speeds. The design of the hydraulic dynamometer (also referred to as a water-brake dynamometer) consists of a rotor (attached to a rotating driveshaft) into which semi-elliptical pockets have been machined. Similar pockets have also been machined into the watertight casing within which the rotor rotates and together these pockets form elliptical receptacles. The pockets in the rotor, as well as those in the casing of the dynamometer, are separated from each other with radial vanes, which are set at an angle to the shaft of the rotor (Martyr & Plint, 2007). The rotor shaft is supported by bearings that are located in the dynamometer casing, which in turn is carried by trunnion bearings. This means that the casing of the dynamometer is free to rotate about the same axis as the rotor shaft (Atkins, 2009).

During operation, the rotor shaft is connected to the crankshaft of the engine and the casing of the dynamometer is filled with water. As the rotor rotates in the water filled casing of the dynamometer, water is discharged from the rotor pockets into the pockets in the dynamometer's casing. From here, the water is returned at reduced speed to again enter the pockets in the rotor. It is this shearing of the water that leads to a resistance of rotation of the rotor, which in turn, causes the dynamometer casing to experience a torque reaction. This torque reaction causes the dynamometer casing to pivot on its trunnion bearings (Atkins, 2009). The torque reaction experienced by the dynamometer can then be calculated by attaching a lever arm of known length to the dynamometer's casing and

measuring the force at the end of this lever arm. Apart from offering resistance to rotation, a second important function of the water flowing through the dynamometer is that it carries away the heat that is generated during the dissipation of energy within the dynamometer, therefore preventing the dynamometer from overheating (Atkins, 2009).

2.4.3 Electric dynamometers

Although there are still situations which justify the use of a hydraulic dynamometer, in general, the complex and accurate control required in modern day engine testing, often exceeds the capability of the hydraulic dynamometer. Consequently, most hydraulic dynamometers have been replaced by electric dynamometers, which are capable of offering far superior control (Atkins, 2009). Following is a description of some of the most common electric dynamometers used to perform engine testing.

2.4.3.1 Dry gap eddy-current dynamometers

In general, eddy-current dynamometers are very robust machines, capable of employing significant braking torque at low rotational speeds (Martyr & Plint, 2007). These dynamometers counter the torque generated by the engine under test, by employing the principle of electromagnetic induction to develop a counter torque, which is used to apply a load to the engine. The eddy-current machine consists of a high permeability steel rotor, which rotates with very fine clearances between steel loss plates. The casing of the dynamometer encapsulates coils that, when supplied with current, generates a magnetic field within the dynamometer's casing (Martyr & Plint, 2007).

During the engine testing procedure, the test engine is coupled to the dynamometer shaft which incorporates the steel rotor of the dynamometer. As the rotor of the dynamometer rotates within the dynamometer's casing, it cuts the magnetic field set up by the coils inside the casing. This causes a variation in the distribution of magnetic flux within the loss plates, which in turn leads to eddy-currents being generated within these loss plates. These circulating eddy-currents generate their own magnetic field, which opposes the original magnetic field within the dynamometer. This leads to the development of a counter torque within the dynamometer, which offers resistance to rotation of the dynamometer's rotor disk. Power is dissipated in the form of electrical resistive losses and the energy is then transferred in the form of heat to cooling water that circulates through passages in the loss plates (Martyr & Plint, 2007). The strength of the magnetic field within the dynamometer (and hence the amount of torque applied to the engine) can be controlled by altering the amount of current supplied to coils within the dynamometer casing (Killedar, 2012). With the casing of the eddy-current dynamometer also being trunnion-mounted, torque can be measured using the same principle as was described above for the hydraulic dynamometer.

2.4.3.2 Direct current (DC) dynamometers

A DC electric dynamometer is essentially a DC electric motor that operates as a generator when it is absorbing power from the engine being tested. In order to use a DC electric motor as a dynamometer, a suitable drive unit (essentially a thyristor based dc-ac-dc converter) is required to control the amount of torque applied to the test engine. DC dynamometers are typically very robust machines, which are easy to control, but have high inertia and limited maximum operating speeds (Martyr & Plint, 2007).

During the engine testing procedure, the dynamometer absorbs the shaft power generated by the test engine and converts the power into electrical energy. In large test setups, that are operated more continuously, this electrical energy can be fed back into the electrical grid, acting as a source of revenue for the dynamometer operator (Atkins, 2009). In small dynamometer setups, the amount of power generated is typically too small and does not justify the expense of installing the additional hardware required to feed the power back into the electrical grid. Therefore, in smaller test setups, the electrical energy generated is simply fed to a load bank where it is dissipated in the form of heat (Killedar, 2012). This heat is then transferred to the cooling medium (most often air) that is used to cool the load bank.

A distinct advantage that DC dynamometers have over both hydraulic and eddy-current dynamometers is that apart from being able to load the test engine, they also have the capability to both start and motor the test engine. Motoring the engine involves using the dynamometer to drive the engine at a certain operating speed while the engine's fuel supply is cut off (thus no combustion is taking place). Measuring the amount of torque applied to the engine during the motoring test, enables the operator to determine the friction losses associated with the engine when operated at the test speed.

The method that is employed to measure the torque absorbed by a DC dynamometer largely depends on the way in which the electric motor is physically integrated with the test bench. Here there are several options available depending on the existing hardware and the complexity of the test bench design. The torque measurement options associated with DC dynamometers are discussed in section 2.4.3.3, along with those of the AC dynamometer.

2.4.3.3 Alternating current (AC) dynamometers

An alternative option to the DC dynamometer is to use an AC electric motor to act as the dynamometer. These dynamometer systems consist of an AC electric motor (most often an induction motor with a squirrel-cage rotor design) and an AC variable speed drive (VSD) that is used to control the dynamometer. These drive units almost exclusively employ insulated gate bipolar transistor technology to vary the frequency of the voltage supplied to the dynamometer. This in turn controls the operating speed of the dynamometer. Similar to the DC dynamometer setup, the power absorbed from the test engine can either be fed

back into the electrical grid or it can be dissipated in an appropriately sized load bank (Martyr & Plint, 2007).

Compared to a DC dynamometer of equivalent size and power rating, an AC dynamometer with a squirrel cage rotor has much lower inertia. Due to this lower inertia, AC dynamometers are capable of faster rates of speed change, making them the preferred choice when it comes to transient testing. Furthermore, AC dynamometers are very robust and due to being based on the design of an AC electric motor, these dynamometers require very little maintenance (Killedar, 2012). Similar to DC machines, AC dynamometers also have the ability to both start and motor the test engine.

The torque measurement options for both DC and AC dynamometers are the same. Both DC and AC dynamometers can be trunnion-mounted and the torque then calculated by attaching a lever arm of known length to the dynamometer casing and measuring the force that is exerted at the end of this lever arm (as was described for the hydraulic dynamometer). However, if an electric motor is to be adapted to function as a dynamometer, quite a substantial amount of redesign to the electric motor may be required before it can be trunnion-mounted to the test bench (Martyr & Plint, 2007). In order to use the electric motor as a dynamometer, provision must also be made for the attachment of the lever- and calibration arms to the motor.

An alternative mounting arrangement is to use an inline torque transducer to measure the torque applied to the engine. These inline torque transducers are installed as part of the driveshaft connecting the dynamometer to the engine and therefore require accurate alignment of the engine and dynamometer during installation. In cases were an inline torque transducer is employed, the foot mount of the electric motor can be used to fix the motor to the test bench. The use of an inline torque transducer thus eliminates the substantial amount of design and fabrication work required to trunnion mount the electric motor. However, these transducers are far more expensive than a normal load cell, which can be used for torque measurement when a trunnion-mounted arrangement is used.

2.4.4 Coupling the dynamometer to the engine

In order to measure the power generated by the test engine, the dynamometer must be coupled to the engine using a driveshaft. There are various means of accomplishing this task, depending on the dynamic characteristics of the engine-dynamometer setup being used. The selection of the appropriate shaft and couplings used to make up the driveshaft is, however, by no means an easy undertaking. Incorrect choice of the driveshaft components or incorrect system design may give rise to a number of problems (Martyr & Plint, 2007).

One of the problems commonly associated with poor driveshaft design, is the occurrence of torsional oscillations during the engine testing procedure. These torsional oscillations are excited by the variation in engine torque, which in turn is a product of the variation in the in-cylinder pressure, between different engine

cycles. As a simple approximation, the engine-dynamometer system may be modelled as two rotating masses coupled with a flexible shaft. Such a system is inherently prone to torsional oscillations, with the two masses being capable of vibrating 180 degrees out of phase, about a node located somewhere along the shaft connecting the two masses (Martyr & Plint, 2007). If an undamped system such as this is excited by a constant torque (T_{ex}), and at a constant frequency (f), then the relationship between the amplitude of the resulting oscillation ($\emptyset$) and the frequency ratio $\left(\frac{f}{f_c}\right)$, would be as is shown in Figure 1 below (Martyr & Plint, 2007).

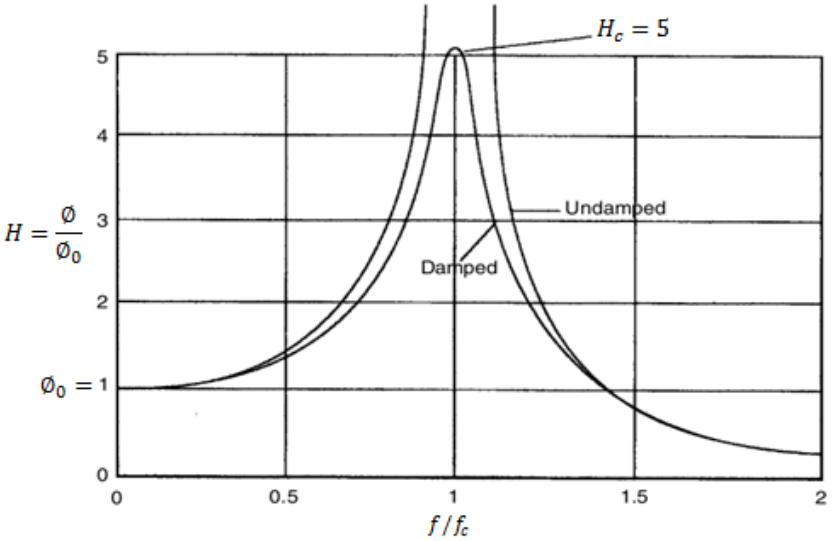

Figure 1: Relationship between amplitude and frequency ratio

(Source: Martyr & Plint, 2007)

From Figure 1 it can be seen that at low frequencies, the combined amplitude of the two masses equals the static deflection of the shaft under the influence of the exciting torque. That is $\emptyset_0 = \frac{T_{ex}}{C_s}$, where C_s is the shaft stiffness. As the excitation frequency increases, the amplitude of the oscillation also increases until $f = f_c$, where the amplitude becomes theoretically infinite and the shaft fails catastrophically. Beyond this point, the amplitude of oscillations decreases with increasing frequency (Martyr & Plint, 2007).

The figure also shows the behaviour of a damped system. Figure 1 shows that for a damped system, the value of the ratio $H = \frac{\emptyset}{\emptyset_0}$ (referred to as the dynamic amplifier) increases with an increase in frequency to reach some maximum, but finite, value at the critical frequency of the drive system (as opposed to becoming theoretically infinite as for the undamped case). Furthermore, for excitation

frequencies higher than the critical frequency of the system, the amplitude of the torsional oscillations decreases with an increase in frequency.

Consequently, the driveshaft coupling the dynamometer to the engine must be designed such that it has an appropriate stiffness (C_s) to ensure that the critical frequency of the shaft lies outside the normal operating range of the engine being tested. In addition, the shaft must also have an adequate amount of damping to allow the engine to be run through the critical speed, if it is required, without it resulting in unsatisfactory torsional oscillations that may lead to failure of the entire driveline (Martyr & Plint, 2007).

Both the main bearing on the engine side, as well as the bearing supporting the dynamometer shaft, have overhanging weight limits, that should not be exceeded. Special effort must therefore be made to design the driveshaft flanges, on the engine and dynamometer side, as well as the torsional coupling, as light as possible. In addition, care must also be taken to ensure accurate alignment of the engine and dynamometer, in order to avoid generating out of balance forces that place unnecessary stress on the engine and dynamometer shaft (Atkins, 2009).

In general, cardan shafts with a universal joint at each end of the shaft are the preferred type of shaft used in most engine testing applications. These shafts are deliberately installed with a small degree of misalignment to prevent brinelling of the needle roller bearings in the universal joints (Atkins, 2009). Furthermore, it is very important that the shaft be installed such that the yokes of the intermediate shaft lie in the same plane. This is required in order to avoid inducing any torsional oscillations (Martyr & Plint, 2007). In applications where a driveshaft other than a cardan shaft is used, it is vital that the engine and dynamometer be aligned as accurately as possible. It should, however, be kept in mind that the engine mountings will move and settle during the early stages of testing and the alignment of the test setup should therefore be checked regularly during the first few days of testing (Atkins, 2009).

2.5 Combustion in direct-injection, CI engines

The combustion process in a direct-injection (DI), compression-ignition engine starts towards the end of the compression stroke when the fuel-injection system injects fuel at high pressure into the cylinder of the engine (Heywood, 1988) (Van Basshuysen & Schäfer, 2004). The fuel enters the cylinder at high speed through either a single, or multiple orifices in the injector nozzle. The fuel atomises into small droplets and penetrates further into the combustion chamber (Heywood, 1988). The liquid fuel then vaporises, mixes with the turbulent air in the cylinder (which is at a high temperature and pressure), after which the required chemical reactions take place in order to form a mixture that is ready to auto-ignite (Baranescu & Challen, 1999). Portions of the fuel and air mixture then auto-ignites due to the temperature and pressure of the air in the cylinder being above the fuel's auto-ignition point (Heywood, 1988).

The aforementioned processes occur during the short delay period (typically lasting a few crank angle degrees) between start of injection and start of combustion (Heywood, 1988). This time lapse between the start of fuel being injected into the cylinder and the start of ignition is referred to as the *ignition delay* period. After spontaneous ignition of the air-fuel mixture occurs, initial combustion proceeds rapidly due to the build-up of prepared air-fuel mixture that was formed during the ignition delay period. This uncontrolled combustion continues until all of the already prepared air-fuel mixture has been burned. This is known as the *pre-mixed combustion* phase (Baranescu & Challen, 1999).

In the period which follows, the rate of the combustion process slows down, due to the combustion speed being limited by the rate at which additional air can be entrained into the mixture and a chemically combustible mixture can be formed. This phase of the combustion process is known as the *diffusion or mixing-controlled combustion* phase (Baranescu & Challen, 1999). Fuel injection continues throughout this combustion phase, until the required amount of fuel has been injected into the engine's cylinder. As stated by Heywood (1988), atomisation, vaporisation, mixing (of the air and fuel) and finally combustion of the fuel continues until almost all of the fuel has been burned.

The combustion phases discussed above are presented in Figure 2 below, which shows the combustion phases overlaid on a heat release diagram of a typical DI CI engine. In Figure 2, the rate of heat release is plotted against degrees of crank angle rotation, with top dead centre (TDC) occurring at 180 degrees. In addition to the premixed and mixing-controlled combustion phases discussed above, Figure 2 also indicates the start of the *late combustion* phase, which follows the mixing-controlled combustion phase. The late combustion phase indicates heat still being released during the early stages of the expansion stroke. This can be attributed to fuel energy that is still present in soot and fuel-rich combustion products (Heywood, 1988).

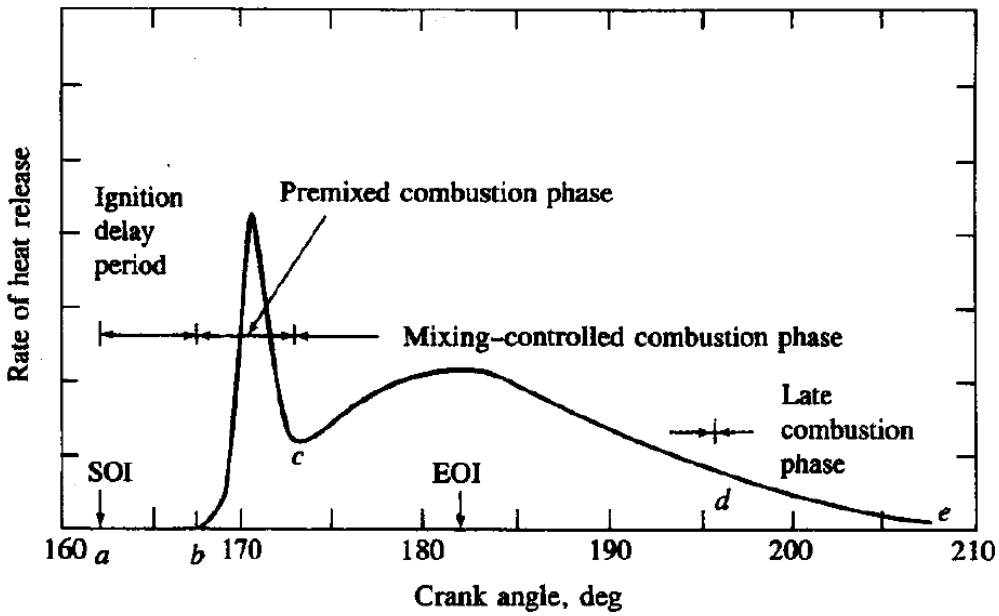

Figure 2: Combustion phases in a direct-injection, diesel engine

(Source: Heywood, 1988)

In order to obtain a short ignition delay, as well as achieve complete combustion in the short interval around TDC, rapid mixing of the fuel and air inside the combustion chamber is crucial. Improved air-fuel mixture rates are achieved by increasing the amount of air motion (swirl) inside the engine cylinder. One method of achieving the desired air motion is through careful design of the inlet ports and by forcing the air into a re-entrant combustion chamber, machined into the top of the piston (Heywood, 1988). Figure 3 shows the piston of a Yanmar L100N single-cylinder, compression-ignition engine employing such a re-entrant combustion chamber design. Another method of ensuring a short and reproducible ignition delay, is by requiring the fuel to have a certain minimum cetane number. A fuel's cetane number defines its ignition quality and is therefore an indication of the ease with which the fuel will auto-ignite, under a prescribed set of conditions (Heywood, 1988).

Figure 3: Yanmar L100N engine piston with re-entrant combustion chamber

(Source: Piston Kit for Yanmar L100 engine, [S.a.])

2.6 Engine indicating

Engine indicating refers to the measurement of a number of crank angle-based parameters which include: the pressure in the intake and exhaust manifold, in-cylinder pressure, as well as the injection line pressure, to name but a few. Ever since it was first employed, engine indicating has developed into a highly sophisticated analysis tool that is frequently employed to optimise the combustion process. The fact that this technology provides cost effective insight into the instantaneous events inside the engine, makes it especially important to engine developers (AVL, 2002).

2.6.1 Types of engine indicating

Engine indicating can be subdivided into two categories namely: high pressure indicating and low pressure indicating. High pressure indicating refers to the measurement of the pressure inside the combustion chamber of an IC engine. These measurements are most often performed using piezoelectric pressure transducers and can either be conducted over the entire engine cycle or it can also only be carried out over a limited crank angle range, depending on the application. An important application of high pressure indicating is thermodynamic analysis of the measured pressure curves. This enables calculation of the rate of heat release from the chemical energy of the fuel, which in turn allows important conclusions to be drawn concerning the combustion process (AVL, 2002). Heat release analysis is discussed further in section 2.7.4 of this document.

Low pressure indicating refers to the measurement of the crank-angle related pressures in the intake manifold and exhaust system of an IC engine. The data obtained from low pressure indicating is one of the base parameters used to

perform gas exchange analysis (AVL, 2002). However, in order to perform complete gas exchange analysis, it is important that both high and low pressure indicating are performed together (Merker *et al.* 2012).

2.6.2 The in-cylinder pressure measurement system

Although initially conducted using mechanical indicators, today an entire measurement system is employed to perform engine indicating. Such a measurement system generally consists of a pressure transducer, electronics to convert the output from the pressure transducer to a measurable signal, hardware that provides some time or angle based reference, data acquisitioning hardware and software to record the measured signals and cabling to transmit the measured signals between the various equipment.

2.6.2.1 Pressure transducer

These days, in-cylinder pressure measurement is most often performed utilizing piezoelectric transducers. Piezoelectric transducers are especially well suited to measure dynamic pressure and can only measure quasi-static pressure as opposed to purely static pressure (Engine Combustion Analysis, 2012). These transducers measure pressure by employing special piezoelectric materials. Most often, these piezoelectric materials are specially grown crystals, which output a charge proportional to the mechanical load or pressure being applied to them. These transducers have excellent dynamic behaviour, high measurement quality, high stability and good linearity. Furthermore, and perhaps most important of all, is that the metrological properties of these transducers are largely independent of temperature. This makes them especially well-suited for in-cylinder pressure measurement in IC engines (AVL, 2002). As opposed to the normal piezoelectric transducer, a water-cooled piezoelectric transducer can also be used to record the in-cylinder pressure. These transducers are extremely accurate and are used for precision measurements. However, they require constant cooling and therefore require that a separate cooling circuit be installed (Merker *et al.* 2012).

As an alternative to using a piezoelectric pressure transducer, an Optrand fibre-optic based pressure transducer can also be used to measure the in-cylinder pressure of an IC engine. The fibre-optic based sensor consists of two core fibres which are bonded to a point-source type, light-emitting diode (LED), operating on a wavelength of 850 nm (near infrared spectrum). Near infrared light from the LED travels along one of the fibres to illuminate the inner surface of a diaphragm, located in the tip of the sensor. Fibre-optic based transducers measure in-cylinder pressure due to the direct effect of the pressure causing a deflection in this diaphragm. This deflection results in a change in the intensity of the reflected light which travels back along the second optic fibre until it reaches a light detector (photodiode). Thermal effects are minimised by employing a heat shield which is installed in front of the sensor diaphragm (Wlodarczyk, 2012). Figure 4 below shows a schematic of the fibre-optic based pressure transducer discussed above.

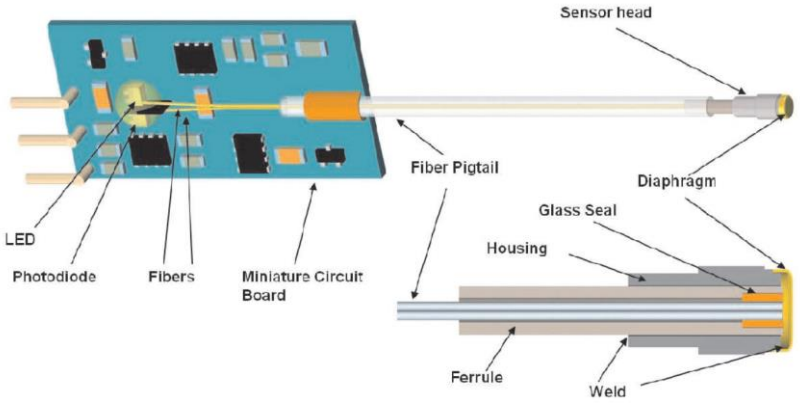

Figure 4: Optrand fibre-optic pressure transducer

(Source: Wlodarczyk, 2012)

The photodiode which measures the reflected light intensity is accompanied by circuitry employing Optrand's patented auto-referencing technique, which is used to maintain sensor accuracy at extreme temperatures (AutoPSI Pressure Sensor Operating Instructions, 2009). The auto-referencing technique corrects for both sensor drift and sensor gain (which occurs due to changes in the temperature of the sensor and signal conditioning electronics) by regulating the intensity of the light emitted by the LED (Wlodarczyk *et al.* 1998). Finally, fibre-optic based sensors are a more cost effective solution (compared to piezoelectric transducers) for measuring in-cylinder pressure.

2.6.2.2 Amplifier

When employing a piezoelectric pressure measurement system, a charge amplifier is required to convert the charge output from the piezoelectric transducer into a measurable voltage signal. This voltage signal is then transmitted, via cabling, to the indicating equipment. Piezoelectric sensors output a very low charge, therefore, in order to obtain a good signal to noise ratio, the noise present in the measurement chain must be kept as low as possible. It is for this reason that the charge amplifier, as well as the cabling connecting the sensor to the amplifier, must have very high insulation values (AVL, 2002).

In contrast, fibre-optic transducers do not require the use of an additional amplifier. The signal conditioning unit accompanying each sensor provides the voltage output directly, which makes for a much simpler and compact measurement chain, compared to when piezoelectric transducers are used.

2.6.2.3 Shaft Encoder

Irrespective of the pressure transducer used, the in-cylinder pressure measurement requires a basis to which the measured pressure values can be referenced. For this

purpose, an incremental shaft encoder must be installed on the crankshaft of the engine to provide a crank angle-based reference for the measured in-cylinder pressure (AVL, 2002). Due to the significant pressure rise associated with diesel engines, it is recommended that the encoder has a resolution of at least 0,25 degrees, to accurately define the measured in-cylinder pressure trace and to avoid aliasing of the measured signal (Zhoa & Ladammatos, 2001) (Goering, 1998). Furthermore, when selecting the encoder, it must also be verified that the encoder is able to withstand the vibration loads, generated by the test engine, at the location where the encoder is to be mounted.

2.6.2.4 Data acquisitioning system

The analogue output signal, either from the charge amplifier or the signal conditioning unit of the Optrand transducer, needs to be captured, digitized and stored by a high-speed data acquisitioning system. In order to accomplish this, the data acquisitioning system should comprise of an analogue to digital converter (to digitize the signal) and a high-speed data acquisitioning unit (to capture and temporarily store the measured data). The captured data is then used to calculate the indicating parameters, which can be displayed on the engine indicating equipment or stored on a computer (AVL, 2002).

2.6.3 Pressure transducer mounting options

Pressure transducers are either installed into existing bores in the cylinder head or directly into the combustion chamber of the engine (AVL, 2002). Using an existing bore is the preferred method of installation since it is less invasive, requires less machining and is less costly compared to other methods of performing in-cylinder pressure measurement.

2.6.3.1 Using an existing bore in the cylinder head

In diesel engines that have glow plugs the preferred method of installation is by inserting an adapter sleeve (that houses a miniature uncooled pressure transducer) into the glow plug bore. Ideally, the transducer should be installed with its diaphragm as close as possible to the combustion chamber in order to avoid creating an indicating channel. However, some glow plug bores are so small that the adapter has to be recessed in the cylinder head. In such cases, special damping chambers are incorporated in the design of the adapter to reduce the noise that results from acoustic resonations (pressure waves propagating backwards and forwards along the indicating channel). This is discussed further in section 2.6.3.2.

Apart from deciding on the position of the pressure transducer in the existing bore, it is also extremely important that the size of the adapter is correctly matched with the glow plug bore. The gap between the glow plug bore and the installed adapter should be as small as possible in order to minimize the thermal load on the transducer. Furthermore, since glow plugs aid in the cold start capability of diesel engines, replacing the glow plug with an adapter (housing a

pressure transducer) can lead to poor cold start performance. However, at normal ambient conditions, the start characteristics remain almost unaffected (AVL, 2002).

2.6.3.2 The indicating channel

When the transducer is not mounted completely flush with the cylinder head ceiling, an indicating channel is created. The addition of such an indicating channel causes an increase in the combustion chamber volume and hence a reduction in the compression ratio of the engine. This in turn can affect engine behaviour. In addition, changing pressure levels inside the combustion chamber lead to acoustic resonance which has an adverse effect on the measured pressure data (Merker *et al.* 2012).

Figure 5 shows the results obtained from a spark ignition engine where a miniature pressure transducer has been installed as part of the spark plug. The measurements were recorded at three different indicating channel lengths (Merker *et al.* 2012).

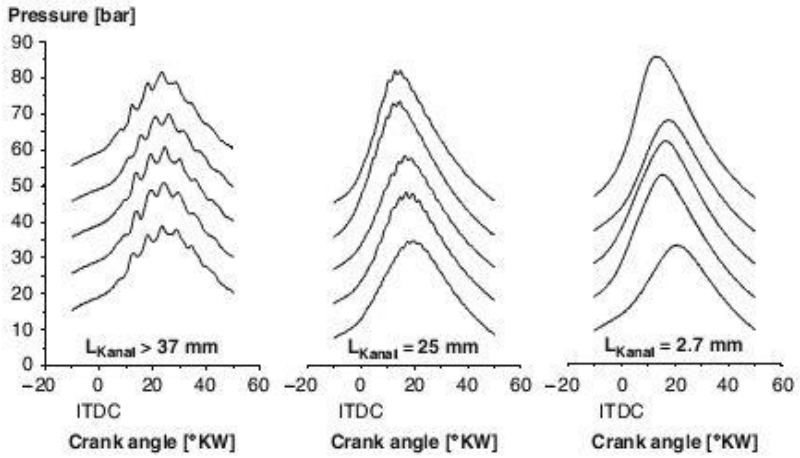

Figure 5: Effect of indicating channel length on measurement signal

(Source: Merker *et al.* 2012)

From Figure 5 it can be seen that significant amounts of vibration occur at longer indicating channel lengths. It is therefore recommended that the length of the indicating channel be kept as short as possible. Moreover, the diameter of the indicating channel should also be equal to or larger than the length of the channel (AVL, 2002). The interference frequency largely depends on the state of the gas and can therefore not be exactly determined beforehand. Owing to the uncertainty regarding the frequency of the interference, frequency filters (to filter out the noise resulting from the acoustic resonations) are also generally not applied to the measured data after it has been captured. This is mainly due to the considerable

calculative cost required for such a procedure and in order to avoid further distortion of the measured pressure signal (Merker *et al.* 2012).

2.6.3.3 Modifying the cylinder head

Distinction is made between direct installation of the transducer into the cylinder head and installations where an adapter sleeve (housing the pressure transducer) is installed in the cylinder head.

When installing the pressure transducer directly into the cylinder head, it is recommended that the transducer be installed slightly recessed from the cylinder head ceiling. A distance of 0,5 mm to 1 mm is sufficient to prevent the piston from hitting the transducer when deposits have built up on the piston surface (AVL, 2002). Although the aim is to install the transducer as flush as possible with the cylinder head ceiling, AVL (2002) has found that there are some advantages to installing the transducer at a slightly recessed position with an indicating channel that minimises oscillations. This is particularly applicable in a compression-ignition engine where the pressure transducer is subjected to high thermal loads. Special consideration must also be given to the selected measuring location of the transducer relative to the combustion chamber. The measuring location has a significant impact on the operating conditions (thermal load, flow effects, etc.) that the transducer experiences when in service (AVL, 2002).

In cases where the measurement channel needs to pass through cooling water jackets or oil galleries, an adapter sleeve is required to facilitate the installation of the pressure transducer. This is a more costly procedure compared to a direct installation since added machining and skilled workmanship is required to mount the adapter sleeve in the cylinder head of the engine. Normally the adapter sleeve will be screwed into the cylinder head using a high temperature resistant bonding agent and sealed off from the water channels and oil galleries using O-rings. As an alternative, an elastic bonding agent can be used instead of O-rings. In such cases, however, the gap between the adapter sleeve and the cylinder head should be less than 0,05 mm. After the addition of an adapter sleeve to the cylinder head, the sleeve must be checked for leaks before it can be used for measurements. This may be done by submerging the cylinder head in a water bath (AVL, 2002).

2.7 Combustion analysis

Once the measured pressure curves have been obtained, it can be used to calculate a wide variety of important parameters associated with the in-cylinder phenomena. The results obtained are referred to as indicating parameters, which can be subdivided into direct indicating parameters (obtained directly from the measured pressure curve data) and indirect indicating parameters (values that, apart from the measured pressure curve data, require additional parameters such as engine torque, crank gear geometry, etc. for calculation) (AVL, 2002).

2.7.1 Referencing and phasing of measured pressure data

By design the transducers which are used to record in-cylinder pressure, measure gauge pressure. In order to obtain the absolute pressure inside the cylinder, the measured pressure trace needs to be referenced to some point in the cycle, where an accurate estimate can be made of the absolute in-cylinder pressure (Zhoa & Ladammatos, 2001). Randolph (1990) noted that it is preferable to reference the in-cylinder pressure at a point where the cyclic variation of the measured pressure is at a minimum. This occurs when the cyclic transient thermal environment inside the combustion chamber has the least effect on the output of the pressure transducer.

There are several techniques available to determine the required shift of the measured in-cylinder pressure data, but the most commonly used method is to set the in-cylinder pressure at intake bottom dead centre (IBDC) equal to the absolute pressure in the intake manifold (also at IBDC) (Lancaster *et al.* 1975) (Zhoa & Ladammatos, 2001). At this point in the engine cycle, the piston is stationary, the cylinder's exhaust valve is closed, while the partially open intake valve experiences little flow and causes very little pressure drop. Consequently, at this instance in time the absolute pressure in the intake manifold can be considered representative of the absolute pressure in the cylinder (Lancaster *et al.* 1975). The process described above of scaling the measured pressure data from a known reference pressure point in the cycle, is referred to as "pegging" of the pressure trace. Although pegging can be performed only once for a batch of cycles captured, it is preferred that it be performed for every captured cycle. Pegging every recorded cycle eliminates the log-term drift, which is commonly associated with piezoelectric transducers (Zhoa & Ladammatos, 2001).

Apart from pegging the measured pressure data, it is also required to phase the measured pressure data relative to the in-cylinder volume. As proposed by Lancaster *et al.* (1975), this can be accomplished by mechanically setting up the incremental encoder so that its trigger coincides with the TDC mark on the flywheel of the engine. However, due to physical constraints in accessing the flywheel markings, as well as the potential inaccuracy of the degree markings on the flywheel itself, this method is more useful for the initial setup of the incremental encoder relative to the piston position. Final and more accurate phasing can then be performed by analysing the pressure data obtained during a motoring test (Zhoa & Ladammatos, 2001). This is explained further in the next section.

2.7.2 Inspecting the pressure data

Once the pressure data from the first motoring curve has been obtained and before proceeding to capture any further large amounts of data, it is advised that the data be checked to determine if it is accurate enough for further detailed analysis (Lancaster *et al.* 1975) (Zhoa & Ladammatos, 2001).

The first check to be performed is to verify that both the amplitude as well as the phasing of the peak pressure is correct. The peak pressure can be estimated using the polytropic relationship:

$$P_{max} = P_{IBDC}(r_c)^{n_p} \tag{2.1}$$

In equation (2.1), P_{max} is the maximum pressure, P_{IBDC} is the pressure in the cylinder at indicated bottom dead centre (IBDC), r_c is the compression ratio and n_p is the polytropic constant. The correct phasing of the pressure data can be verified by examining the motoring pressure curve near the position of peak pressure. Due to the leakage and heat loss, the angle at which the peak pressure occurs should precede TDC by between 0,8 to 1 degree for large direct-injection diesel engines (Zhoa & Ladammatos, 2001). If the peak pressure occurs more than 2 degrees before TDC, the data is regarded as advanced with respect to volume (V) (Lancaster *et al.* 1975). Generally, a decrease in this angle will also be observed for increased engine speed (Zhoa & Ladammatos, 2001).

As mentioned in the previous section, further and more accurate phasing can be performed using a logarithmic plot of the in-cylinder pressure versus volume (also referred to as a log P - log V plot). Zhoa & Ladammatos (2001), as well as Lancaster *et al.* (1975), points out that the compression process (from intake valve closure until the piston reaches TDC) is a polytropic process satisfying the equation:

$$PV^{n_p} = constant \tag{2.2}$$

Applying the logarithm to both sides of equation (2.2) allows the equation to be rewritten as: $\log(PV^{n_p}) = \log(constant)$. Expanding the logarithmic term leads to $\log(P) + n_p \log(V) = constant$, which can be rearranged as follows: $\log(P) = -n_p \log(V) + constant$. Thus, when plotted on a logarithmic scale, the compression segment of the pressure versus volume diagram will be a straight line, with a negative slope of n_p. Empirical data have shown the value of n_p to range between 1,25 and 1,35 for the slope of the compression line (Heywood, 1988) (Blair, 1999). Figure 6 below shows an accurately referenced and phased motoring log P - log V diagram. The diagram was obtained by Lancaster *et al.* (1975) using a single-cylinder Waukesha Cooperative Fuel Research engine.

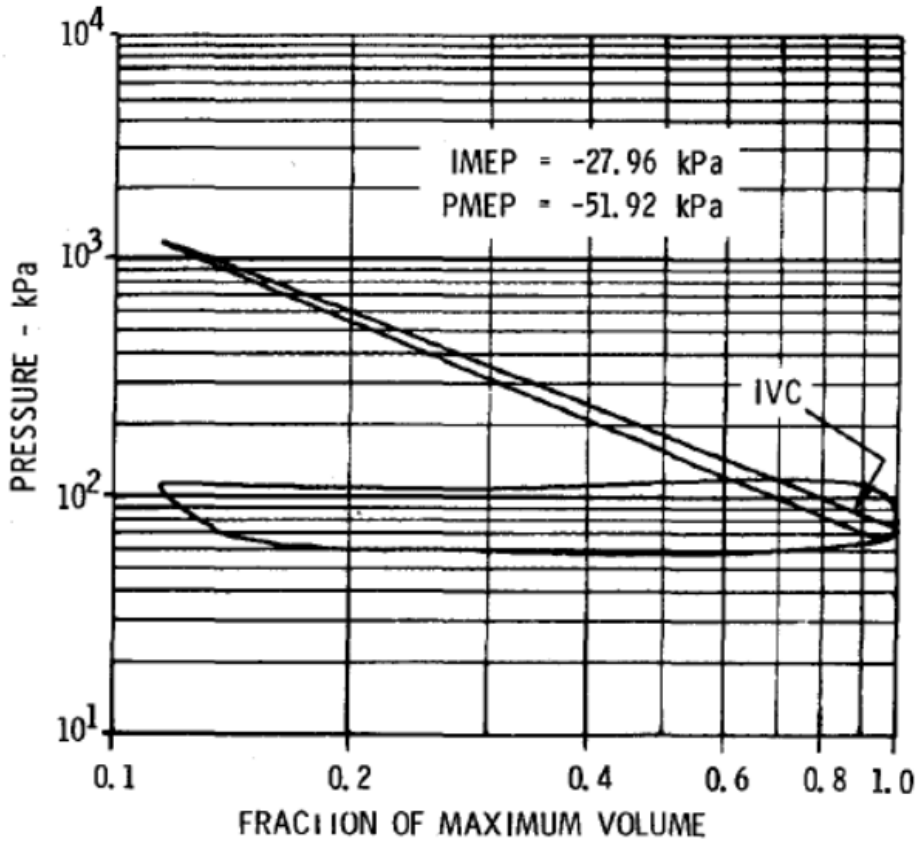

Figure 6: Accurately referenced and phased motoring log P - log V diagram

(Source: Lancaster *et al.* 1975)

There are several factors which can lead to the shape of the compression curve deviating from that of a straight line. It is these deviations that can be used to validate both the pegging and phasing of the pressure data. Assigning an incorrect reference pressure, or using an incorrect clearance volume during the data manipulation, will lead to curvature in the compression curve, at the beginning and end of the compression stroke respectively. Figure 7 displays the data of Figure 6 after the reference pressure was lowered by 20 kPa. In Figure 7 the curvature in the compression curve can be observed near the start of the compression stroke. Figure 8 shows the data from Figure 6 after the clearance volume was reduced by 14 %, which leads to a curvature in the compression curve near TDC.

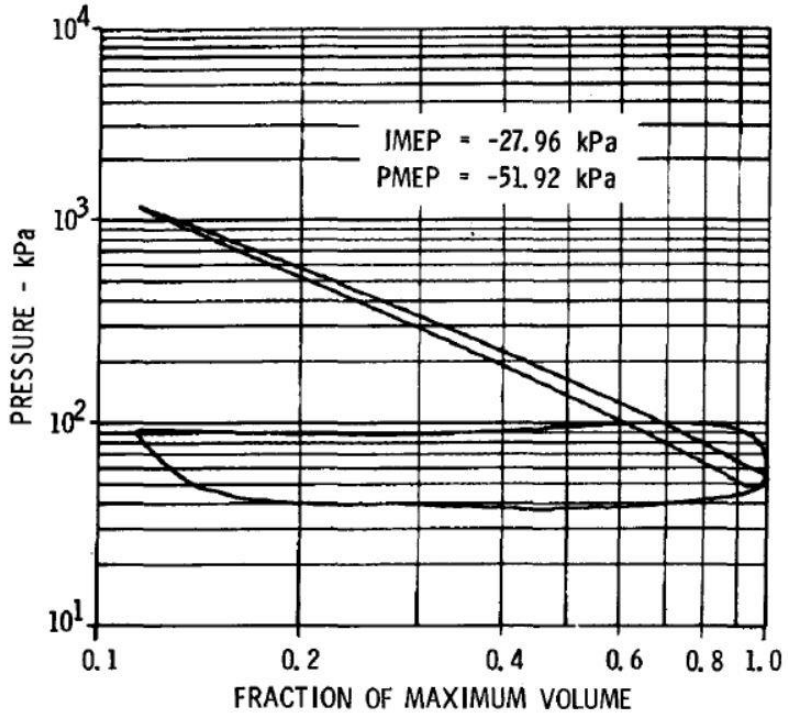

Figure 7: Data from Figure 6 with reference pressure lowered by 20 kPa

(Source: Lancaster *et al.* 1975)

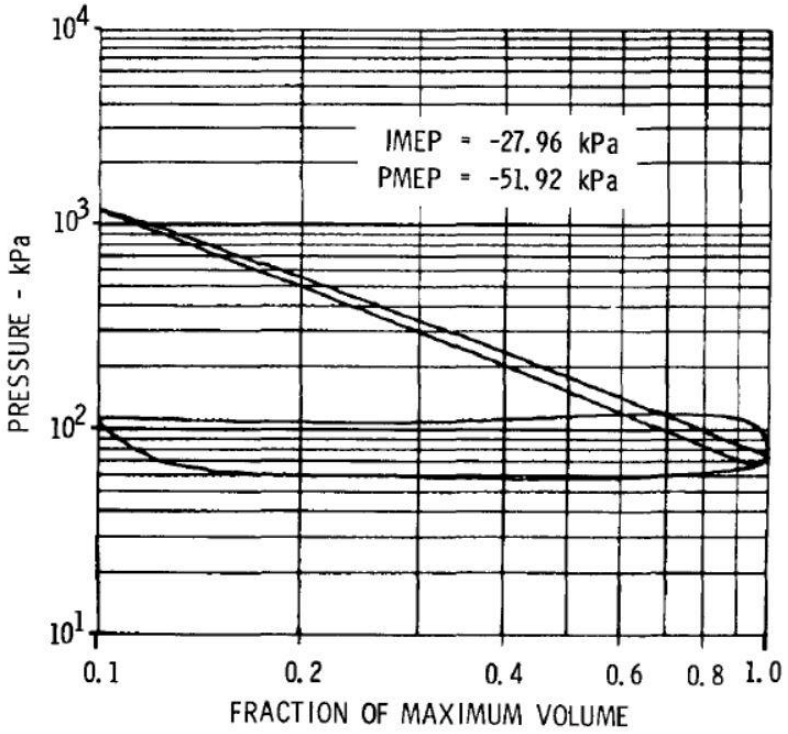

Figure 8: Data from Figure 6 with clearance volume reduced by 14 %

(Source: Lancaster *et al.* 1975)

Deviation from a straight line in the central region of the compression curve is an indication that the pressure data is incorrectly referenced with respect to crank angle position. An example of incorrectly referenced pressure data is presented in Figure 9 where the data from Figure 6 has been retarded by 2 degrees of crank angle rotation. As can be seen in Figure 9, this leads to crossover between the compression and expansion curves. Deviation from a straight line in this central region of the compression curve for properly referenced and phased data is, however, an indication that the pressure data is faulty (Lancaster et al. 1975).

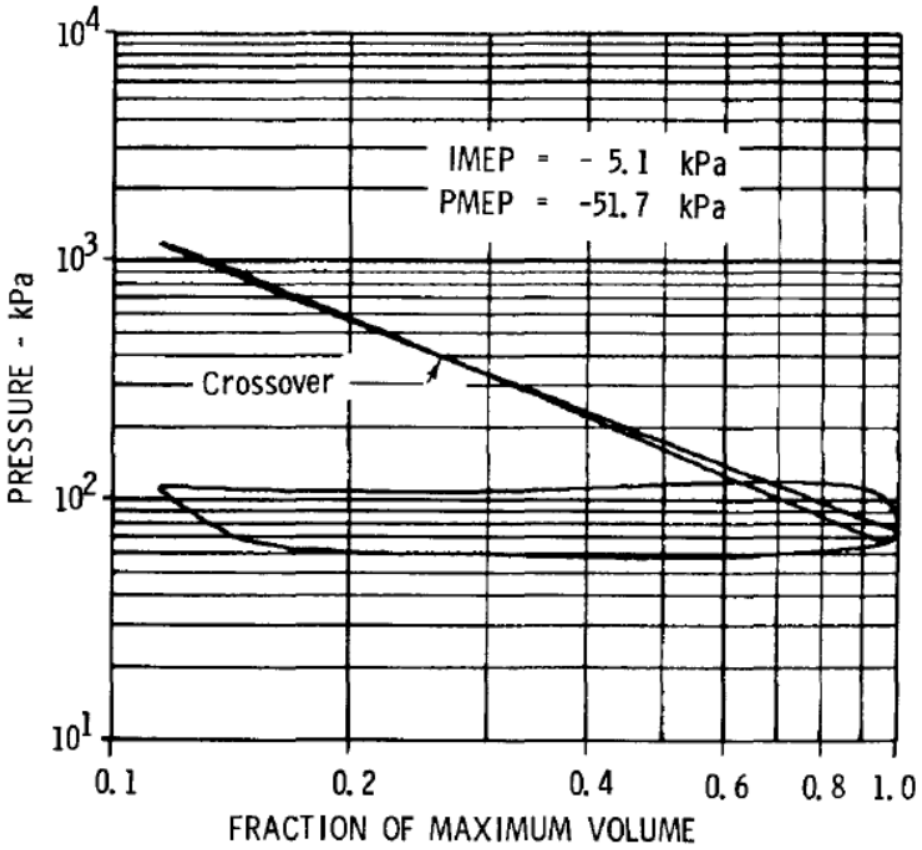

Figure 9: Data from Figure 6 retarded with 2 degrees

(Source: Lancaster *et al.* 1975)

2.7.3 Calculation of mean effective pressures

Plotting the measured in-cylinder pressure against the in-cylinder volume (P - V diagram) reveals additional information related to the combustion process. The pressure of the in-cylinder gasses acting on the surface area of the piston exerts a force on the piston, which displaces the piston in the cylinder. The gas is thus doing work on the piston, which can be described by:

$$W = \int P dV \tag{2.3}$$

In equation (2.3), W is the work done on the piston, P is the in-cylinder pressure and V is the in-cylinder volume. By performing the integration in equation (2.3) from BDC before the exhaust stroke to BDC after the intake stroke, the work exchange between the cylinder gasses and the piston (during the intake and exhaust strokes) can be calculated. This is known as the pumping work (W_p). The gross indicated work ($W_{i,gross}$) is the work performed on the piston during the compression and expansion strokes. The gross indicated work can thus be calculated by evaluating the integral in equation (2.3) from BDC before the compression stroke, to BDC after the expansion stroke (Lancaster *et al.* 1975).

Another important parameter for a four-stroke engine is the net indicated work ($W_{i,net}$), which is the difference between the gross indicated work ($W_{i,gross}$) and the pumping work (Zhoa & Ladammatos, 2001). Therefore, the net indicated work can be expressed as:

$$W_{i,net} = W_{i,gross} - W_p \tag{2.4}$$

Dividing the gross indicated work by the swept volume (V_s) of the engine, yields the gross indicated mean effective pressure ($IMEP_{gross}$) as shown in equation (2.5) below:

$$IMEP_{gross} = \frac{W_{i,gross}}{V_s} \tag{2.5}$$

The IMEP of an engine is a parameter, which is independent of engine size, engine speed and the number of cylinders in an engine (Stone, 1992). It is thus a useful parameter for comparing engines of different size (Lancaster *et al.* 1975).

Similar to equation (2.5), the work output of the engine (as measured by the dynamometer) can be quantified using a parameter referred to as the brake mean effective pressure (BMEP).

$$BMEP = \frac{4\pi T_{dyno}}{V_s} \tag{2.6}$$

with T_{dyno} being the torque measured by the dynamometer (Ferguson & Kirkpatrick, 2001).

The difference between the gross indicated mean effective pressure ($IMEP_{gross}$) and the BMEP, is known as the friction mean effective pressure (FMEP). It is a measure of the loss of power due to: mechanical friction in the engine, friction losses associated with the gas exchange process and due to driving auxiliary equipment such as the alternator, oil pump, cooling fan, etc.

$$IMEP_{gross} = BMEP + FMEP \tag{2.7}$$

The FMEP is mainly (although not exclusively) dependent on engine speed (with FMEP increasing with an increase in engine speed) (Van Basshuysen & Schäfer, 2004).

2.7.4 Heat release analysis

The type of combustion analysis most commonly associated with compression-ignition engines, is what is referred to as a heat release analysis (Stone, 1992). A heat release model is a differential model of an engine power cycle (Ferguson & Kirkpatrick, 2001). It computes the amount of heat (generally expressed as a function of crank angle) that needs to be added to an engine's cylinder contents, in order to cause the observed variations in the in-cylinder pressure (Stone, 1992). A typical heat release diagram for a direct-injection, compression-ignition engine was presented in Figure 2.

The results obtained from the heat release analysis are very helpful in discerning the various modes of combustion in a compression-ignition engine (Milton, 2005). This makes heat release analysis a powerful diagnostic tool that can be used to: validate mathematical models for engine simulation, develop new injection strategies, test new combustion system designs and evaluate how engine performance and efficiency is affected by, for example, heat transfer and changes in injection timing (Bueno *et al.* 2012) (Ferguson & Kirkpatrick, 2001).

2.7.4.1 Modelling the combustion process

In order to perform the heat release analysis, the combustion process has to be modelled using a suitable combustion model. According to Stone (1992), existing combustion models can be divided into one of three categories, namely:

1. Zero-dimensional models
2. Quasi-dimensional models
3. Multi-dimensional models

As one proceeds downward in the list above, the degree to which the model correlates with the physical combustion process increases. However, at the same time, the level of complexity involved in implementing these models (and the computational power required to solve them) also increases substantially (Engine Combustion Modelling – An Introduction, [S.a.]).

Zero-dimensional models (which are zero-dimensional in the sense that they include no consideration of the flow field dimensions) are the simplest to implement and also the most suitable to observe how the heat release rate is affected by empirical variations in engine operating parameters (Engine Combustion Modelling – An Introduction, [S.a.]). Although higher accuracy can be obtained by using either a quasi-dimensional or multi-dimensional model, the large increase in complexity involved in setting up and solving these models can often not be justified. Consequently, zero-dimensional models are frequently implemented to perform the heat release analysis of internal combustion engines and is considered adequate for diesel engine analysis (Heywood, 1988).

Zero-dimensional models can be further sub-divided into:

1. Single-zone models
2. Two-zone models

3. Multi-zone models

The most common approach to combustion modelling is to model the engine's cylinder contents as a single zone. The state of the cylinder contents is defined by average properties and no distinction is made between burned and unburned gasses. A single-zone combustion model thus considers the contents of the cylinder to be homogenous. The benefit of using such a model is having the ability to include the heat transfer and gas flow phenomena more simply (Zhoa & Ladammatos, 2001). Alternatively, the cylinder contents can also be modelled as consisting of multiple zones, each at a different thermodynamic state and having different properties. Each zone is, however, still considered to be uniform in composition and temperature, while all the zones are considered to be at the same pressure (Klein, 2007).

2.7.4.2 Zero-dimensional, single-zone model

When using a zero-dimensional, single-zone combustion model, the rate of release of the fuel's chemical energy (or heat release) can be obtained by applying the first law of thermodynamics to an open system that is considered to be quasi static (uniform in temperature and pressure). The first law, applied to such a system, yields:

$$\frac{dQ_{ch}}{d\theta} = \left(\frac{1}{\gamma-1}\right) V \frac{dP}{d\theta} + \left(\frac{\gamma}{\gamma-1}\right) P \frac{dV}{d\theta} + \frac{dQ_w}{d\theta} \tag{2.8}$$

where $\frac{dQ_{ch}}{d\theta}$ is the heat release rate, V is the cylinder volume, P is the in-cylinder pressure, θ is the crank angle, γ is the specific heat ratio and $\frac{dQ_w}{d\theta}$ is the rate of heat transfer to the cylinder wall (Heywood, 1988). For the detailed derivation of equation (2.8), please refer to Appendix A.

According to Heywood (1988), when applying equation (2.8) to model diesel combustion, the following factors complicate the analysis:

- Liquid fuel is injected into the cylinder (enters the control volume being analysed) and mixes with the air in the cylinder to produce an air-fuel distribution that is not uniform throughout the cylinder and which varies with time. The process is therefore not quasi static.
- The composition of the combustion gasses is unknown and not uniform.
- The accuracy of the correlations that are used to predict the in-cylinder heat transfer in diesel engine is not well defined.
- The crevice regions increase heat transfer and furthermore contain a non-negligible fraction of the cylinder charge. The gas trapped in these crevice regions are also at conditions different from that of the rest of the combustion chamber.

Due to the challenges posed by dealing with the above-mentioned uncertainties, simple, as well as more sophisticated methods of combustion analysis only provide approximate answers. The heat release calculated with the use of equation (2.8), is therefore referred to as the apparent heat release, as this value is

only an approximation of the actual amount of heat released during combustion, which cannot be determined exactly (Heywood, 1988).

2.7.4.3 In-cylinder heat transfer

In order to conduct the heat release analysis, the heat transfer to the cylinder wall has to be calculated using an appropriate model. The last term in equation (2.8) accounts for the rate of heat transfer from the combustion products to the cylinder wall of the combustion chamber. In general, the amount of heat transferred to the cylinder wall of the combustion chamber accounts for 25 % to 30 % of the total amount of energy released from the air-fuel mixture during the combustion process (Milton, 2005) (Finol & Robinson, 2006). The rate of heat transfer is calculated from:

$$\frac{dQ_w}{d\theta} = \frac{h\,A_w\,(T_g - T_w)}{60n} \tag{2.9}$$

where $\frac{dQ_w}{d\theta}$ is the rate of heat transfer to the cylinder wall, h is the instantaneous heat transfer coefficient, A_w is the combustion chamber wall area, T_g is the instantaneous bulk gas temperature, T_w is the mean surface temperature of the combustion chamber wall and n is the rotational speed of the engine.

As can be seen from equation (2.9), the calculation of the heat transfer rate requires knowledge of the in-cylinder heat transfer coefficient (h), which varies both with time and position (Stone, 1992). Various correlations have been developed to estimate the in-cylinder heat transfer. These correlations differ from one another based on the type of heat flux that they predict. Consequently, there are correlations to predict: the time-averaged heat flux to the cylinder walls, the instantaneous spatially-averaged heat flux to the cylinder walls, as well as correlations to predict the instantaneous local heat fluxes (Finol & Robinson, 2006). In order to perform engine modelling, the temporal variation in heat flux is required, while the spatial variation in heat flux is considered to be less important. It is only when exhaust gas emissions are considered, that the variation in heat transfer with position also needs to be accounted for (Stone, 1992). Therefore, when the rate of heat transfer to the cylinder wall of a reciprocating engine needs to be calculated, the general approach is to use an instantaneous, spatially averaged heat transfer coefficient.

One of the earliest correlations developed using an instantaneous, spatially averaged heat transfer coefficient, was the one proposed by Eichelberg (1939) - as cited by Stone (1992:378). Eichelberg (1939) proposed the following equation to model in-cylinder heat transfer:

$$\frac{Q_w}{A_s} = 2{,}43\; {v_p}^{1/3}\; (PT_g)^{1/2}\; (T_g - T_w) \tag{2.10}$$

where A_s is the instantaneous surface area of the combustion chamber, v_p is the mean piston speed and P is the instantaneous in-cylinder pressure. Equation (2.10) has the advantage of being very simple to implement, in that it only requires the user to specify a mean surface temperature. Stone (1992), however,

pointed out that the correlation proposed by Eichelberg is not dimensionally consistent, which have led to arguments where the generality of the correlation is questioned. Furthermore, the correlation proposed by Eichelberg (1939) is based on heat transfer due to free convection, which is essentially a different process from the heat transfer encountered in an internal combustion engine. Inside the cylinder of an internal combustion engine, heat transfer occurs predominantly due to forced convection, with some contribution from radiation after start of ignition (Finol & Robinson, 2006).

The first correlation, based upon forced convection, was the one proposed by Annand (1963):

$$\frac{Q_w}{A_s} = a_1 \frac{k_g}{D} Re^{b_1}\left(T_g - T_w\right) + c_1\left({T_g}^4 - {T_w}^4\right) \tag{2.11}$$

In the above equation $k_g$is the thermal conductivity of the combustion gas, D is the cylinder bore and Re is the Reynolds number. When equation (2.11) is used to predict the heat transfer in a compression-ignition engine, Watson and Janota (1982), as cited by both Stone (1992) and Finol & Robinson (2006), suggests the following values for parameters a, b and c:

$$a_1 = 0{,}25 \text{ - } 0{,}8$$
$$b_1 = 0{,}7$$
$$c_1 = 0{,}576\sigma \tag{2.12}$$
$$\sigma = \text{Stefan-Boltzmann constant}$$

When there is no radiation present, that is during the intake, compression and exhaust strokes, the value of c_1 should be set equal to zero (Stone, 1992). Another correlation that is widely used to predict in-cylinder heat transfer, is the correlation proposed by Woschni (1967):

$$h = 129.8\, D^{-0{,}2}\, P^{0{,}8}\, {T_g}^{-0{,}53}\, [C_1 v_p + C_2 \frac{V_s T_r}{P_r V_r}(P - P_m)]^{0{,}8} \tag{2.13}$$

In equation (2.13), h is the heat transfer coefficient, V_s is the swept volume of the engine and P_m is the cylinder pressure of the motored engine. P_r and T_r represent the known state of the gas corresponding to the known instantaneous volume V_r, at some reference condition. The reference condition is often taken to be at either inlet valve closure or start of injection. C_1 and C_2 are constants that should be applied having the following values:

$$C_1 = 6{,}18,\ C_2 = 0 \text{ during the scavenging period}$$
$$C_1 = 2{,}28,\ C_2 = 0 \text{ during compression} \tag{2.14}$$
$$C_1 = 2{,}28,\ C_2 = 3{,}24\times10^{-3} \text{ during combustion and expansion}$$

(Woschni,1967)

A simplified form of equation (2.13) was later proposed by Hohenberg (1979):

$$h = C_1 V^{-0,06}\, P^{0.8}\, {T_g}^{-0,4} (v_p + C_2)^{0,8} \tag{2.15}$$

where V is the instantaneous cylinder volume and constants C_1 and C_2 have values of 130 and 1,4 respectively. Hohenberg (1979), as cited by Finol & Robinson (2006), noticed that in the case of high-speed compression-ignition engines, Woschni's correlation underestimates the heat flux during the compression and exhaust phases. Furthermore, he also determined that the correlation proposed by Woschni (1967) overestimates the maximum value of the heat flux associated with combustion. These findings, along with the fact that Woschni's correlation is rather complicated to implement, led to the development of equation (2.15) (Balistrou *et al*. 2010). The surface area to be used in conjunction with equation (2.15), is calculated as:

$$A_s = 2\left(\frac{\pi(D^2)}{4}\right) + \pi(D)y \tag{2.16}$$

With y being the piston displacement from TDC as is given by equation (1.4) in Ferguson & Kirkpatrick (2001):

$$y = l + R_p - \left[\left(l^2 - {R_p}^2 \sin^2 \alpha\right)^{0,5} + R_p \cos \alpha\right] \tag{2.17}$$

In equation (2.17), l is the connecting rod length, R_p is the radius to the crank pin and α is the angle the crankshaft makes with the vertical.

3 Selecting the Dynamometer System

Before any design work could commence, an appropriate dynamometer had to be selected for the test setup. In order to evaluate the different dynamometer options available, a list of engineering requirements was compiled to quantify the desired performance specifications of the engine test setup. These requirements were then used to evaluate the various dynamometer options and finally to select the most appropriate dynamometer system.

3.1 Test setup requirements

At the time at which the dynamometer options were evaluated, a second larger test engine (a Honda GX670 V-Twin, two-cylinder, spark-ignition engine, with a maximum power output of 15,3 kW) was already selected for use in future research projects. Although the test engine for this project (Yanmar L100N, single-cylinder, compression-ignition engine) had a maximum power output of 7,4 kW, the dynamometer for this project was selected to also accommodate the larger Honda test engine. This was done in order to improve the flexibility of the test setup, with regards to future research projects. In the future, the same test setup can thus be used to conduct fuel-to-fuel evaluations on both petrol and diesel fuel blends, simply by changing the test engine. Table 1 lists the various

engineering requirements that were used to quantify the performance of the engine test setup that was to be designed.

Table 1: Test setup requirements

Specification	Unit	Yanmar L100N[a]	Honda GX670[b]
Speed range	rpm	0 - 3600	0 - 3600
Maximum speed/High idle	rpm	3800 ± 30	3850 ± 150[c]
Torque range (when absorbing power)	N·m	0 - 27,5	0 - 46
Engine speed at max torque	rpm	2200 - 2700	2500
Maximum power	kW	7,4	15,3
at engine speed	rpm	3600	3600
Speed control accuracy required	N/A	± 1% or 5 rpm (whichever is greater)[d]	
Torque control accuracy required	N·m	± 0,5	
Motoring capability	N/A	Preferred	

[a] (Source: Yanmar Industrial Engines - Operators Manual, [S.a.])

[b] (Source: Honda Owner's Manual - GX670, 2007)

[c] (Source GX670 Engine Adjustment Information, 2010)

[d] (Source: SAE J1349 Standard, 2004)

As can be seen from Table 1, the desired accuracy to which the dynamometer must be able to control the test engine, is to within ± 1 % of the speed set point and to within ± 0.5 N·m of the torque set point.

3.2 Evaluation of dynamometer systems

At this stage of the project, the viability of implementing each of the dynamometer systems researched during the literature study was evaluated. The dynamometer systems were evaluated based upon:

1. The suitability of the system, in terms of the type of testing to be performed. This was done, by considering the ability of the dynamometer system to meet the requirements listed in Table 1.
2. The complexity associated with integrating the dynamometer system with the existing test bench and test facility.
3. The initial capital layout required to procure and install the dynamometer system, as well as the cost associated with maintaining the dynamometer system.
4. The operation lifetime, as well as the flexibility of the dynamometer system, in terms of meeting future research needs.

The evaluation criteria listed above, formed the basis of the evaluation of each of the dynamometer systems. For conciseness, the details surrounding the outcome of this evaluation process, along with some additional dynamometer features, are summarised in Table 2. (The detailed evaluation, behind the data presented in Table 2, can be found in Appendix B.)

Table 2: Dynamometer comparison

	Dynamometer Type			
Features	**Hydraulic**	**Eddy-current**	**DC**	**AC**
Control Stability	Low	Good	Very Good	Excellent
Inertia	Low (Less than equivalent sized eddy-current machine)	Varies (Higher than hydraulic dynamometer)	High	Low
Drag Force	Drag force on engine	Drag force on engine	Essentially zero drag force	Essentially zero drag force
Motoring Capability	No	No	Yes	Yes
Mounting Options	Trunnion-mounted	Trunnion-mounted	Trunnion- or fixed mounted	Trunnion- or fixed mounted
Additional Hardware	Constant pressure water supply	Coolant supply	Load bank and drive unit	Load bank and drive unit
Cooling Medium	Water	Water	Air	Air
Electrical Requirements	Low	Low	High	High
Cost	Low	Moderate	High	High
Maintenance Required	Moderate	Moderate	Moderate (Brush wear needs to be monitored)	Little to no maintenance

(Adapted from: Dynamometer Comparison, [S.a])

3.3 Dynamometer system selection

Apart from the technical aspects discussed in the previous section and summarised in Table 2, a few additional factors had to be considered before the final dynamometer selection could be made. These factors originated from the

fact that the selected dynamometer had to be integrated with an existing engine test stand, the desired project outcomes and the resources available in terms of time and funding.

From a project point of view, it was decided that the selected dynamometer had to be able to motor the test engine. Even though friction tests were not planned, the ability to motor the engine is vital in order to obtain proper motoring curves during engine indicating testing. This will also extend the testing capability of the entire engine test facility, because up until this point no other test stand in the facility had the ability to motor a test engine.

Even though the hydraulic dynamometer system is the most cost effective solution, its lack of accuracy and control stability makes for an inferior system. Furthermore, it offers the least flexibility in terms of future testing and the constant drag force that it exerts on the test engine is considered substantial when it comes to testing engines with low torque output. Therefore, when it comes to the small engine test setup (requiring very accurate control) the hydraulic dynamometer is not the best option. The eddy-current dynamometer system, on the other hand, does offer improved control stability (at a higher initial cost), but it still requires an adequate coolant supply and periodic maintenance. Taking the above mentioned into consideration, along with the fact that neither of the two systems meet the requirement of being able to motor the test engine, it is clear that neither of the systems offer a viable solution.

Focus was then shifted to the use of either a DC or AC dynamometer system. Due to the selected test engine being a single-cylinder, compression-ignition engine, a large amount of torsional vibrational was expected from the engine. Furthermore, the engine also has no additional cylinders to aid in balancing the forces generated during combustion. The best possible control stability was thus required from the dynamometer's side in order to achieve the desired performance. As indicated in Table 2, both the DC and AC dynamometer offer improved control stability compared to the other dynamometer systems considered. Furthermore, both systems are air-cooled and therefore do not require additional water lines to be installed, as is the case with the hydraulic and eddy-current systems. Both the AC and the DC dynamometers have the ability to motor the test engine, allowing friction tests to be performed, however, the DC dynamometer has higher inertia compared to the AC dynamometer. Also, the AC dynamometer system requires less maintenance and is therefore a more cost effective solution in terms of maintenance cost. Quotations were also obtained for complete DC and AC dynamometer systems and it was found that the AC dynamometer system also offers the most cost effective solution in terms of initial capital layout.

Given this information, it was decided that an appropriately sized AC dynamometer system would best suit the project. Due to the small amounts of power that would be generated, it was also decided that no regeneration will be utilized and that the generated power would rather be dissipated using an air-cooled resistive load bank.

4 Test Setup Development

This section describes the design of the test bench components, as well as its integration within the existing test facility. Although some modifications were required in order to connect to the existing support services in the test cell, the focus was primarily placed on designing an appropriate engine test bench. Autodesk Inventor software was used to construct a detailed three-dimensional model of the entire assembly and to create the detailed drawings of all the designed components.

4.1 Test engine

When the test engine had to be selected for this project, the main focus was to select a small displacement engine that is simple in design, easy to maintain and that is representative of diesel engines used in modern day passenger vehicles.

The test engine selected for use in this project is a Yanmar L100N single-cylinder, 4-stroke, air-cooled, compression-ignition engine, with a displacement of 0,435 L. The engine has a mechanical fuel injection pump and a basic fuel supply system that is easy to remove, clean and replace when different fuel blends are being tested one after the other. The Yanmar engine also has no on-board electronic control unit capable of changing the setup of the engine between tests and therefore influence the test results. Its parts are readily available and it is a popular research engine that is referenced in many biodiesel research papers. There is also already test data available from previous research that can be used both for comparison and to validate the results obtained with the test setup being developed in this project.

Most importantly, the re-entrant combustion chamber design that is employed by the Yanmar test engine is very common in larger diesel engines utilised by modern passenger vehicles. The test engine's familiar combustion chamber design, coupled with a compression ratio of 19,7:1 (Yanmar Industrial Engines - Operators Manual, [S.a.]), gives it combustion characteristics which are very similar to that of larger diesel engines. The results obtained with the smaller Yanmar engine can thus be considered representative of the results that will be obtained with the use of a larger, four-cylinder diesel engine.

The Yanmar engine was previously used in a final year mechanical project and was thus already available in the test facility. Apart from being run-in during the previous project, the engine was only subjected to an additional three hours of testing. It could therefore safely be concluded that the engine did not experienced significant wear and tear during its operational lifetime and was more than suitable for use in this project. The detailed specifications of the Yanmar L100N engine are listed in Table 16 in Appendix I.

4.2 Test bed and engine stand design

The bed of the test bench, as well as the engine stand used to support the Yanmar engine, was already designed and manufactured as part of Mr E. Grobbelaar's final year project for his Bachelor's degree in Mechanical Engineering (Grobbelaar, 2011). Apart from the addition of a few threaded holes, used to secure the throttle actuator to the test bed, the existing test bed of the test bench was used unaltered in this project.

The engine stand, however, required a few modifications to facilitate the mounting of the fuel supply system and other instrumentation. Suitable anti-vibration engine mountings were already designed by Grobbelaar (2011) during his final year project and formed part of the existing engine stand design. Therefore, it was not required to consider the design of the engine mountings for the test engine.

4.3 Electric dynamometer

In an effort to reduce the overall cost of the system, it was decided to measure the torque generated using a load cell, as opposed to using an in-line torque transducer. From a practical point of view, especially when it comes to steady state testing, using a load cell is also preferred. This is substantiated by Martyr & Plint (2007) who states that compared to an in-line torque transducer, a well-maintained, trunnion-mounted machine more consistently provides accurate torque measurement results during steady state testing.

4.3.1 Selecting the electric motor

Before any design work could commence, an appropriate AC electric motor had to be selected that could be used as the dynamometer. In order to ensure that the electric motor was suitable for the application, both the electrical and mechanical characteristics of the motor had to be considered.

4.3.1.1 Electrical characteristics

In order to specify the power rating and rated speed of the required motor, the performance curve of the electric motor was compared to the performance curves of both the Yanmar L100N compression-ignition engine and the larger Honda GX670 spark-ignition engine.

The synchronous speed (n_{sync}), of an induction motor is defined by equation (7.1) in S.J. Chapman (2005) as:

$$n_{sync} = \frac{120 f_e}{N_p} \tag{4.1}$$

where, f_e is the frequency of the input voltage and N_p is the number of poles in the machine. From equation (4.1) it is clear that the lower the number of poles in the machine, the higher the synchronous speed of the motor. In an effort to match

the electric motor as closely as possible to the internal combustion engine, a two pole AC induction motor was selected.

The two pole construction gives the motor a synchronous speed of:

$$n_{sync} = \frac{120(50)}{2} \tag{4.2}$$

$$= 3000\ rpm \tag{4.3}$$

The standard power ratings of available induction motors were evaluated based on the Honda engine's maximum power output of 15,3 kW. Both a 15 kW and an 18,5 kW AC induction motor were identified as possible dynamometer options. The performance curves of both these electric motors were then compared to the performance curves of the test engines. The performance curves of both test engines were plotted using data provided by the original engine manufacturer. The performance curves plotted for the electric motors represent the expected performance of a motor and drive unit combination, where the motor is no longer limited to operating at only 50 Hz.

Essentially, when employing a motor and drive unit combination, there is constant torque region for all speeds below the synchronous speed (or when taking into account slip, the rated speed) of the motor. At speeds higher than the synchronous speed, the motor and drive unit has a constant power rating and the torque therefore drops off as the operating speed of the motor increases (Induction Motor Speed Torque Characteristics, 2006). Figure 10 below shows the torque (plotted on the vertical axis) versus speed (plotted on the horizontal axis) of both the electric motors and the test engines. The vertical dotted line indicates the synchronous speed of the electric motors.

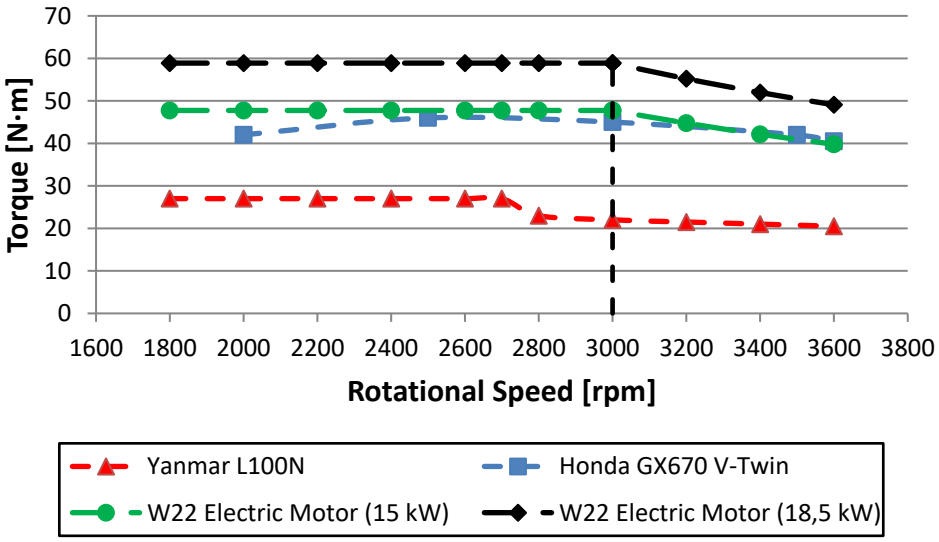

Figure 10: Test engine and electric motor torque curves

From Figure 10 it can be seen that although the 15 kW electric motor, is capable of absorbing the torque generated by the Yanmar diesel engine, it has too low a rating to be used with the larger Honda petrol engine when testing at speeds above the electric motor's rated speed. It is advised that a motor with a power rating higher than the maximum power developed by the engine is selected. This will ensure that situations are avoided where the motor becomes overloaded for short periods of time when the torque output of the engine spikes to values larger than the maximum rated output of the engine. These torsional oscillations are quite common, especially when testing single-cylinder, compression-ignition engines.

Considering all of the above, an induction motor with power rating of 18,5 kW was selected to be used as the dynamometer. This makes for a more suitable dynamometer system, with additional capacity, which prevents the dynamometer from being required to continuously operate close to its rated load.

4.3.1.2 Mechanical characteristics

Due to a load cell being used for torque measurement, the electric motor had to be trunnion-mounted between two pedestals. Therefore, in addition to satisfying the electrical requirements listed above, the physical construction of the selected motor had to meet the following criteria:

- The motor's casing had to allow for attachment of calibrating arms as well as a load cell.
- The shaft of the motor had to be such that an encoder could be mounted to it in order to measure the operating speed of the electric motor.
- The physical construction of the motor had to allow it to be trunnion- mounted between pedestal bearings.
- The terminal box of the motor had to be mounted on top of the electric motor in order to minimise the influence of the electric cabling on the torque measurements.
- The electric motor had to be air-cooled, as water lines running to and from the motor's casing will influence the torque measurements.

After identifying a selection of motors that satisfied the electrical requirements, quotations were obtained from various suppliers. These quotations were then evaluated along with the available mounting options of each electric motor considered.

4.3.1.3 Selected motor

After considering both the electrical and mechanical characteristics discussed above, a W22 electric motor from WEG was selected for the application. The selected motor is a standard efficiency, 3-phase, 2-pole, AC, induction motor, with a power rating of 18,5 kW.

The selected motor employs a cast iron frame and has both a foot and flange mount. Both mounting options were requested on the single motor in order to

allow as much freedom as possible for the design of the trunnion bearings, load cell attachment and calibration arm mountings.

4.3.2 Modifications made to electric motor

A number of modifications were made both to the shaft and casing of the purchased electric motor, in order to allow it to be trunnion-mounted to the dynamometer stand.

4.3.2.1 Motor casing

The standard driveshaft of the electric motor was too short (especially on the non-drive end of the motor) to be able to suspend the motor from its shaft when trunnion mounting it. As a result, the design of the motor's casing had to be adapted in order to trunnion mount the entire casing between two pedestal bearings, rendering the motor's casing free to rotate. After disassembly of the electric motor, existing components were altered and a number of additional components were designed, in order to convert the electric motor into a trunnion-mounted dynamometer.

Two new flanges were designed that could attach to the existing flanges on both ends of the electric motor (access to the flange on the non-drive end of the motor was obtained by removing the cooling fan and shroud from this end of the motor). The new flange on the non-drive end of the dynamometer was designed purely to act as interface between the dynamometer and the rear trunnion bearing (housed in the rear pedestal). In addition to functioning as an interface between the pedestal bearing and the dynamometer, the flange designed for the drive end of the dynamometer also acts as attachment point for the load cell and dynamometer calibration arms. Finally, both existing flanges of the electric motor were also modified to allow attachment and ensure proper alignment of the two newly designed flanges. In Figure 11 below, the designed flanges for the drive end and non-drive end of the dynamometer can be seen. The designed flange for the non-drive end is shown bolted to the existing flange of the electric motor. The newly designed flanges can also be seen in Figure 13, which shows the flanges after they have been integrated as part of the complete dynamometer assembly.

Figure 11: Drive end flange (top) & non-drive end flange (bottom)

4.3.2.2 Dynamometer shaft

The shaft with which the electric motor was supplied also required quite a few modifications. Firstly, the electric motor's driveshaft and rotor assembly were removed in order to machine down the driveshaft ends to accurately interface with the pedestal bearings. Secondly, the drive end of shaft was modified for proper fitment of the taper lock (used to connect the dynamometer's shaft to the test setup's driveshaft). Furthermore, the shaft was also extended to enable attachment of a shaft encoder at the rear of the dynamometer. This encoder was used to measure the dynamometer's rotational speed.

The dynamometer's shaft was extended by first drilling and tapping the non-drive end of the shaft. A threaded shaft extension was then designed and fabricated using an oversized diameter compared to that of the dynamometer shaft. After applying Loctite 577 thread locking compound to the thread of the designed shaft extension, the extension piece was bolted to the dynamometer shaft and torqued. This method of attaching the extension piece to the dynamometer shaft was considered sufficient seeing that the shaft extension would not support any load and that it would only be used to rotate the shaft encoder (which has a very low starting torque of only 0,05 N·m and moment of inertia of 6×10^{-6} kg·m^2).

After allowing a minimum of 24 hours for the Loctite to cure, the shaft assembly was put back into the lathe for machining. Due to the shaft encoder's small tolerance for radial run-out, it was vital that the extension piece added was concentric with the rest of the dynamometer's shaft. Concentricity of the final shaft design was achieved by machining the assembled shaft and extension piece down to size as a single component. During the machining process, the shaft was supported at its bearing surfaces while the radial run-out of the shaft extension was monitored using a mechanical dial gauge. The shaft was machined down to its final size (as dictated by the inner diameter of the selected trunnion bearing), while ensuring that the radial run-out of the extended shaft remained within acceptable levels according to the shaft encoder's specifications.

4.3.2.3 Trunnion bearings

Mechanical mounts were required to physically mount the dynamometer to the test bench, as well as allow the torque reaction of the dynamometer to be measured. This was addressed by designing two pedestals that were strong enough to support the entire mass of the dynamometer, as well as resist the dynamic loads that are generated when the dynamometer is absorbing power from the engine. These pedestals were designed to house trunnion bearings, which enable the dynamometer's casing to pivot around the central axis formed by the dynamometer's shaft. The outer races of these trunnion bearings were located in the pedestals using a slight press fit, while the inner races of the bearings seated on the designed flanges (shown in Figure 11) which were attached to the dynamometer's casing. The torque reaction was measured using a load cell that was attached to the dynamometer's casing.

The above-mentioned pedestals were manufactured by cutting the designed profiles out of a 40 mm thick billet of steel. Preliminary machining of the pedestals was then performed in order to reduce the thickness of the profiles where required. The pedestal bases were laser cut from 25 mm thick mild steel, after which welded constructions were formed with the profiles machined previously. Up until this point, the pedestals were manufactured still slightly larger than their specified final dimensions. This was done deliberately as it was anticipated that localised heating introduced by the welding process, as well as stress relieving of the material (due to the large amount of material being removed during the preliminary machining phase) would cause the material to distort. After the welding was completed, the pedestals were machined to meet the final specified tolerances. Finally, the fabrication was completed by line boring the two pedestals to ensure that the bearing surfaces were concentric. A bearing plate was also designed and fabricated for each pedestal in order to keep the bearings in position and close off the pedestal. The rear bearing pate also doubles as mounting bracket for the shaft encoder measuring the rotational speed of the dynamometer. In Figure 12 below the fabricated pedestals can be seen along with their bearing plates, the designed flanges for the front and rear of the dynamometer, as well as the modified existing flanges of the electric motor.

Figure 12: Machined dynamometer components prior to being painted

The front pedestal was machined to accept a SKF double row, self-aligning, ball bearing (part no: 1213 ETN9). The self-aligning bearing was selected, because it is insensitive to angular misalignment between the dynamometer casing and the axis formed by the two bearing housings (pedestals). The self-aligning bearing also generates less friction compared to other types of roller bearings, rendering it ideal for the application (friction in the trunnion bearings needs to be kept to a minimum in order to obtain repeatable and accurate torque measurements) (Self-aligning ball bearings, [S.a.]).

For the rear pedestal, a SKF, single row, deep groove ball bearing with metal shields was selected (part no: 6213-2Z). The deep groove ball bearing is capable of accommodating axial load and is therefore employed to ensure axial location of the dynamometer casing. Its sealed construction also renders it maintenance free without influencing the friction characteristics of the bearing, due to the shields not making contact with the inner bearing ring.

4.3.2.4 Additional dynamometer components

Apart from the various components already mentioned in this section, a number of additional dynamometer components were also designed to enable calibration of the dynamometer and mounting of the load cell.

Calibration arms

Using the maximum rated torque output of both the Yanmar and the larger Honda test engine, the sensitivity and mounting position of the load cell, as well as the spatial constraints surrounding the location of the test setup, a practical length was chosen for the design of the calibration and counterweight arm. Other design requirements considered during the design of the arms included high rigidity and minimising the effects of thermal expansion (which leads to a change in length of the arms due to varying material temperature between consecutive calibration

events). The above mentioned were addressed by choosing a tall and slender profile for the design of the arms, while limiting the length of the arms to a dimension that is practical.

Weight tray

A weight tray was also designed so that existing calibration masses could be used to calibrate the dynamometer. The tray mounts directly to the dynamometer's designed calibration arm and employs a knife-edge design which fits into a v-groove machined into the calibration arm. This knife-edge ensures that the calibration masses are always mounted at a preselected distance from the rotation axis of the dynamometer.

Load cell brackets

The torque reaction of the dynamometer was measured using a HBM U2A tension and compression load cell. Due to the physical construction of the load cell, a special bracket and connecting rod arrangement had to be designed to mount the load cell to both the dynamometer stand and the dynamometer. The load cell, along with the designed calibration arms and weight tray are shown in Figure 13 below.

Figure 13: Load cell (left), calibration arms and weight tray (right)

4.3.3 Dynamometer stand design

The existing stand, used to support the previously employed Froude dynamometer, had to be modified to accept the newly designed electric

dynamometer. This was achieved by extending the length of the test bench, as well as by changing the mounting location of the load cell. The length of the dynamometer was increased by adding an extension piece and an extra set of support legs to the front of the existing stand. New holes were then drilled to mount the newly designed load cell bracket, as well as the front and rear pedestals to the dynamometer stand.

4.4 Driveshaft and safety guard design

At the start of this project a driveshaft (which was designed by Grobbelaar (2011) during his final year project) was already available. This driveshaft was previously used to connect the Yanmar engine to a hydraulic dynamometer. Due to employing the same test engine as the previous test setup, it was decided to rather adapt and reuse the existing driveshaft, as appose to designing a completely new shaft. This was done in an effort to save cost and to expedite the project.

For the design of the previous driveshaft, an automobile front axle half shaft assembly was used as a departure point. An adapter flange was designed to connect the inner constant velocity joint of the half shaft, to the imperial sized output shaft of the Yanmar test engine. This was accomplished by purchasing a Fenner weld-on hub (designed to accept an imperial sized taper-lock) and welding this hub to the designed flange. Final machining of the flange was performed after the welding process to ensure that the final tolerances were met and that the flange ran true. This section of the previous driveshaft was used unaltered for the new test setup.

The other end of the driveshaft was connected to the dynamometer by implementing a completely new design. Due to the anticipated oscillation in the torque output of the engine, a Fenaflex F50 tyre coupling was selected to damp out the majority of this torsional vibrations. The flexible coupling was connected to the driveshaft through the use of a taper lock and a parallel key (an end-milled parallel keyway was machined into the driveshaft specifically for this purpose). The flexible coupling was designed by catalogue and selected based on its power rating at the rated speed of the engine. In addition, the factors of safety guarding against failure due to the maximum nominal torque output of the engine, as well as due to the peak torque output of the engine (which occurs due to spikes in the engine's torque output profile) were calculated. The peak torque output of the engine was obtained by applying a service factor (determined based upon the system architecture and available literature) to the maximum rated torque output of the engine. Analysis showed the flexible coupling has a factor of safety of 2,4 guarding against failure given the maximum nominal torque output of the engine and a factor of safety of 1,3 guarding against short term overload of the flexible coupling during torque spikes. The detailed procedure regarding the sizing and selection of the flexible coupling is presented in Appendix C.

A second flange was designed to connect the flexible coupling to the dynamometer shaft. Here attachment was again ensured by incorporating a weld-

on hub into the design of the flange to allow the flange to be fixed to the dynamometer shaft through the use of a taper lock. This same flange also makes provision for the mounting of a spherical bearing (SKF part no: GE 20 ES 2RS), which locates the end of the driveshaft that is extending through the centre of the flexible coupling. This spherical bearing, along with the 4 degrees of misalignment that can be tolerated by the flexible coupling, allows for relative misalignment between the output shaft of the engine and the dynamometer's shaft. Due to the construction of the driveshaft, a small degree of misalignment is actually preferred as it prevents brinelling of the constant velocity joint that is connected to the output shaft of the test engine.

Due to the addition of a keyway to the shaft, a detailed fatigue analysis was performed on the design of the driveshaft. This was done using the distortion energy ASME elliptic failure criteria which indicated a factor of safety of 1,6 guarding against cyclic loading of the driveshaft. A check was also performed for first cycle yielding by calculating the maximum von Mises stress and comparing it to the yield strength of the driveshaft material. This produced a factor of safety of 2,65. The details of the aforementioned driveshaft analysis can be found in Appendix D. Finally, as an additional check, the structural integrity of the driveshaft design was also verified by performing a finite element analysis (FEA) on the driveshaft design. The results obtained from the linear static analysis showed good correlation with hand calculations performed for the same applied loads. The FEA results indicated a factor of safety of 1,7 guarding against yielding for a pure torsional load case. The details surrounding the finite element model used, as well as the results obtained are presented in Appendix E.

Once it was verified that the driveshaft design was satisfactory, the required modifications were made to the length of the existing driveshaft safety guard. This guard is installed to protect personnel and equipment in the event of a catastrophic failure of any of the driveshaft components. The guard encloses the entire driveshaft and will, during failure of any driveshaft component, constrain such a component, preventing it from inflicting any further damage to equipment or test cell personnel. The newly designed driveshaft and modified safety guard is shown in Figure 14 below.

Figure 14: Driveshaft and safety guard

4.5 Test setup integration

Once manufacturing of the designed components were complete, fit checks were performed to verify that the required tolerances were met during the fabrication process. Upon completion of the fit checks, the parts were cleaned and painted.

4.5.1 Test bench integration

Integration of the entire test setup was started by first adding the mounting holes for the throttle actuator to the test bed, after which the test bed was installed in the allocated test cell. The test bed was then aligned and levelled using the six anti-vibration feet located underneath the bed. After satisfactory alignment was achieved, the engine and dynamometer was installed, along with their respective support stands. The dynamometer was then mechanically aligned with the engine, after which it was secured to its support stand by bolting down the pedestals and connecting the load cell to the dynamometer's casing. At this point in time the driveshaft was not yet installed as the electric motor and its drive unit still had to be commissioned (this requires running the electric motor without any load).

Finally, the exhaust system of the engine was installed and connected to the test cell's extraction system. This required that additional flanges and exhaust extension pieces be designed and fabricated in order to tie the standard exhaust system of the engine into the exhaust extraction system of the test cell. Care was taken when implementing the aforementioned changes to prevent creating additional back pressure at the outlet of the engine's standard exhaust system.

4.5.2 Integration of dynamometer system

For the purpose of commissioning the dynamometer system, the shaft encoder at the back of the dynamometer was installed to enable the rotational speed of the dynamometer to be measured. After all of the required mechanical integration was completed, the supplier of the drive unit was contacted to install both the drive unit and the 18,5 kW brake resistor. A formal proposal document was provided to the supplier of the drive and brake resistor, ahead of time, in which all of the test setup requirements were detailed (Grobbelaar & Haines, 2012). No fuel system was installed at this stage and the engine was still operated using its supplied fuel tank. The supplier then performed an on-site installation of the hardware and commissioned the dynamometer system. During the commissioning process, the driveshaft and safety guard was installed to enable the dynamometer to apply load to the engine. This was done to verify the functionality of the complete system.

4.6 Fuel supply system

Accurate measurement of the test engine's fuel consumption is essential in order to obtain accurate and repeatable engine performance data. This required the design and installation of a fuel supply system comprising of:

- A supply tank
- An AVL 730 dynamic fuel balance (fuel flow meter)
- Electric fuel pumps
- Fuel filters
- Suitable piping, fuel lines and ball valves to direct the flow of fuel
- Temperature sensors to monitor the fuel supply and return temperature

4.6.1 Fuel system layout

Installation of the fuel supply system was started by designing and manufacturing a support bracket for the AVL 730 dynamic fuel balance, which was then used to mount the fuel flow meter to the test cell wall. This bracket supports the flow meter using three adjustable feet, which are used to ensure that the flow meter is levelled correctly. The required fittings were then installed and the inlet and outlet ports of the flow meter were setup to connect to the fuel supply tank and the engine. Due to the small capacity of the engine, as well as the fact that different fuel blends will be tested, a header tank was not installed. Instead, fuel is supplied to the fuel flow meter from a 25 L container, which can easily be exchanged for a container with a different fuel blend without having to disturb the installed fuel supply system of the engine.

A 6,5 bar electric fuel pump is used to pump fuel from the 25 L container, through a 10 micron diesel filter, to the inlet of the fuel flow meter. From the fuel flow meter, the fuel is then gravity fed through a ball valve, after which the fuel flows through a fixed ¼ inch stainless steel line to the test bed. From here, a second

electric fuel pump (3 bar capacity) is used to pump the fuel through a 3 micron diesel filter and directly to the engine's injector. The return fuel line is routed from the engine's injector and ties back into the supply fuel line on the suction side of the 3 bar pump. This then completes the closed fuel circuit, which fuel can only enter by first passing thought the fuel flow meter. Therefore, once all the fuel lines have been primed, any fuel being consumed by the engine will pass through the flow meter first and be measured. The closed fuel circuit existing between the engine and fuel flow meter, allows the fuel supply container (which is located before the fuel flow meter in the circuit) to be exchanged and the engine started without needing to bleed the fuel system each time.

4.6.2 Fuel system wiring

The inlet of the fuel flow meter is controlled by a solenoid valve, which only opens when the fuel flow meter needs to refill its measuring vessel. Therefore, a wiring circuit was setup where the 6,5 bar fuel pump receives its supply from the 12 V battery next to the test bed. A relay (with normally open terminals and whose coil is energized by the same circuit which energizes the solenoid valve of the fuel flow meter) was then inserted in series with this circuit. Consequently, every time that the fuel flow meter opens and closes the solenoid valve, it automatically also switches the fuel pump (supplying the fuel to the fuel flow meter) on or off. The second fuel pump (located on the test bed) is controlled from the ignition switch of the engine, as it only needs to pump fuel to the engine when the engine's ignition is switched on.

5 Instrumentation and Actuators

After preliminary setup of the dynamometer system was completed, the rest of the test setup was instrumented. Various sensors were fitted to monitor the operating condition of the engine, as well as to measure and record engine performance and engine indicating parameters. Detailed wiring diagrams were also created to document the installation of all instrumentation and actuators.

5.1 Throttle actuator

A TGS Posicon 1000 throttle actuator was installed in order to control the fuel supply to the test engine. The TGS 1003 Mechanical Positioning Device, employed by the system, has a nominal stroke of 100 mm and a nominal force output of 140 N. The system's control unit accepts a 0 - 10 V analogue signal as input (to control the position of the actuator) and outputs a 0 - 10 V signal (to indicate the actual position of the actuator).

Considering the high levels of vibration generated by the test engine, the sensitive nature of the throttle actuator, as well as its relatively high mass, it was decided not to connect the throttle actuator directly to the throttle linkage of the engine. Instead, the throttle actuator was mounted to the test bed, directly beneath the

engine test stand. A throttle cable was then installed to connect the throttle actuator to the original throttle linkage of the engine. This then isolated the throttle actuator from any engine vibration and rendered the throttle and governor settings of the engine untouched. The installed throttle actuator can be seen in Figure 15 below.

Figure 15: Instrumented test setup

5.2 Load cell and signal amplifier

The load cell employed was a 4-wire circuit, 500 kgf HBM U2A tension and compression load cell. The load cell is capable of measuring the applied load in both tension and compression (this enables torque to be measured both when absorbing and motoring the engine). However, should the need exist to also measure the torque when motoring the engine, the load cell also needs to be calibrated in compression.

The load cell was mounted to the dynamometer stand, where it was mechanically attached to the dynamometer. Shielded extension wire was then used to connect

the load cell to a LCS/I/0350 signal amplifier located within the control room. Special care was taken to avoid routing the cabling close to any AC wiring or other noise sources that could negatively influence the torque readings.

5.3 Fuel flow measurement

As mentioned previously, fuel flow to the engine was measured using an AVL 730 dynamic fuel balance (fuel flow meter). The fuel flow meter employs a gravimetric measurement principle (which eliminates the need to account for the variation in fuel temperature and hence changes in fuel density) to monitor the weight of fuel in a measuring vessel. The measuring vessel is supported by a combination of a torsion spring and beam balance, while the vertical displacement of the vessel (due to a change in fuel mass) is monitored using a highly sensitive capacitive sensor. The unit is capable of measuring the instantaneous fuel consumption, as well as the cumulative fuel consumption over a specified period of time. These measurements can also be recorded during dynamic changes in the engine's operating condition. A fuel temperature control unit was not required in the end as the data showed that the inlet fuel temperature remained within ±2 °C throughout the tests. The installed AVL fuel flow meter is shown in Figure 16 below.

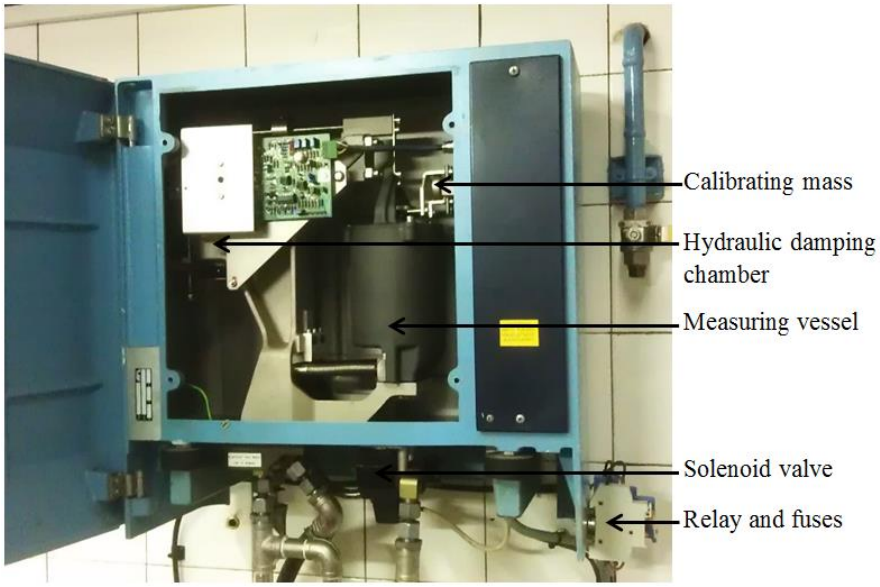

Figure 16: Installed AVL fuel flow meter

5.4 Engine oil pressure

A WIKA A-10 pressure transducer was installed to measure the test engine's oil pressure during operation. An oil pressure sensor with a rating of 0 - 25 bar was

selected and installed. The sensor uses a 2-wire circuit and has a 4 - 20 mA output.

Access to the engine's oil pressure was obtained by removing an existing plug from one of the oil channels running through the engine's crank case. A special fitting was fabricated that was installed into the oil channel and the oil pressure sensor was mounted to the engine stand. A braded stainless steel hose was then used to connect the pressure sensor to the fitting installed in the engine's oil channel.

5.5 Engine indicating instrumentation

In order to perform engine indicating the test engine was instrumented with transducers to record the in-cylinder and intake manifold pressures. A shaft encoder was also installed in order to reference the measured pressures to the instantaneous position of the crankshaft.

5.5.1 In-cylinder pressure transducer selection

After considering various Kistler and AVL pressure sensors, it was decided that the significant cost associated with using a traditional piezoelectric measurement chain could not be justified. Alternative measurement options were researched during which Optrand transducers were identified as a viable solution.

As opposed to a piezoelectric sensor, Optrand transducers do not require a separate charge amplifier which results in a considerable saving when using these transducers. Furthermore, the Optrand transducer itself is a cheaper alternative to a Kistler or AVL piezoelectric sensor. It was therefore concluded that the use of an Optrand transducer would result in the least expensive measurement chain and it was consequently decided to rather use an Optrand pressure transducer to measure the in-cylinder pressure of the engine.

The various transducer options available from Optrand were carefully considered based on their pressure ranges, sizes and dynamic behaviour. Finally, the AutoPSI-S miniature transducer was identified as being the preferred choice. This transducer has a pressure range of 0 - 200 bar and a frequency range of 1 Hz to 25 kHz. Its miniature design also allows for easy installation into the cylinder head of the engine.

5.5.2 In-cylinder pressure transducer installation

In order to measure the in-cylinder pressure of the test engine, the Optrand AutoPSI-S miniature pressure transducer was installed into the combustion chamber of the engine. The test engine does not have glow plugs and therefore no existing bore was available to install the pressure transducer. Direct installation of the miniature pressure transducer was also not possible, due to an air channel that had to be traversed before the combustion chamber could be reached (this channel forms part of the cooling system of the engine and transports air forced by

the flywheel fan throughout the cylinder head of the engine). After considering all of the above, it was decided to design and manufacture an adapter sleeve that could be inserted into the cylinder head to house the miniature pressure transducer.

The adaptor sleeve was designed to allow for flush installation of the pressure transducer with the combustion chamber ceiling. This was done to avoid the complications (discussed in section 2.6.3.2 of this report) that are associated with the addition of an indicating channel (which is created when the transducer is not mounted flush with the combustion chamber). Figure 17 shows the fabricated adapter sleeve, as well as the position where the sleeve was installed in the engine's cylinder head.

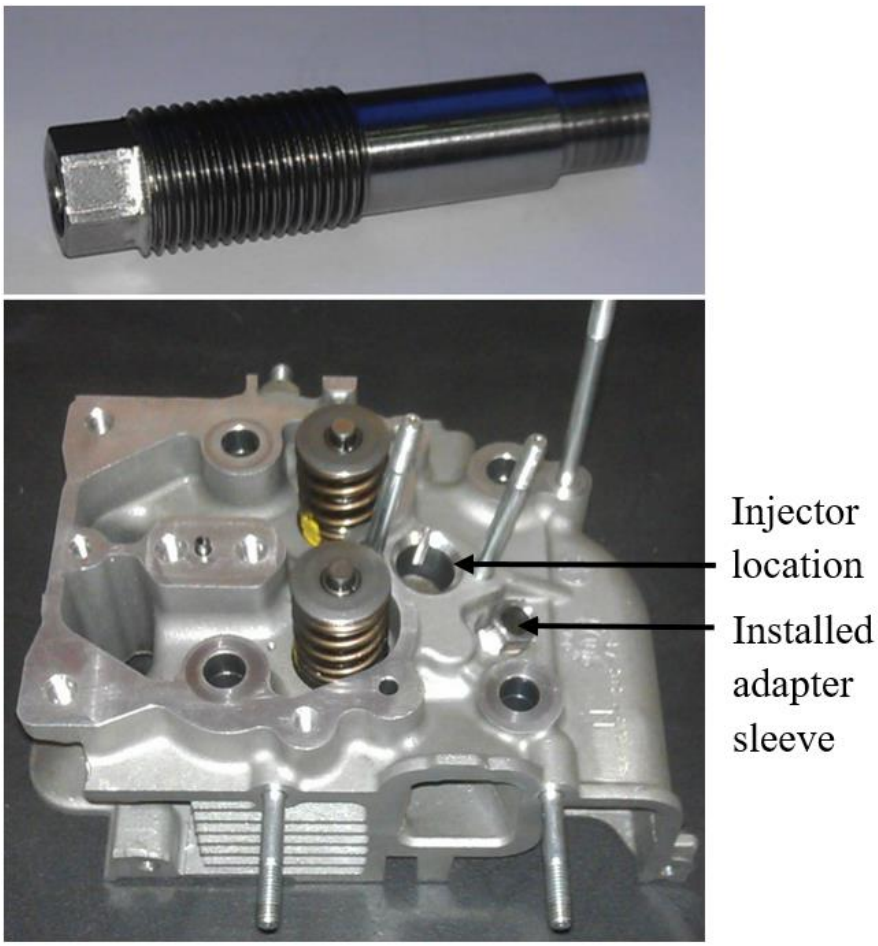

Figure 17: Adapter sleeve (top) and engine cylinder head (bottom)

The adapter sleeve was installed into the cylinder head of the engine after applying Loctite 648 (a high strength, high temperature resistant adhesive) to the threads of the sleeve. The adapter sleeve was also sealed off from the air channel

that it traverses by using an appropriate elastic bonding agent. Finally, the section of the sleeve that protruded into the combustion chamber was machined down to match the contour of the combustion chamber ceiling. Figure 18 shows the bottom view of the machined cylinder head with the adapter sleeve installed.

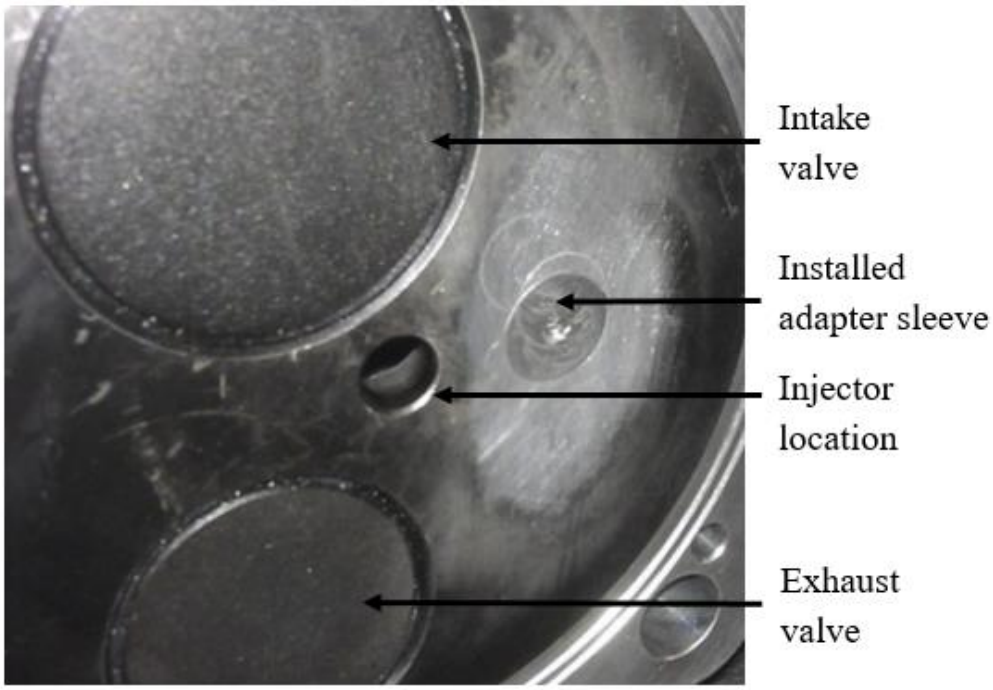

Figure 18: Machined cylinder head with adapter sleeve installed

5.5.3 Intake manifold pressure measurement

The intake manifold pressure was measured using a tapping point in the intake manifold of the engine. Due to the pulsating nature of the flow encountered, a stable pressure reading could not be obtained by measuring directly on the intake manifold of the engine. Consequently, a damping chamber had to be installed to damp out the pressure waves in the measurement line. The pressure reading was then taken after the damping chamber using a WIKA S-10 strain gauge pressure transducer. This transducer has a pressure range of -1 to 3 bar gauge pressure and a 4 - 20 mA output. However, the data acquisitioning unit could only accept voltage inputs and therefore the output signal of the intake manifold pressure transducer was routed to the data acquisitioning unit via a 3104 isolated signal converter from PR Electronics. This signal converter, converted the received 4 - 20 mA signal into a 0 - 10 V signal.

5.5.4 Engine shaft encoder

For the purpose of referencing the in-cylinder pressure to the crank angle position, a Leine Linde RHI 503 incremental shaft encoder was selected. This encoder functions by means of a photoelectric scanning principle. Light is emitted by a LED and passes through a scanning reticle, after which it falls onto a graduated disc. Both the disc and scanning reticle are transparent, while the gratings are either transparent or reflective. As the disc rotates, gratings on the disc move relative to the stationary scanning reticle, causing the intensity of the parallel light which falls onto the disc to be varied (modulated). The changes in light intensity are recorded by photovoltaic cells, which output electrical signals with very accurate signal periods (Encoder Technology - Details and Descriptions, 2014).

The RHI 503 incremental shaft encoder has two output channels (phased by 90 electrical degrees) each of which outputs 3600 pulses per revolution. This translates to a resolution of 0,1 degrees of crank angle rotation. The encoder also has a third reference channel, which outputs a single pulse per revolution. Through proper alignment of the encoder with the engine's crankshaft, this pulse from the reference channel can be used to indicate the position of top dead centre (TDC) in the engine. The RHI 503 encoder was specifically selected for its rugged design, which enables it to withstand higher vibrational loads compared to other encoders. This was particularly important since the encoder is used on the single-cylinder, compression-ignition engine, which is known for generating high levels of vibration during operation. Furthermore, as pointed out by AVL (2002), another advantage of using an optical encoder is that they are less susceptible to electrical interference, which is especially important in the engine testing environment where test cells are often plagued by large amounts of electrical noise.

Brackets for mounting the encoder to the engine were already available, but were modified slightly, to allow for improved alignment of the shaft encoder during installation. A machined flange with a protruding shaft was mounted to the engine's flywheel and clocked up to have a radial run-out of less than 0,015 mm. This high degree of alignment was required in order to limit the amount of stress placed on the shaft encoder's bearing. The encoder was then aligned with this protruding shaft and fastened to a second bracket which secured it to the engine's casing.

5.6 Temperature measurements

Apart from the various instrumentation discussed above, several thermocouples were also installed to measure the following temperatures:

- Ambient air temperature
- Inlet air temperature
- Engine oil temperature
- Supply fuel temperature

- Return fuel temperature
- Exhaust gas temperature

It was decided to standardise on a single type of thermocouple sensor for all the temperature measurements as this reduces the number of types of extension wire and connectors that has to be purchased to only one. This reduces the overall installation cost and also allows for interchange ability of the sensors in the event of sensor failure. Due to the high temperature requirement associated with measuring the exhaust gas temperature (exhaust gas temperature reaches in excess of 600 °C), all temperature measurements were conducted using K-type thermocouple sensors (which has a maximum measureable temperature of 1200 °C).

5.7 Emergency stops and override button

Two emergency stop switches were installed (one inside the test cell on the test bench itself) and another inside the control room. These emergency stops act as master control relays and when activated initiates complete shutdown of the entire test setup. The PLC, however, remains powered during such an event to allow instrumentation readings to be visible. These emergency stops were hard wired and remained latched after being activated. This means that the test setup cannot be restarted until the emergency stop bottom has physically been reset.

The emergency stop inside the control room also employs an override button. When pressed, the override button prevents the control software from shutting down the entire test setup in the event that an alarm has been tripped. The override button thus enables the operator to regain control of the test after the alarm condition has been addressed, thus preventing the test from being stopped abruptly and the data being compromised. Care must be taken to ensure that it is safe to do so before overriding the automated shutdown procedure of the test setup.

5.8 Smoke measurement

Smoke measurements were conducted using an AVL 415 variable sampling smoke meter. Due to the unavailability of a suitable smoke probe, a smoke probe was designed, using the guidelines stipulated in the AVL documentation, which accompanied the smoke meter.

The smoke probe consists of a 8 mm diameter stainless steel tube with a threaded tip, onto which a stainless steel cap is screwed. The cap covers ten equally spaced 3 mm diameter holes (drilled into the 8 mm tube) preventing them from being directly exposed to the soot in the exhaust gas. This cap therefore prevents rapid clogging of the 3 mm sampling holes during testing. The exhaust gas is sampled thought the 3 mm diameter holes and then transported along the inside of the 8 mm tube to outside the exhaust system, from where it is conveyed to the smoke meter via an extension hose. The designed smoke probe can be seen in Figure 19.

Figure 19: Designed smoke probe (bottom) and stainless steel cap (top)

The smoke probe assembly was installed along the centreline of the exhaust pipe in a straight section of the exhaust system. The probe was positioned at least six pipe diameters away from the nearest bend in the exhaust pipe system. This prevents the flow of the gas in the exhaust system itself from influencing the measurement reading (Smoke value measurement with the filter-paper-method, 2005).

5.9 Final test cell layout

The final test facility houses the entire engine test bench with its instrumentation, the fuel supply for the engine, a dynamic fuel flow meter, an exhaust extraction system and the resistive load bank for the dynamometer. The variable speed drive (VSD) unit of the dynamometer, the control cabinet (that houses the programmable logic controller, along with various other controllers) and the computer (that is used to control the entire test setup) are all installed in the control room adjacent to the test cell. From inside the control room the operator can safely conduct all of the required testing, having full control of all equipment, without being required to enter the test cell while the engine is running. The developed test bench can be seen in Figure 20 below.

Figure 20: Developed test bench

6 Control System and Data Logging

This section describes the setup and functionality of the control system hardware and software. The same system was also used to capture and log all engine performance data. Separate hardware and software was, however, employed to perform the high-speed data acquisitioning during the conduction of the engine indicating tests.

6.1 Control system architecture

Figure 21 shows the system architecture that was employed to manage the test setup's control and data logging procedures.

Operator input is provided to a desktop computer, via a graphical user interface known as ETA (Engine Test and Automation). The desktop computer is in turn connected to a programmable logic controller (PLC). Communication between the PLC and desktop computer is handled by RSLinx software and a suitable Allen-Bradley (AB) driver. This communication follows RS-232 protocol. The PLC handles all control and logic operations, as well as accepts inputs and supplies outputs to the various transducers and actuators that form part of the test setup. The dynamometer is controlled by an AB PowerFlex 753 drive unit, which is also connected to the PLC. The PLC supplies set point values to the VSD (using RS-232 protocol) and the VSD then returns the actual measured results to the PLC.

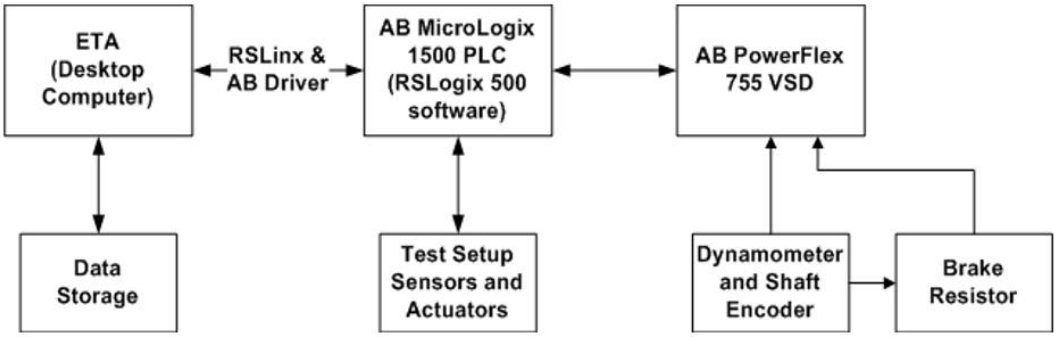

Figure 21: Control system architecture

6.2 Hardware

The control system hardware was installed in the test cell's control room in order to establish a central location from where the entire test setup could be controlled. A control cabinet was set up in the control room into which the following items were installed:

- Fuel flow meter controller
- Throttle actuator controller
- Load cell amplifier
- A current to voltage converter
- AB MicroLogix 1500 PLC with accompanying expansion modules
- Various fuse, relays, power supplies and transformers

6.2.1 PLC hardware

The PLC system consisted of an AB MicroLogix 1500 (1764-24BWA) controller, to which an AB DeviceNet Scanner (1769-SDN) was directly connected (so that it receives power from the backplane of the controller). The DeviceNet Scanner was in turn connected to an AB DeviceNet Adapter (1794-ADN) (through the use of an ethernet connection). Finally, three different expansion modules (comprising of an analogue input, analogue output and a thermocouple module) were connected directly to the DeviceNet Adapter. Following is a more detailed description of the various connections that were made to both the controller and the expansion modules.

6.2.1.1 MicroLogix 1500 controller (1764-24BWA)

Aside from handling all logic operations, the base unit of the MicroLogix 1500 PLC also provided a number of digital inputs and relay outputs. The digital inputs were used to monitor the state of the override button (which is accessible to the operator via the emergency stop inside the control room). Relay outputs were used to control the ignition and starter relay circuits, switch the drive on and off, as well as to set the throttle actuator to the shut-off position. The emergency stop

of the drive was connected in parallel with the ignition relay circuit so that the drive would shut down when the ignition relay coil was de-energised.

6.2.1.2 Analogue output module (1794-OE4/B)

The various terminals of the analogue output module were configured to output either a 0 - 10 V signal or a 4 - 20 mA signal. The module was used to control the position of the throttle actuator, as well as to send the desired speed set point of the dynamometer to the VSD.

6.2.1.3 Analogue input module (1794-IE8/B)

Similar to the analogue output module, the terminals of the input module were configured in the control software to accept either a 0 - 10 V voltage signal or a 4 - 20 mA current signal. Where possible, transducers with a current output signal were selected. This was done due to the current signals proving to be less susceptible to electrical noise, which is quite common in the engine test cell environment.

This module received the following inputs:

- Feedback indicating the actual throttle position.
- The engine oil pressure reading.
- The mass of fuel in the AVL dynamic fuel balance.
- The measured torque (received from the load cell amplifier).
- The actual operating speed of the dynamometer (received as input via the VSD).

6.2.1.4 Thermocouple module (1794-IT8)

From the test setup, the various thermocouples were routed to a junction box installed on the test setup. From the junction box, extension wire was routed to the thermocouple input module on the PLC. The type of thermocouple used was selected in the PLC software and the thermocouple module then provided the cold junction compensation for all the thermocouples internally. Figure 22 below shows the control cabinet which was setup to house the PLC and the various controllers.

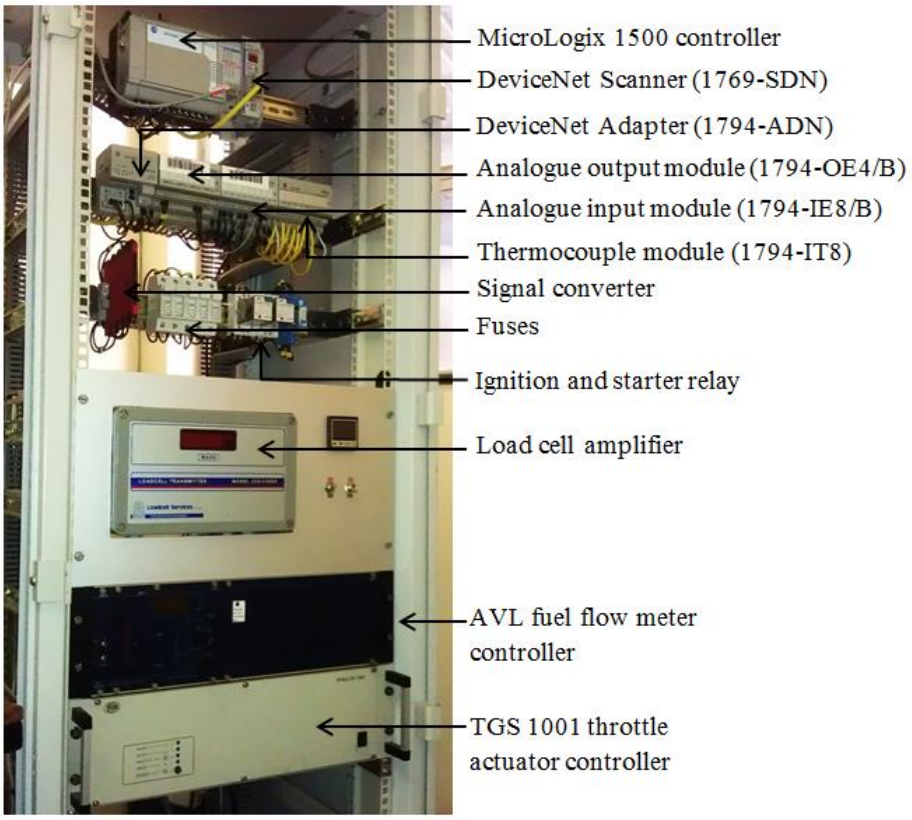

Figure 22: Control cabinet housing PLC and controllers

6.2.2 Allen-Bradley drive (PowerFlex 753 VSD)

An Allen-Bradley PowerFlex 753 VSD was installed to control the speed of the dynamometer. The VSD receives the measured speed of the dynamometer as input form the shaft encoder mounted at the back of the dynamometer. The required speed set point is supplied to the VSD via the PLC. The VSD then compares the actual speed of the dynamometer to the speed set point and alters the rotational speed of the dynamometer accordingly (by altering the amplitude and frequency of the voltage supplied to the dynamometer) in order to match the actual speed of the dynamometer to the supplied speed set point. The power generated by the dynamometer, when operating in absorption mode, was dissipated in a 18 kW, air-cooled brake resistor, which was mounted to the inside of the test cell wall.

6.2.3 Engine pressure indicating hardware

All high-speed data acquisitioning was performed using a National Instruments (NI) 6351 USB data acquisition unit. This unit was employed to capture and log: in-cylinder pressure, intake manifold pressure, as well as the inputs received from the shaft encoder mounted to the test engine. Hardware triggering (output from

the shaft encoder) was used to reference both the captured in-cylinder pressure and intake manifold pressure measurements to crank angle rotation.

By design, the shaft encoder outputs 3600 pulses per crankshaft revolution. When the engine is operated at high idle (3800 rpm), this amounts to a maximum data input rate (to the data acquisitioning unit) of 228 Ks/s. The data acquisitioning unit used has a sampling rate of 1,25 Ms/s single-channel and 1 Ms/s multi-channel (aggregate). Consequently, the in-cylinder pressure, as well as the intake manifold pressure could be sampled (simultaneously) at more than double the maximum data output rate of the engine. Therefore, aliasing was avoided by selecting the sampling frequency in the data capturing software to be at least 500 Ks/s per channel.

6.3 Software

The software for each of the hardware items employed, were programmed and configured to achieve the desired control of the test setup.

6.3.1 PLC software

RSLogix 500 software was used to configure the ladder logic program uploaded to the PLC controller. The program consisted of a main routine (which monitored the status and connectivity of the PLC), as well as various sub-routines (which were called upon by the main routine as required).

The function of the main routine is to monitor the connectivity and status of the PLC, as well as to call the various sub-routines. Different sub-routines were employed to: monitor and pass digital inputs and outputs between the PLC and the graphical user interface (GUI), copy analogue and thermocouple inputs to the GUI, copy set point values from the GUI to the analogue outputs of the PLC, as well as to perform the fuel flow calculations. These sub-routines were customised (in RSLogix 500 software) with the aid of an employee from Sasol Advanced Fuels Laboratory, in order to suit the current test setup configuration and functionality.

Setup of the PLC system was started by configuring the RSLogix 500 software to accept the 1769-SDN DeviceNet Scanner module. RSNetWorx software was then used to register all of the PLC hardware items on the network, as well as to upload the current network configuration to the scanner module. Once the network was established, each of the expansion modules was configured independently, again using RSNetWorx software. Setup of the PLC software was then completed by uploading the final settings to the scanner module.

6.3.2 User interface

A graphical user interface was developed to control the entire test setup by employing a SCADA (Supervisory Control and Data Acquisition) system known as ETA. ETA was developed by Cape Advanced Engineering, specifically for the

engine testing environment. It could therefore be configured to enable complete control of the test setup, while simultaneously allowing the operator to (in real time) monitor all measured variables of the setup. ETA also allows both manual and automated test sequences to be executed based on individual testing requirements. All set point and measured values were passed between ETA and the test setup hardware, via the AB MicroLogix 1500 PLC. Measured variables (such as torque and dynamometer speed) were calibrated directly in ETA. Set point values (such as the throttle actuator position and torque set point) were also calibrated from within ETA. Therefore, the entire measurement chain was included during the calibration process.

Separate test panels were set up in ETA to:

- Control the state of the engine and dynamometer.
- Switch between the different test setup control modes.
- Display all measured variables of the test setup. These included: engine performance parameters, engine operating conditions, ambient testing conditions, as well as the state of various auxiliary equipment.
- Visually monitor engine performance parameters, engine operating conditions and ambient conditions.

The graphical user interface can be seen in Appendix G.

6.3.3 Engine pressure indicating software

All engine indicating related measurements were captured and logged with the use of LabVIEW software and the hardware discussed in section 6.2.3. Within LabVIEW a customized VI (Virtual Instrument) was programmed that could capture both the intake manifold and in-cylinder pressure measurements. Hardware triggering was implemented (through the use of the shaft encoder attached to the engine's crankshaft) to start the logging process, as well as to determine the time increments at which the pressure measurements were captured.

6.4 Control system operating modes

From within ETA, the test setup can be operated in either torque control or speed control mode. The operating mode of the control system can be selected by the user and is based upon the type of engine test to be performed.

6.4.1 Constant torque mode

In this control mode, the operating condition of the engine is controlled as is shown in Table 3 below. Constant torque mode is used whenever partial load testing is to be performed. It is, however, also possible to perform partial load testing using constant speed mode (discussed in the next section of this report). During partial load testing the operating point of the engine is fixed by supplying both a speed and a torque set point value, after which the control system regulates

the throttle position of the engine in order to maintain the engine at the specified operating point.

Table 3: Constant torque mode

Speed	Set point provided as input by the operator.
Torque	Set point provided as input by the operator.
Throttle	Adjusted by the control system.

6.4.2 Constant speed mode

In this control mode, the operating point of the engine is fixed by altering the engine parameters as is shown in Table 4 below. This mode of control lends itself towards testing at full load conditions during which a constant speed set point is selected and the engine's throttle is set to the wide open position. The amount of torque placed on the engine is then altered by the control system in order to maintain the engine speed at the specified speed set point.

Table 4: Constant speed mode

Speed	Set point provided as input by the operator.
Torque	Varied by control system (as the throttle setting is changed by the operator) in order to maintain the speed as per the speed set point.
Throttle	Adjusted manually by the operator.

7 Commissioning of Test Setup

This section details the procedures implemented in order to validate the dynamometer design, as well as to calibrate the various sensors and actuators. Furthermore, this section also focuses on the accuracy and stability of the test setup's control system, before finally addressing the repeatability of the test setup.

7.1 Validation of dynamometer design

After integrating the newly designed dynamometer, a static calibration was performed in order to ensure that the dynamometer measured the torque accurately. The calibration results were analysed to verify that the dynamometer has a linear output response and that it displays a limited amount of hysteresis when loaded and unloaded. Finally, the repeatability of the dynamometer system was also validated.

Figure 23 below shows the results obtained during a calibration cycle prior to starting the engine. The figure presents the applied torque (shown on the vertical axis) plotted against the measured voltage output (shown on the horizontal axis). After the data points were plotted, a first-order polynomial was fitted to the data using the method of least squares.

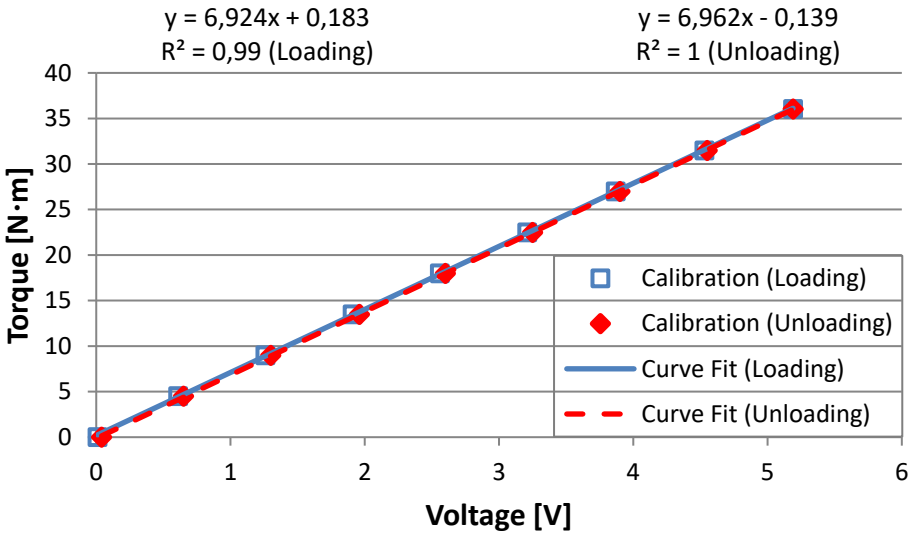

Figure 23: Dynamometer linearity

The coefficients of determination (R^2) of the curve fits in Figure 23 are 0,99 and 1 for the cases of loading and unloading the dynamometer respectively. This verifies that a first-order polynomial can be used to represent the measured data exceptionally well and therefore also confirms that the output of the dynamometer is linear over the measured range. Furthermore, from Figure 23 it can also be observed that the dynamometer displays almost zero hysteresis. Comparing the two measured datasets (loading versus unloading), there is only a 0,1 N·m difference in the zero offset. Simultaneously, the percentage difference between the remaining data points are, on average, less than 0,3 %. The small amount of hysteresis confirms the sound design and alignment of the trunnion bearings. It also confirms that the amount of friction present in the system is acceptably small.

Finally, the repeatability of the dynamometer was tested using a hot setup with calibration being performed pre- and post-testing of the engine. The test setup was run until the engine reached operating temperature (this being determined by monitoring the engine's oil temperature), after which the first calibration was performed. The results of this calibration are presented as the data points labelled "Calibration (Pre-Testing)" in Figure 24 below. The engine was then tested over a range of partial load points at various engine speeds, after which the setup was shut down and the dynamometer calibration was performed once more to obtain the results labelled "Calibration (Post-Testing)" which are also presented in Figure 24.

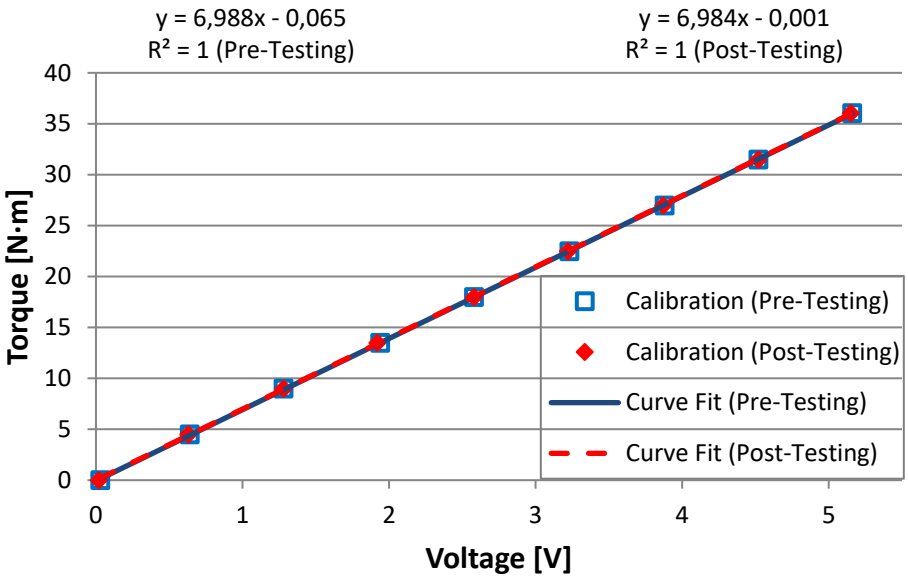

Figure 24: Dynamometer repeatability

From Figure 24 it is clear that the dynamometer displays excellent repeatability with the output being linear across its measurement range (the R^2 values for both curve fits are 1). The pre- and post-testing calibration results display 0 N·m difference in the zero offset, which is extremely good. Furthermore, comparing the polynomial coefficients of the curve fits in Figure 24 to those of the curve fits in Figure 23, also shows very good correlation of the calibration results obtained with a hot and cold setup. Considering the good repeatability shown above, along with the linear output and negligible amount of hysteresis exhibited by the complete dynamometer system, it was concluded that the dynamometer design was acceptable and it was consequently signed off for testing. The data that was used to produce Figure 23 and Figure 24 can be found in Appendix K).

7.2 Calibration of instrumentation and actuators

Prior to starting any tests, all pressure transducers and thermocouples were calibrated. This section summarises the calibration procedures followed. The details surrounding the execution of these processes, along with the results that were obtained, are presented in Appendix H.

7.2.1 Throttle actuator calibration

The Posicon 1000 throttle actuator system leaves the factory fully calibrated and does not require recalibration when installed. It was, however, required to set the amount of force exerted by the actuator (this is selected as a percentage of the nominal force rating of the actuator). Apart from the force setting, it was also

required to set the fixed positions for “shut off”, “idle”, and “maximum throttle”. These settings were all performed by following the procedure detailed in the throttle actuator’s user manual.

The final step was to calibrate the feedback signal from the actuator (this was performed directly in ETA) in order to determine the actual position of the actuator from within ETA. During this process, the actual position of the actuator was verified using the hand held remote terminal of the actuator, which displays the actual position of the actuator as a percentage of the stroke between the predefined “idle” and “maximum throttle” positions.

7.2.2 Fuel flow meter calibration

The AVL dynamic fuel balance was calibrated upon installation following the detailed calibration procedure in the fuel flow meter’s user manual. The calibration procedure was directly performed from the fuel flow meter’s control unit. Once the calibration requirements stipulated in the fuel flow meter’s user manual were met, the output from the fuel flow meter’s control unit was calibrated directly in ETA. This ensured that the entire measurement chain was included in the calibration process and that the fuel flow rate displayed in ETA was synchronised with the flow rate displayed by the fuel flow meter’s control unit. Refer to Appendix H.4 for the detailed calibration procedure implemented.

7.2.3 Pressure transducer calibration

7.2.3.1 In-cylinder pressure transducer

During the calibration of the Optrand transducer, a WIKA CPB 3000 dead weight tester was used to apply a known pressure to the sensor. In an effort to achieve the best possible accuracy during the calibration process, the wiring setup, hardware equipment and data logging software was implemented in exactly the same way it was to be used to log data during the engine tests. During calibration, the sensor was electrically connected to the NI 6351 USB data acquisition unit and the sensor output was recorded using LabVIEW software. Refer to Appendix H.2.1 for the calibration results obtained.

7.2.3.2 Intake manifold pressure transducer

The measurement range of -1 to 3 bar gauge pressure of the WIKA S-10 strain gauge pressure transducer required that the sensor be exposed both to vacuum and positive gauge pressure during calibration. The senor was calibrated while being electrically connected exactly the same way it was to be used in service, but without being connected to the damping chamber. The reason for excluding the damping chamber during calibration was due to the chamber adding too much volume to the measurement line, which made it difficult to achieve the required vacuum pressure using the available calibration equipment.

The sensor was calibrated over a pressure range of -0,6 to 1 bar, using a pressure pump from SI Pressure Instruments and a WIKA reference gauge. The upper

range of the calibration was restricted to 1 bar due to the test engine not employing force induction. Consequently, the mean intake manifold pressure will not rise higher than atmospheric pressure. The calibration results are presented in Appendix H.2.2.

7.2.3.3 Oil pressure transducer

The A-10 pressure transducer which was used to measure the engine oil pressure was supplied with a calibration certificate. The sensor supplier is ISO certified, therefore the sensor was installed as supplied and the provided sensitivity from the calibration certificate was used to determine the measured pressure. The measurements obtained from the oil pressure sensor is purely for monitoring purposes (in order to verify that there is sufficient oil pressure during start-up and that the oil pressure reading does not abruptly change during operation), therefore using the sensitivity provided on the sensor's calibration certificate was deemed fit for the purpose.

7.2.4 Temperature sensor calibration

A Fluke 9142 field metrology well was used as heat source during the calibration of the thermocouple sensors. The reference temperature measurement was obtained by employing a calibrated platinum resistance thermometer in conjunction with the field metrology well.

Prior to performing the calibration, the thermocouples were installed as part of the test setup and all the associated wiring to the measurement equipment completed. The thermocouples were then removed from the test setup, with all of their respective wiring harness in place as they would be used as part of the test setup. The sensors were then calibrated with the output values being captured directly in ETA. The field metrology well has a temperature range of -25 °C to 150 °C and the thermocouples were calibrated over a temperature range of 0 °C to 140 °C with data points captured every 20 °C. Upon reaching each of the temperature set point values, the heat source, reference temperature probe and thermocouples were allowed to stabilise before the data was captured. Calibration cycles were performed both while increasing and decreasing the temperature, after which the averages of the measured results were calculated. A first order polynomial was then fitted to the data and used as a calibration curve. Refer to Appendix H.3 for the detailed calibration results.

7.3 Stability and accuracy of test setup

Due to the implementation of a new control system and new control hardware, an initial test sequence was executed during which the PID settings of the entire control system were set. Preliminary testing was then performed, over multiple days, in order to monitor the control stability of the test setup. These tests also served the purpose of identifying the most suitable speed and load points at which to conduct future engine tests.

In order to obtain an accurate indication of the engine's performance, the aim was to select speed and load points which were representative of the engine's normal operating range. The final test points were identified by evaluating the engine's performance curves (see Figure 53 in Appendix I) and selecting the load points such that they all fall within the engine's torque output capability over the selected speed range. Following this selection procedure, preliminary test points were identified as being: 5, 10, 15 and 20 N·m at 2400 rpm, 2800 rpm and 3200 rpm respectively. These test points therefore also cover the 3000 rpm operating point of a 50 Hz generator, which is a typical application in which the test engine is commonly used. The test points are shown in Figure 25 where the torque is plotted against engine speed (shown in rpm on the horizontal axis). In addition, Figure 25 also displays the peak torque curve of the test engine as obtained from the engine manufacturer's data.

An automated test sequence was then programmed in ETA and executed using constant torque mode. The engine was started and allowed to reach operating temperature, after which the automated test was initiated. The automated test was started at a load of 5 N·m and a speed of 2400 rpm (test point 1 in Figure 25). The engine was run at each this test point for 2 minutes (the amount of time required for the engine's exhaust gas temperature to stabilise), after which sixty data points were then captured over a period of five minutes. Upon completion of the data capturing, the automated test moved the test engine on to the second test point (10 N·m at 2400 rpm). After the test point was reached, the engine was run once more until the exhaust gas temperature stabilised and the sixty data points were captured again. This process was repeated to sequentially complete all the test points in the order shown in Figure 25, without any intervention from the operator.

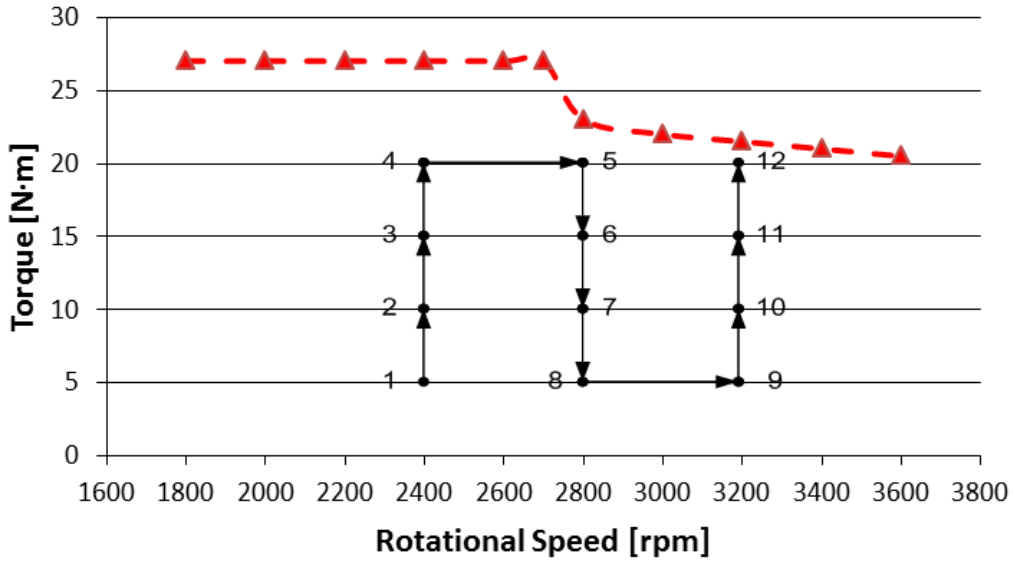

Figure 25: Test points used during testing

The results of the test are presented in Figure 26, where the measured torque is plotted for each captured data point. The data presented are the raw data points as they were captured (over a period of 5 minutes) and without correcting the torque for ambient conditions. From Figure 26 it is clear that the test setup exhibits very good control stability across all test points, especially considering the fact that the test engine used is a single-cylinder, compression-ignition engine, which is known for torsional oscillations.

The largest deviation in load, can clearly be noticed for all test points conducted at a test speed of 2800 rpm, with the highest deviation being recorded at test point number 5 (20 N·m at 2800 rpm). These more noticeable deviations in load can be attributed to the engine's torque characteristic displaying significant torque backup around 2800 rpm (as can be seen from the steep gradient in the full load torque curve presented in Figure 25 above). As a result, when running at an operating speed of 2800 rpm, any small deviation in speed, results in a significant change in fuel delivery and therefore torque output of the engine. The change in torque output of the engine causes the engine's speed to change even more, forcing the control system to respond by changing the load on the engine, in order to bring it back to the set point values for the specific test point. The repetition of the above sequence of events, is the cause of the larger deviations in torque output for test points conducted at speeds of 2800 rpm.

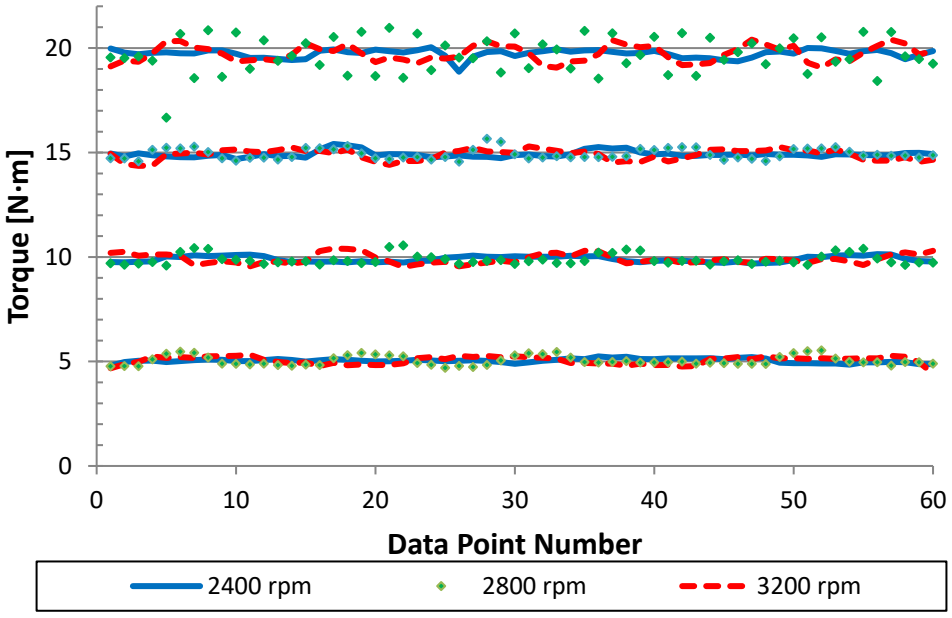

Figure 26: Test setup control stability over period of 5 minutes

Table 5 was constructed in order to quantify the accuracy of the data presented graphically in Figure 26. Statistical analysis was performed which yielded the mean and standard deviation values (for both load and speed) for each of the recorded data sets. The results of which can be seen in the last four columns of Table 5. Further inspection of the results reveals that the mean torque values are all within the initial stipulated ± 0,5 N·m tolerance band, listed in Table 1. This also holds for test point 5, where even with the larger deviations due to the reasons discussed in the paragraph preceding Figure 26, the value of the mean torque recorded is still within 0,4 N·m of the set point value of 20 N·m. Table 5 also indicates that the mean speed values obtained are all within 5 rpm of the set point value and therefore far exceed the ±1 % speed control accuracy requirement, listed in Table 1. Overall, the stability and accuracy of the entire test setup (including the control system) proved satisfactory and the stipulated design requirements were met successfully. Note that test point 1 was repeated at the end of the test cycle in order to compare the test setup accuracy before and after completing the entire test cycle.

Table 5: Control system accuracy

Test Point #	Test Point (Set Point Values)	Mean Torque [N·m]	Mean Speed [rpm]	Load	Speed
				Standard Deviation [N·m]	Standard Deviation [rpm]
1	5 N·m at 2400 rpm	5,0	2400	0,1	0,6
2	10 N·m at 2400 rpm	9,9	2402	0,1	0,7
3	15 N·m at 2400 rpm	14,9	2403	0,1	0,9
4	20 N·m at 2400 rpm	19,7	2404	0,2	1,0
5	20 N·m at 2800 rpm	19,6	2804	0,9	2,7
6	15 N·m at 2800 rpm	14,9	2805	0,3	0,5
7	10 N·m at 2800 rpm	9,9	2802	0,3	0,4
8	5 N·m at 2800 rpm	5,0	2800	0,2	0,3
9	5 N·m at 3200 rpm	5,0	3198	0,2	0,2
10	10 N·m at 3200 rpm	9,9	3200	0,2	0,2
11	15 N·m at 3200 rpm	14,9	3202	0,3	0,2
12	20 N·m at 3200 rpm	19,7	3205	0,4	0,3
13	5 N·m at 2400 rpm	5,0	2402	0,1	0,6

Data obtained by Corbett (2017), who used the test bench developed in this project to perform testing of the larger Honda GX670 spark-ignition engine,

shows that the dynamometer also displays very good control stability when testing at higher load points, as can be seen in Figure 27 below. This verifies that the developed test bench and dynamometer system meets the control accuracy requirements initially stipulated in Table 1, where the test setup was designed with the purpose of also being suitable to test the larger Honda, spark-ignition engine.

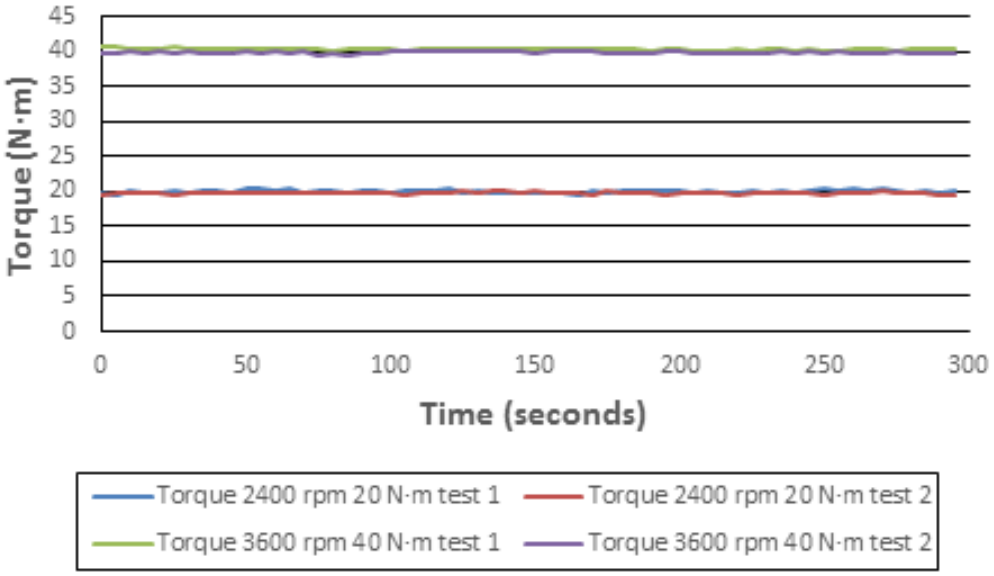

Figure 27: Test setup stability when testing Honda, spark-ignition engine

(Source: Corbett, 2017)

7.4 Repeatability

In order to verify the repeatability of the test setup, it was decided to monitor brake specific fuel consumption (BSFC) and exhaust gas temperature over four different load points, each of which were tested at three different speeds (test points 1 through 12 in Table 5). During these tests, 50 ppm diesel was used as fuel and differences in ambient conditions were accounted for by applying the SAE J1349 power correction factor (SAE J1349 Standard, 2004). Comparing the BSFC results of the two tests, showed a percentage difference of 1,6 % (on average). The difference in exhaust gas temperature results for the same tests, showed a percentage difference of 3,2 % (on average) when comparing the results of the first test, to that of the second. The inlet air temperature recorded during these tests displayed an average difference of 2,7 °C between tests 1 and 2. The results obtained are presented in Figure 28 and Figure 29 respectively, where the measured values have been plotted against BMEP. The measured test data which is presented graphically in this section can be found in tabulated form in Appendix K.

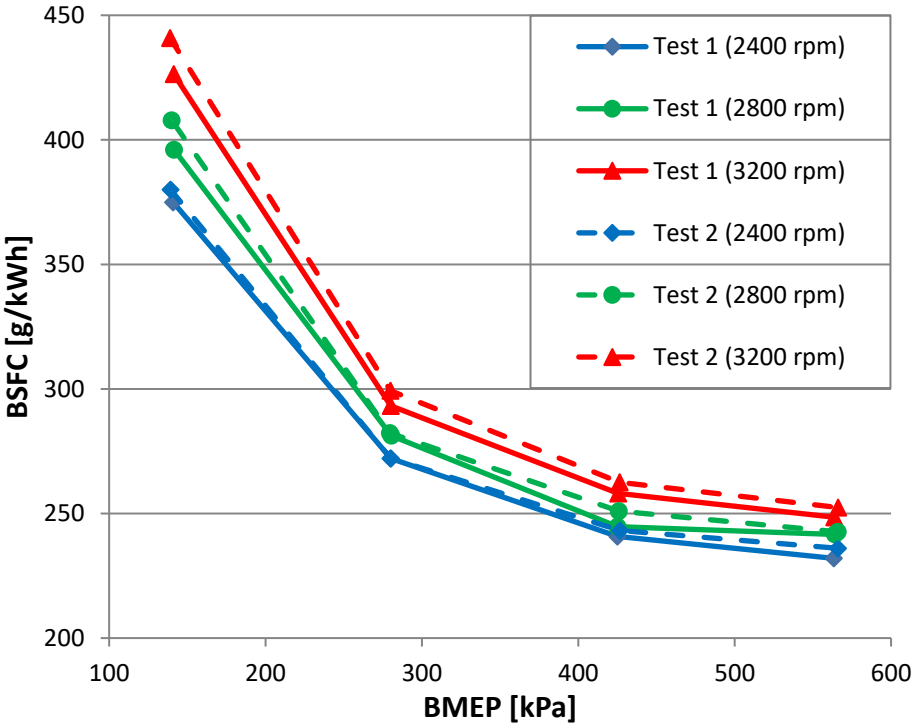

Figure 28: BSFC versus BMEP

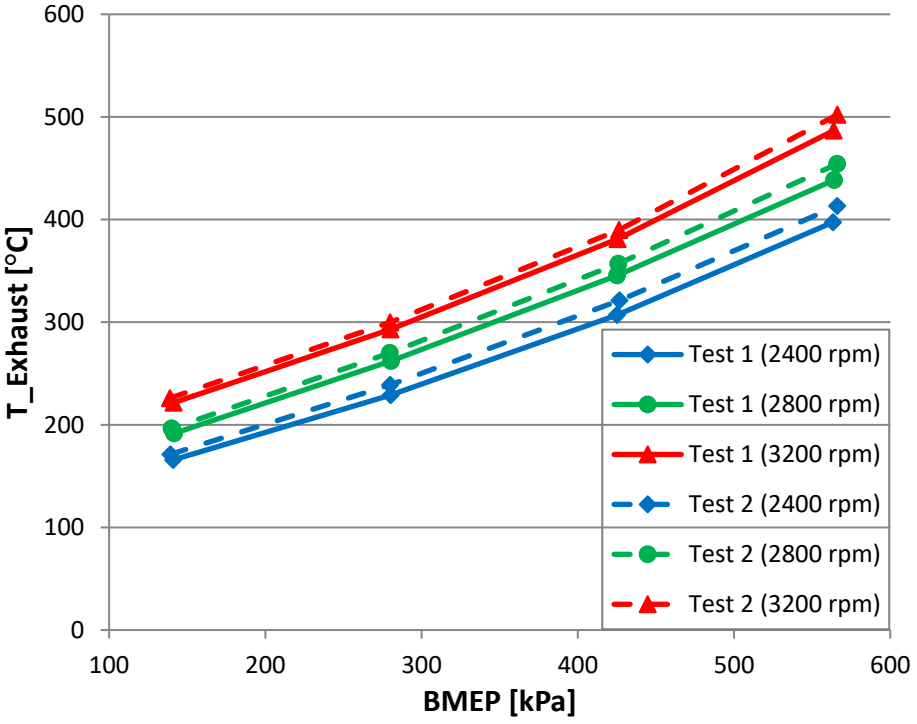

Figure 29: Exhaust gas temperature versus BMEP

8 Engine Performance Testing and Results

After commissioning of the test setup, during which the repeatability of the entire test setup and measurement system was confirmed, the engine performance tests were started.

The first part of the engine performance testing, consisted of full load testing using 50 ppm diesel as fuel. Following these tests, partial load testing was performed in order to investigate the effects on engine performance when using a B10 biodiesel blend (10 % by volume biodiesel blended with 90 % by volume petroleum diesel) as opposed to 50 ppm diesel. The source of the biodiesel was fatty acid methyl esters produced from palm-based cooking oil. The pure biodiesel was sourced from a biofuel supplier and the B10 blend was then produced through splash blending.

The original engine manufacturer confirmed that the highest percentage of biodiesel previously tested in the engine was 7 % (before modifications were required to the fuel injection equipment), but it was decided to use a B10 blend in an attempt to be able to detect a noticeable difference in the test results when comparing B10 to petroleum diesel.

Prior to conducting each of the engine tests, the dynamometer was calibrated to ensure that the measured torque was accurate. Furthermore, a second calibration sequence was also performed after completion of each test. This was done to verify that there was no drift in the calibration during the logging of the test data.

8.1 Full load testing

A full load test was performed prior to starting the engine performance testing. The result from the full load test was used to establish a baseline for the performance of the test engine. After completing the full load test, all of the engine performance tests were conducted. At the end of the entire test program (multiple days later), a second full load test (the bracket test) was performed. The results of the two full load tests were then compared to each other in order to ensure that the engine still made the same amount of power after completing the entire test program. Thus, verifying that the performance of the engine itself remained unchanged throughout the duration of the engine test program.

The results of these two full load tests are presented in Figure 30 below. Figure 30 shows both the full load torque and power curves. The measured parameters were plotted against engine speed, with all full load tests being conducted over a speed range of 2400 - 3600 rpm. Note that the horizontal axis in Figure 30 starts at a speed of 2200 rpm.

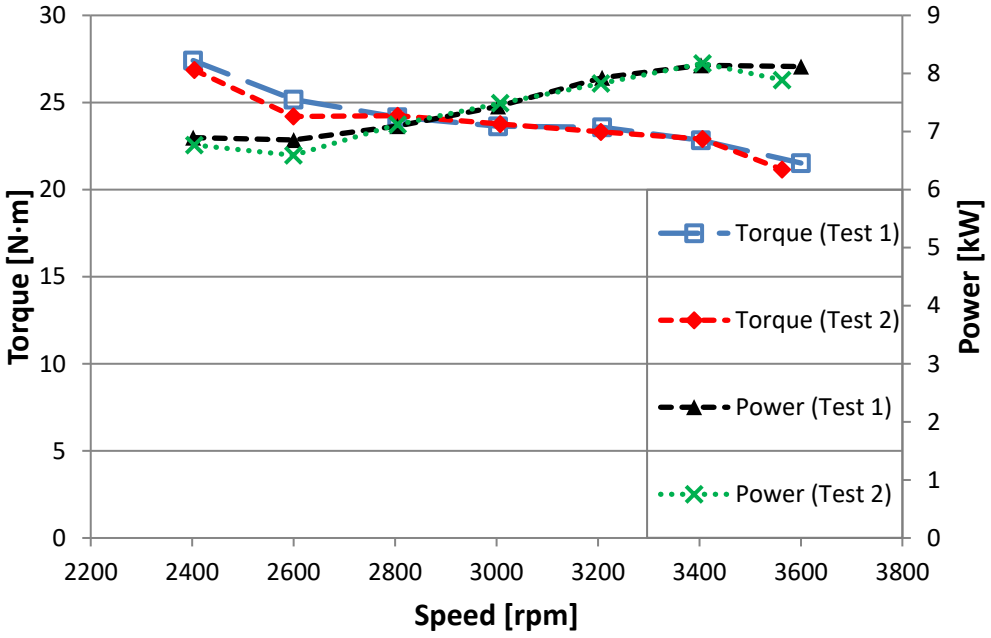

Figure 30: Torque and power curves pre- and post-testing

In Figure 30 it can be seen that the results from the second test compare very well to that of the first full load test, even though these two tests were conducted multiple days apart. The largest discrepancy (less than 1 N·m) occurs at a speed of 2600 rpm. Further investigation revealed that the difference was due to a slightly higher fuel consumption rate during the first test. This can be attributed to increased fuel delivery which is controlled by the engine's internal control system (over which the test setup has no control). Apart from the slight discrepancy in the data at 2600 rpm, the remaining data points were all within 0,5 N·m of each other. Similarly, the two power curves shown also correspond very well with the same trends being visible as can be observed from the torque data.

Both the torque and power data in Figure 30 indicate that during test 2, the highest speed that the engine could achieve (under full load conditions) was slightly lower (at 3560 rpm) than the speed of 3600 rpm achieved during test 1. This difference is due to the influence of the mechanical governor (which exhibits a 5 % speed droop in order to ensure stable speed control). It was ensured that the throttle was always at the wide open throttle position during the full load tests. The changes in the performance curves are therefore not related to a change in throttle actuator input. The difference in output observed can only be due to hysteresis in the governor, or due to a change in the governor springs. This was left untouched, because it was decided beforehand not to make any changes to the engine's fuel delivery system.

Figure 31 below shows the governor droop which was measured during the second full load test. Multiple data points were captured near the breakaway point

(at 3600 rpm) in an effort to capture the drop-off. Governor droop was, however, not measured during the first test, due to no governor breakaway being present at the time.

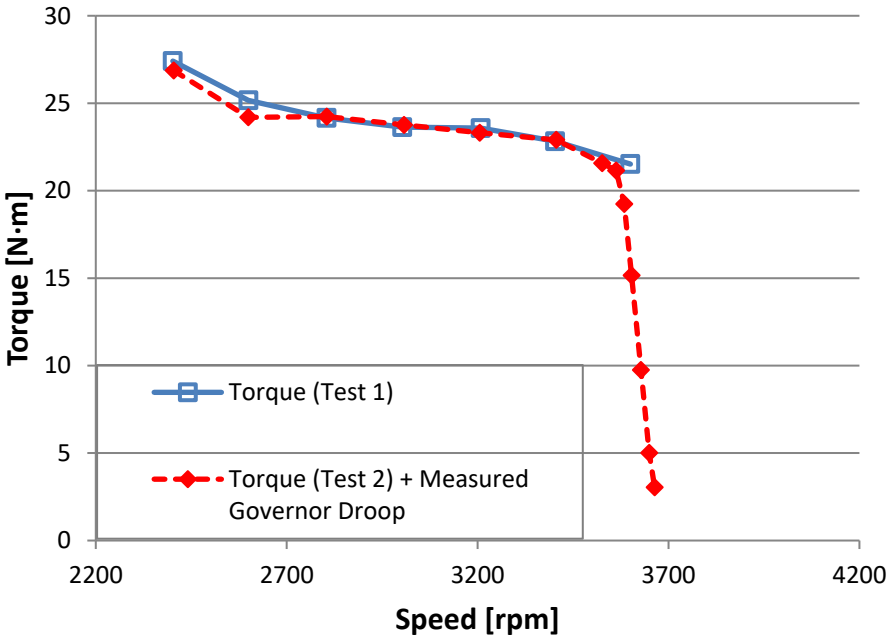

Figure 31: Measured governor droop

8.2 Partial load testing

Partial load tests were also conducted in order evaluate the effect that the use of a B10 biodiesel blend has on the performance of the test engine. In order to report the findings, BSFC was chosen as the parameter to quantify the effect on engine performance.

Test points 1 through 12 in Table 5, the same test map previously used to test for repeatability, was also used to conduct the fuel-to-fuel evaluations. Figure 32 shows the BSFC values (presented in g/kWh) recorded for both diesel and B10 when exposed to the above-mentioned test map. The BSFC values were plotted against BMEP, which is plotted in kPa on the figure's horizontal axis.

From the results it is clear that the trend is that across the various load points B10 results in higher BSFC values. This corresponds with what is found in the literature and can be attributed to the lower energy content and higher density of biodiesel compared to that of petroleum diesel (Aziz *et al.* 2006) (Ozsezen & Canakci, 2011). The measured data used to construct Figure 32 can be found in Appendix K.

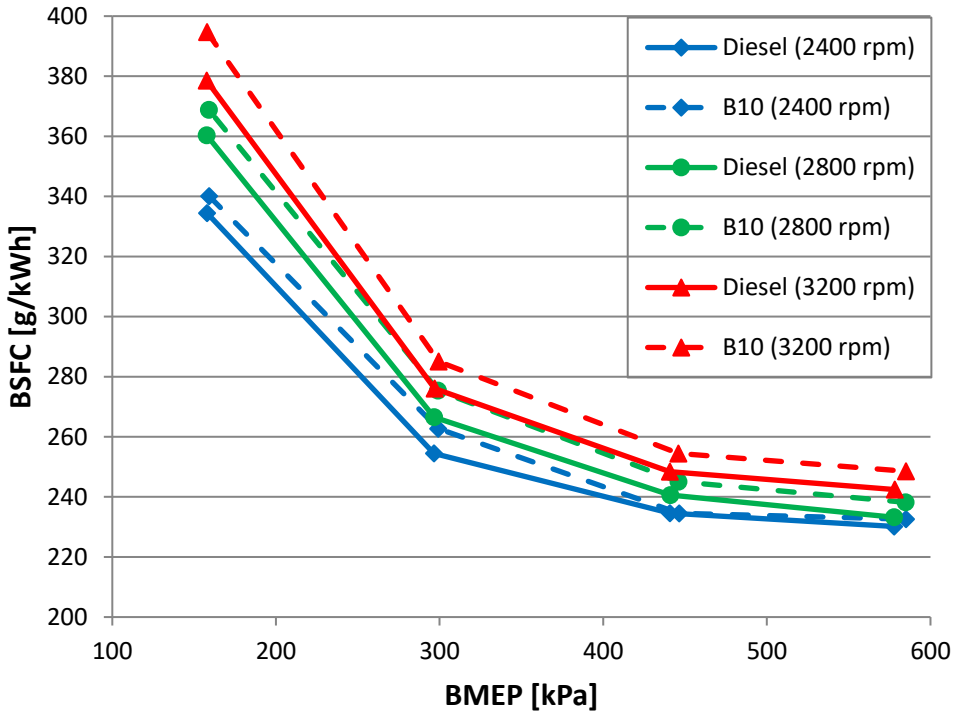

Figure 32: Effect of B10 on BSFC

The diesel BSFC results shown in Figure 32 differ somewhat from those presented in Figure 28, with the discrepancy being most noticeable at low load conditions. The results consistently display improved correlation as the load is increased. The data presented in the two figures were captured multiple days apart with the test setup being subjected to numerous hours of testing in-between. Any small change in friction (during this hours of testing) along the driveline would result in a change in the fuel consumption of the engine (to compensate for the change in friction) when the engine is required to repeat the predefined test point. The small change in friction would not be measured by the load cell and would therefore result in different BSFC results being obtained. This explains why the differences in the BSFC results are most noticeable at low load (where the change in friction makes up for a larger percentage of the load applied by the dynamometer). In both cases, however, the test setup continued to display very good repeatability.

8.3 Smoke measurement

During the conduction of the partial load tests, smoke measurements were taken to evaluate the amount of soot present in the engine's exhaust gas. The effect on the amount of soot particles present was evaluated by monitoring the change in filter smoke number (FSN). The results obtained displayed good repeatability,

with measurements for consecutive tests showing variances as low as 0,02 in FSN (on average).

Comparing the effect of the use of B10 biodiesel to that of 50 ppm diesel, it was found that although the influence of B10 is very small, the biodiesel produces the same (to within 0,01 FSN) or lower FSN values compared to 50 ppm diesel. This can be seen in Figure 33 below (where the filter smoke numbers have been plotted against BMEP).

This observed reduction in soot content can be attributed to the higher oxygen content of biofuel (compared to the oxygen content of petroleum diesel) which leads to improved and more complete combustion. This in turn results in reduced soot particles being present in the engine's exhaust gas and corresponds with what is reported in the literature (Aziz *et al.* 2006) (Gopinath & Sundaram, 2015) (Ozsezen & Canakci, 2011).

A significant discrepancy was, however, obtained at a BMEP of 578 kPa and a speed of 2800 rpm where the use of B10 biodiesel resulted in a higher FSN compared to 50 ppm diesel. This data point is inconsistent with the rest of the results obtained and could unfortunately not be repeated, due to a faulty smoke meter (the cause of which was later identified as being a dry solder joint). However, the integrity of the data was not compromised, as the smoke meter performs a self-calibration check prior to taking each measurement. The measured data used to construct Figure 33 can be found in Appendix K.

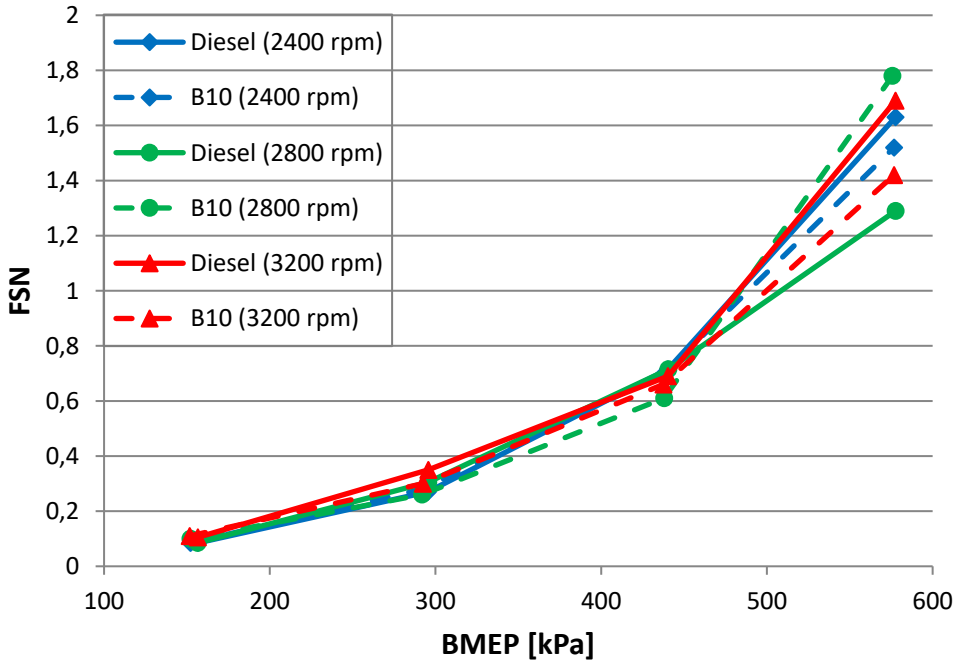

Figure 33: Effect of B10 on FSN

9 Engine Indicating Testing and Results

During the engine indicating tests, crank angle based measurements of the intake manifold pressure and in-cylinder pressure were recorded. The recorded data was then analysed and used to construct a zero-dimensional, single-zone, heat release model of the engine.

9.1 Testing and data capturing

Prior to starting any of the tests, the incremental shaft encoder on the engine was mechanically aligned relative to the crankshaft of the engine. The purpose of the exercise was to align the encoder such that its trigger pulse was as close as practically possible to coinciding with the TDC position of the piston (just prior to the start of the intake stroke).

Using the partial load test map presented in Figure 25, test points numbers: 1, 4, 9 and 12 from Table 5, were selected to be used during the engine indicating tests. These particular test points were selected to monitor the effect that high and low load, as well as, high and low speed, have on the engine indicating measurements.

Testing was started by performing motoring tests at the preselected speeds of 2400 rpm and 3200 rpm, with the entire test setup at normal operating temperature. Due to heat losses and leakage being more significant for a hot engine, it is important that the data be captured while the engine is at its normal operating temperature.

During each test, 500 cycles of both in-cylinder and intake manifold pressure were captured simultaneously for each run. The larger number of cycles was chosen, due to the inherent cycle-to-cycle variation associated with the single-cylinder, diesel engine (as discussed in section 3.3). Furthermore, capturing a larger number of cycles requires no additional effort from an engine testing point of view, it only leads to larger data files during post processing. The pressure data was then averaged over the 500 cycles in order to eliminate as much of the cycle-to-cycle variation of the engine as possible. As pointed out by Lancaster *et al.* (1975) averaging the measured pressure data over a number of cycles is an acceptable procedure. Statistically, the variance associated with the measured average pressure reduces as the number of samples (the number of engine cycles) used to calculate the average pressure is increased.

Due to the high degree of cyclic variation of the single-cylinder engine, as well as due to the employment of the variable speed drive to control the electric dynamometer, the measured pressure signal still exhibited a substantial amount of high frequency noise. Consequently, a low pas filter was constructed using the fdatool in Matlab, after which the pressure data was filtered using the filtfilt function in Matlab. This function was best suited to the application as it filtered the data both forwards and backwards, eliminating any phasing of the data during the filtering process. The cut-off frequency of the filter was chosen such that no

clipping of the peak pressure occurred. Therefore, the integrity of the pressure data remained intact after the filtering process.

9.2 Referencing and phasing

In order to reference the in-cylinder pressure, the measured intake manifold absolute pressure (MAP) was averaged over 6 degrees of crankshaft motion (from 3 degrees before bottom dead centre (BDC) to 3 degrees after BDC) (Zhoa & Ladammatos, 2001). This then gave the average MAP at BDC between the intake and compression stroke for the particular load and speed. The in-cylinder pressure (over this same range of crankshaft motion) was then pegged at this calculated averaged MAP.

Final and accurate phasing of the pressure data was performed using the procedures described in section 2.7.2. This consisted of plotting the log P - log V diagram of the measured data and using the shape of the curve (more specifically the straightness and slope of the compression line) in order to verify accurate phasing of the data. The initial mechanical alignment of the encoder (discussed in the previous section) meant that only a small amount of additional phasing was required. The guidelines given by Zhoa & Ladammatos (2001) was used to perform the phasing until a straight compression line was obtained, having a slope of $-n_p$ and the shape of log P - log V diagram displayed a sharp and distinct tip at TDC (as can be seen in Figure 34). In addition, the pressure curve was also examined in order to ensure that the crank angle at which the peak pressure occurs precedes TDC, as is explained in the literature (Zhoa & Ladammatos, 2001) (Lancaster *et al.* 1975).

9.3 Motoring test results

Table 6 below shows the peak pressure, as well as the crank angle position where the peak pressure occurred, for the motoring tests conducted at 2400 rpm and 3200 rpm. It was found that the peak pressure occurs prior to the piston reaching TDC and that the angle with which the peak pressure precedes TDC, decreases from 0,2 to 0,1 degrees when the engine speed increases form 2400 rpm to 3200 rpm. This agrees very well with what is reported in the literature by Zhoa & Ladammatos (2001). Furthermore, equation (2.1) was solved for n_p, in order to calculate the value of the polytropic exponent (for the compression stroke) when using the measured test data. The measured values of P_{max} and P_{IBDC}, as well as the value of the compression ratio (r_c), was then substituted into the equation, which yielded the results shown in the last column of Table 6. Here it can be seen that values of 1,3 and 1,32 were obtained for the polytropic exponent, corresponding to test speeds of 2400 rpm and 3200 rpm respectively. This falls well within the range of 1,25 to 1,35 that is reported in literature by Lancaster *et al.* (1975) and Stone (1992).

Table 6: Referenced and phased data of motoring tests

Test Description	P_{max} [kPa]	Position of P_{max} [Degrees before TDC]	Polytropic Exponent (n_p)
Motoring at 2400 rpm	4896	0,2	1,30
Motoring at 3200 rpm	5084	0,1	1,32

Figure 34 below, shows the phased pressure versus volume diagram, for the motoring test conducted at 3200 rpm. The data is plotted on axes having a logarithmic scale, with the pressure presented in kilopascals and the cylinder volume in cubic meters.

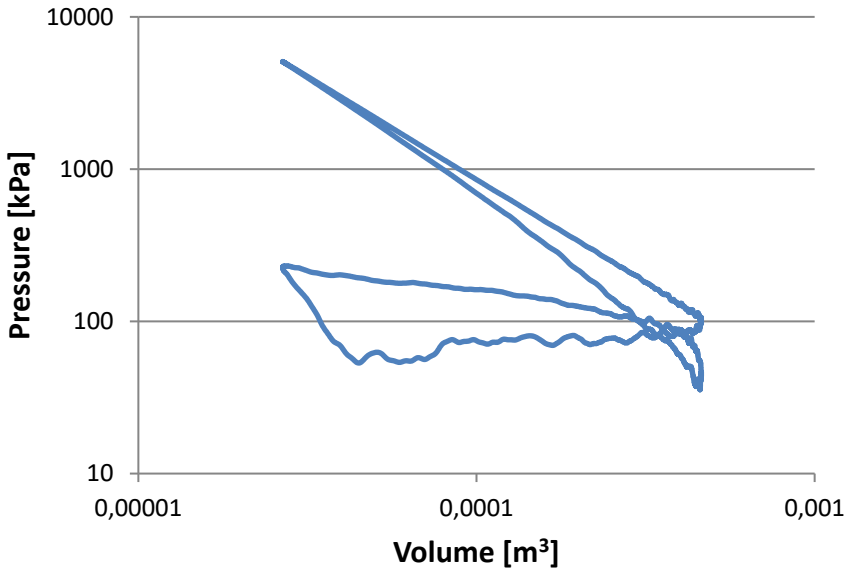

Figure 34: Log P - log V motoring curve at 3200 rpm

The irregular crossover (referred to by Lancaster *et al.* (1975) as the bow-tie effect) which can be observed near BDC is due to the Optrand transducer being susceptible to thermal shock. This thermal shock is also the reason why a slope can be observed in the exhaust stroke in Figure 34 above. Thermal shock, also referred to as temperature drift of a transducer, occurs when the sensor diaphragm is influenced by the cyclic temperature changes within the engine cylinder during the combustion process (Pressure Sensors for Combustion Analysis, 2013). The periodic changes of the sensor diaphragm temperature, exaggerates the influence of cyclic changes in combustion temperature, which in turn leads to inaccurate sensor output readings (Randolph, 1990). Compared to a traditional water-cooled piezoelectric transducer, the Optrand transducer is much more susceptible to

thermal shock, due to the direct exposure of its sensor diaphragm to the combustion pressures (and therefore combustion temperature) (Wlodarczyk, 2012).

9.4 Repeatability of data

After concluding the initial motoring tests and verifying the accuracy of the data, testing at the remainder of the selected indicating test points (test points 1, 4, 9 and 12 from Table 5) were performed. A second test sequence was also performed, during which the entire set of motoring and partial load test points were repeated. This was done in order to verify the repeatability of the entire engine indicating test setup.

Analysis of the measured data showed very good repeatability (see Table 7 below) when comparing the results obtained during the second (repeat) test sequence to that of the first. The pressure data recorded at test point 4 (20 N·m at 2400 rpm) for both test 1 and test 2 are presented in Figure 35 below. Also plotted in Figure 35 are the two motoring curves recorded at 2400 rpm during test 1 and 2 respectively. Inspection of Figure 35 shows that both the motoring and combustion pressure traces exhibit very good repeatability with the pressure traces for tests 1 and 2 being almost identical.

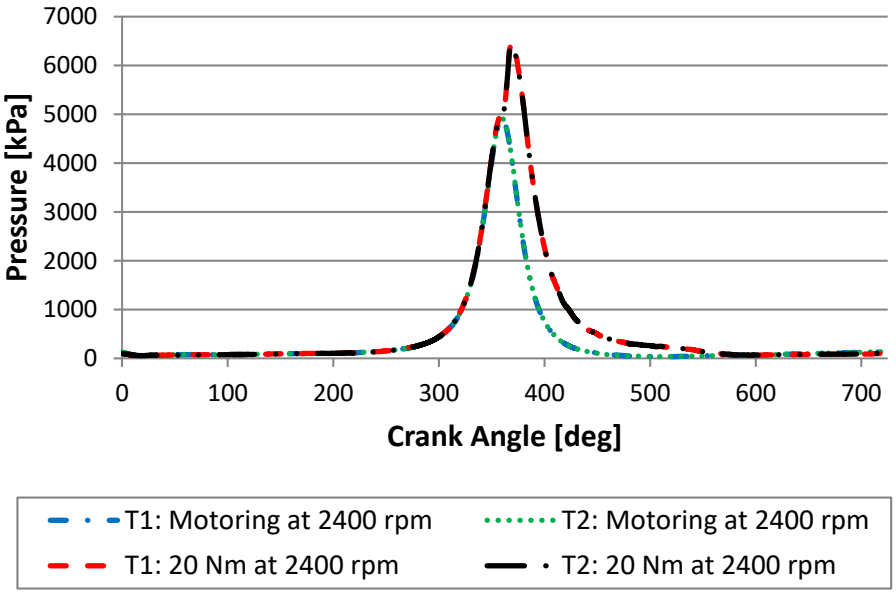

Figure 35: Pressure data repeatability for 2400 rpm

Repeatability was quantified by comparing the maximum pressures (in kPa), the location where the maximum pressure occurs (specified in number of crank angle degrees after TDC), as well as the $IMEP_{gross}$ (also specified in kPa) values

obtained during tests 1 and 2. $IMEP_{gross}$ was calculated by substituting equation (2.3) into equation (2.5) and performing the numerical integration of the measured pressure data from BDC before the compression stroke, to BDC after the expansion stroke. Table 7 below, lists the values of the above mentioned parameters as measured at all of the test points. Also shown in Table 7, is the percentage and degree differences between each of the above parameters when comparing the results obtained during test 2 to that obtained during test 1.

Table 7: Repeatability data of engine indicating tests

Test Point #	Test Point	Max P [kPa]		Diff [%]	Pos of max P after TDC [°]		Diff [°]	$IMEP_{gross}$ [kPa]		Diff [%]
		Test 1	Test 2		Test 1	Test 2		Test 1	Test 2	
1	5 N·m at 2400 rpm	6013	5997	0,3	7,7	7,6	0,1	226,8	228,6	0,8
4	20 N·m at 2400 rpm	6462	6442	0,3	9,0	9,0	0,0	634	635	0,2
9	5 N·m at 3200 rpm	5438	5448	0,2	11,2	11,2	0,0	246,2	254,2	3,2
12	20 N·m at 3200 rpm	6121	6105	0,3	10,3	10,4	0,1	656,7	665	1,3

When observing the percentage differences in maximum pressure obtained between tests 1 and 2, as well as the position where the maximum pressure occurred, it is clear that the data displays very good repeatability. In addition, the last column of Table 7 shows very good repeatability of the calculated $IMEP_{gross}$, with differences as low as 0,2 % being obtained. With the exception of the IMEP result for test point number 9, all other IMEP values are within 1,5 % of each other. Based on the results above, it can be concluded that the repeatability of the entire test setup and engine indicating measurement chain is satisfactory.

9.5 Data accuracy

Apart from verifying the repeatability of both the engine indicating test setup and measurement chain, the accuracy of the measured data was also investigated. This was accomplished by comparing the gross IMEP values (obtained from the

measured in-cylinder pressure data) to the gross IMEP values obtained when using the measured BMEP and adding the FMEP (that is solving equation (2.7)).

The FMEP was calculated using the Willan's Line model. When implementing this model, the fuel consumption of the engine is plotted against BMEP for constant engine speed. This line is then extrapolated until it intersects the negative BMEP axis (where it indicates zero fuel flow). The power output read from where the extrapolated line intersects the BMEP axis can then be regarded as an approximation of the FMEP for the specific engine speed (Van Basshuysen & Schäfer, 2004). Willan's model assumes that when running at constant speed, engine friction is independent of indicated power and, furthermore, that indicated efficiency remains constant. This assumption is, however, only reasonable when running at operating points away from maximum power (Stone, 1992).

Figure 36 illustrates how the process described above was applied to calculate the FMEP at speeds of 2400 rpm and 3200 rpm respectively. In Figure 36, the fuel flow is plotted on the vertical axis (in units of g/s), while BMEP is shown on the horizontal axis (in units of kPa). Fitting a linear curve to the measured data points and extrapolating this curve to where it intersects the BMEP axis, allows the FMEP to be read off for each of the engine speeds. The curve fits for the data of 2400 rpm and 3200 rpm, both indicated R^2 values of 1. A FMEP of 114 kPa was obtained for a test speed of 2400 rpm, while the data recorded at a speed of 3200 rpm indicated a FMEP of 143 kPa. These results agree well with literature, where Van Basshuysen & Schäfer (2004) also reports that the FMEP increases with increasing engine speed.

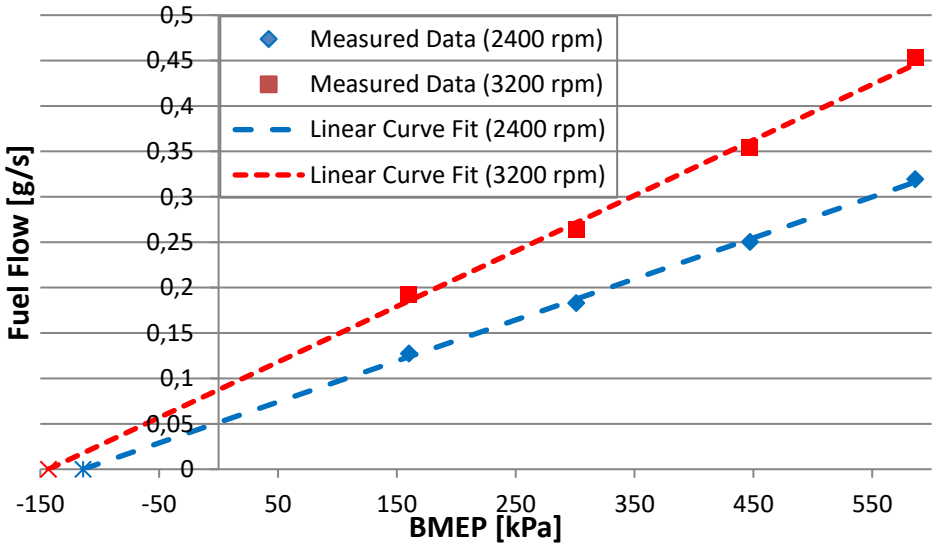

Figure 36: Fuel flow versus BMEP

Equation (2.7) was then solved for the gross IMEP using the FMEP obtained from Figure 36, along with the BMEP measured at the specific load points. The gross IMEP values obtained using the above method, was then compared to the gross IMEP obtained when solving equation (2.5) using the measured in-cylinder pressure data. The percentage differences were calculated using the gross IMEP values obtained from equation (2.5) as baseline. Table 8 below shows the results obtained.

Table 8: Gross IMEP comparison

Test Point	BMEP [kPa]	FMEP [kPa]	$IMEP_{gross}$ (Eq 2.7) [kPa]	$IMEP_{gross}$ (In-cylinder Data) [kPa]	Difference [%]
20 N·m at 2400 rpm	570,3	114,0	684,3	641,7	6,7
20 N·m at 3200 rpm	570,5	143,1	713,6	697,4	2,3

The results show improved correlation between the gross IMEP values for the test conducted at 3200 rpm, indicating a percentage difference of 2,3 % between the measured and calculated gross IMEP values. Results obtained at 2400 rpm show a slightly higher percentage difference (6,7 %) when comparing the measured and calculated gross IMEP values.

The observed discrepancies between the gross IMEP values can be contributed to several reasons. Firstly, the Optrand transducer, used to capture the in-cylinder pressure data, is susceptible to cyclic temperature drift. This was already discovered when plotting the pressure versus volume data (refer to Figure 34). The fact that cyclic temperature drift acts over such a large range of crank angles, means it has a substantial influence on the calculation of the IMEP - which is obtained by integrating over a single engine cycle (Pressure Sensors for Combustion Analysis, 2013). Secondly, in a study performed by Wlodarczyk (2012), the accuracy of the Optrand transducer was compared to that of a 6061 Kistler, water-cooled, piezoelectric pressure transducer. Both sensors were mounted inside the cylinder head and an additional heat shield (in the form of an Inconel 600 wire mesh) was installed in front of the Optrand transducer. Results showed that at pressures above 5 bar, the pressure measured by the Optrand transducer is accurate to within ± 1,5 % of the pressure measured by the piezoelectric pressure transducer. Performing the integration using inaccurate pressure data is thus another source of error in the IMEP calculation. Lastly, using the Willan's line method to calculate the FMEP is limited to the assumptions discussed earlier in this section of the report and the method does therefore not account for the change in friction, due to a change in indicated power.

9.6 Heat release

After verifying the repeatability and accuracy of the measured in-cylinder data, the data was used to setup a heat release model for the test engine. For the purpose of the heat release analysis, the combustion process was modelled using a zero-dimensional, single-zone combustion model. This allows the contents of the cylinder to be modelled as being homogenous, which significantly simplifies the analysis, yet still remains accurate enough to capture the influences that changes in the engine operating parameters have on the rate of heat release (Heywood, 1988).

An Excel spreadsheet was setup based on the work done by Goering (1998), in order to implement equation (2.8) and consequently perform the heat release analysis. Inputs to the spreadsheet included: the test point speed, the fuel flow rate, the ambient test conditions used to calculate the intake air density, as well as the measured in-cylinder pressure data for the specific test point. The flow rate of the intake air was calculated using equation (2.27a) from Heywood (1988). In the absence of more accurate measured data, a volumetric efficiency of 85 % (Heywood, 1988) was assumed during the calculation of the air flow rate. Apart from entering the test conditions, physical properties such as the: bore, stroke, connecting rod length and compression ratio of the engine (as obtained from the engine's data sheet) was also provided as inputs. This spreadsheet was then used to perform accurate phasing and pegging of the measured pressure data and ultimately to calculate the rate of heat release for each test point.

During the heat release analysis, the heat transfer from the cylinder gases to the combustion chamber wall was accounted for, by implementing equation (4.2). After evaluating the various models of the heat transfer coefficient available in the literature, it was decided to implement equation (2.15), as proposed by Hohenberg (1979). The correlation proposed by Eichelberg was not selected due to it not being based on forced convection. The correlation proposed by Hohenberg (1979) was selected over that of Woschni (1967), due to the shortcomings of Woschni's correlation when it comes to predicting heat transfer for high-speed compression-ignition engines (which is the type of engine used in this study). As an added benefit, Hohenberg's correlation is also significantly less complicated to implement compared to that of Woschni. Although, the different correlations discussed above, each leads to a different value of the instantaneous heat transfer coefficient (h), the consequent variation in calculated heat transfer to the cylinder wall, is not that significant. According to Stone (1992), an error of 10 % in the predicted amount of in-cylinder heat transfer, only results in a 1 % error in predicted engine performance.

The accuracy of the heat release model was verified by confirming that the rate of heat release for the motoring pressure data, displayed zero heat release (due to no fuel being added to the engine during the motoring test). The results obtained for the motoring test conducted at a speed of 2400 rpm are presented in Figure 37 below, where the measured data is plotted against crank angle. The measured pressure trace is plotted on the primary vertical axis and the rate of heat release

(ROHR) is shown plotted on the secondary vertical axis. Note that the horizontal axis covers a range from 280 degrees of crankshaft rotation to 520 degrees.

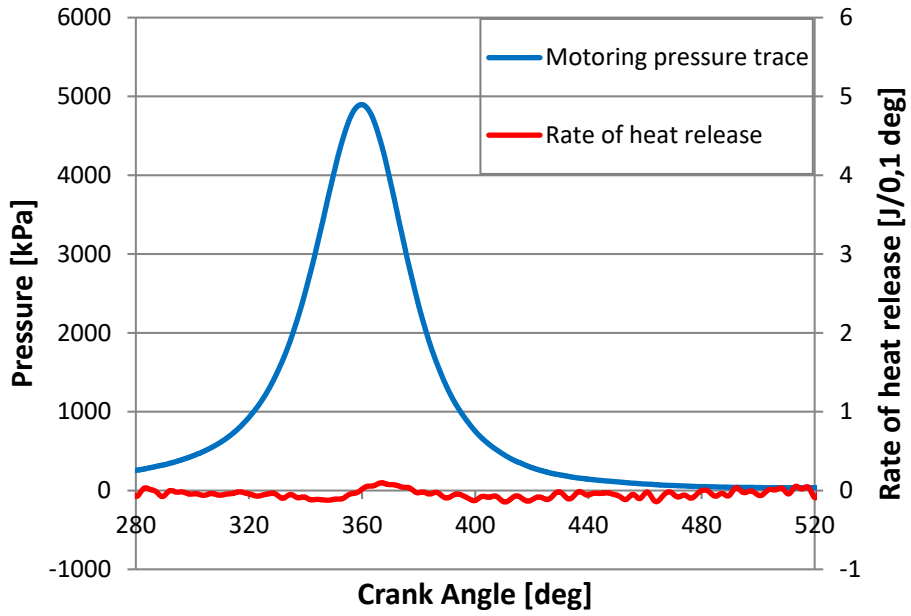

Figure 37: Rate of heat release for motoring at 2400 rpm

After confirming the accuracy of the heat release model, the heat release analysis was completed for all four of the engine indicating test points. Figure 38 displays the obtained ROHR for test point number 4 (20 N·m at 2400 rpm), with the ROHR shown on the primary vertical axis in units of J/0,1 degree. Aside from the ROHR, Figure 38 also displays the cumulative heat release (CHR), which was obtained through numerical integration of the rate of heat release curve. The CHR represents the area enclosed under the ROHR curve for the entire combustion process. The CHR is thus a good approximation (since the analysis is not exact) of the mass of fuel injected (m_f) times the lower heating value (also known as the net calorific value) of the injected fuel. That is,

$$CHR = \int_{\theta_{start}}^{\theta_{end}} Q_{ch} d\theta = m_f Q_{LHV} \tag{9.1}$$

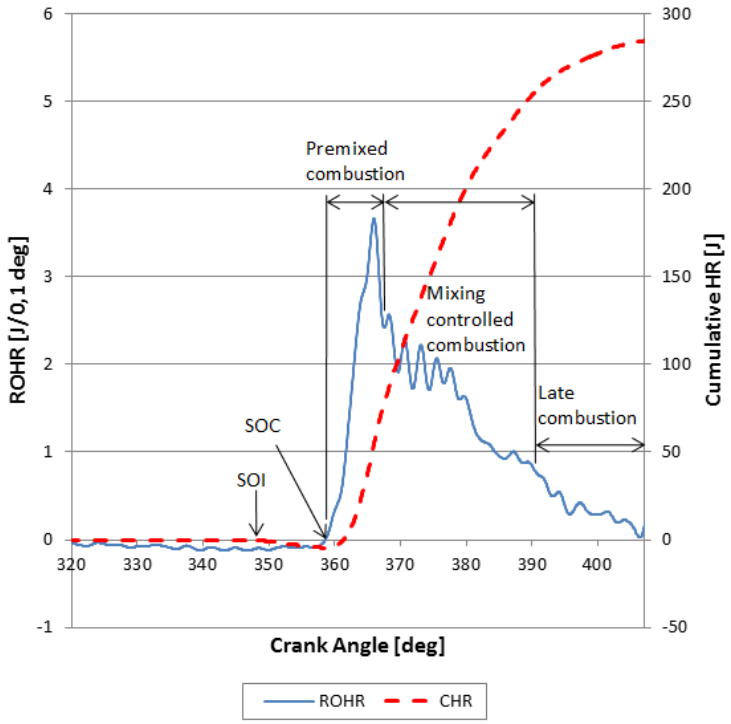

Figure 38: ROHR and CHR (20 N·m at 2400 rpm)

Due to the absence of a needle lift sensor to determine the exact start of injection (SOI), the $\frac{dP}{d\theta}$ curve was used as an indication of the start of injection (see Appendix J). For the data recorded at test point 4, the first peak of the $\frac{dP}{d\theta}$ curve indicated SOI occurring at 348,2 degrees of crank angle rotation. Start of injection results in the CHR curve dipping below zero at SOI (as can be observed in Figure 38 above). This is due to the heat being extracted from the combustion chamber in order to vaporize the injected fuel, resulting in a negative ROHR. Following the SOI event, start of combustion (SOC) occurs at 358,7 degrees, indicating a combustion delay of 10,5 degrees of crank angle rotation. After SOC, the premixed combustion phase commences and lasts for 8,8 degrees up until the 367,5 degree mark. At this point, the mixing controlled combustion phase starts, which lasts until the start of the late combustion phase at 390 degrees. The heat release ends with the conclusion of the late combustion phase at 406 degrees.

10 Conclusion and Recommendations

During this project, a small diesel engine test bench employing an electric dynamometer was developed. The test bench was developed to meet the needs of Stellenbosch University's Biofuel Test Facility, which required an engine testing platform that enables testing of small quantities of biofuel. This requirement originated from the ability of the Department of Process Engineering to produce

their own biofuel, in small quantities at a time. The development of the small test bench further expands the testing capability of the Biofuel Test Facility by enabling further insight to be gained regarding the effects that the use of biofuel has on the performance and emissions of a compression-ignition engine. The valuable information gained using the developed test bench is especially relevant given the implementation of local and global mandates to continue to increase the quantities of biofuel introduced into fuel supplies.

A number of different dynamometer systems were researched and an AC electric dynamometer system, comprising of an AC induction motor, a VSD and a resistor bank was selected as the most appropriate dynamometer system. The electric motor was modified as required and the dynamometer system was then integrated with the existing test bench. A suitable driveshaft was also designed and manufactured to couple the engine to the dynamometer. The test bench was upgraded by installing a fuel flow meter, throttle actuator and various other sensors to measure engine performance. The cylinder head of the test engine was also modified and a fibre-optic pressure transducer was installed to measure in-cylinder pressures. Software was successfully developed to measure and capture both in-cylinder and intake manifold pressures during engine indicating testing.

It was found that the developed test bench, control system and support equipment displayed good control stability and was capable of producing accurate and repeatable results. BSFC and exhaust gas temperature results from different tests showed correlation between the tests to within 1,6 % and 3,2 % respectively. Smoke measurements proved to be very repeatable indicating correlation to within 0,02 FSN (on average) for results obtained during consecutive tests. Engine indicating tests showed that the developed in-cylinder pressure measurement system is capable of providing results at a resolution of 0,1 degrees of crankshaft rotation. Comparing the maximum in-cylinder pressure recorded during consecutive tests, showed that the obtained results were within 0,3 % of each other, while measured IMEP values showed correlation ranging from 0,2 % to 3,2 %. Comparison of measured IMEP values to theoretical calculated IMEP values indicated good accuracy of the engine indicating setup (considering not using a water-cooled transducer) with correlation as good as 2,3 % being achieved between the measured and calculated values.

Even though careful consideration was given to the selection of the test points, for future research it is recommended that the test speed of 2800 rpm be changed to move away from the torque backup region of the engine's performance curve. In terms of future engine indicating testing, it is recommended that a water-cooled piezoelectric pressure transducer be installed into the cylinder head of the engine. This will enable more accurate IMEP measurements to be recorded due to reduced influence of thermal effects on the transducer diaphragm and hence measured pressure. Furthermore, it is also strongly advised that all cabling used for in-cylinder pressure measurement be upgraded to at least category 6 shielded twisted pair cable, in order to reduce the amount of electrical noise present in the measured pressure data.

Finally, in this study the captured pressure data was averaged over 500 engine cycles and a single heat release analysis was performed. The software that was developed to capture the pressure data can, however, be modified to capture any number of cycles. As an alternative approach, heat release analysis can also be performed on each individual engine cycle, after which statistical analysis can then be used to obtain the final heat release results. It is recommended that future researchers also investigate this method of performing the heat release analysis.

Appendix A: Apparent Heat Release

A major advantage of using a heat release approach (based on the first law of thermodynamics) is that the variation in in-cylinder pressure can directly be related to the amount of chemical energy released during the combustion process. Most importantly, the above mentioned is possible while retaining the simplicity of modelling the engine's cylinder contents using a single-zone model (Heywood, 1988).

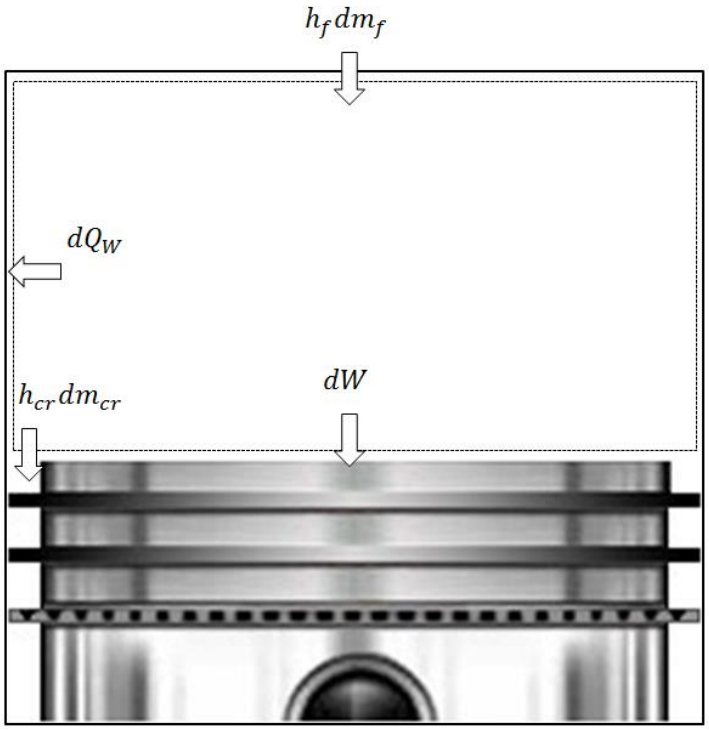

Figure 39: Open system boundary of combustion chamber

(Adapted from: How to Test Engine Compression, [S.a.])

The heat release analysis starts with the first law of thermodynamics applied to an open system. Using the sign convention as indicated in Figure 39, this yields:

$$dQ_{ch} - dQ_w - dW + \sum h_i dm_i = dU_s \qquad \text{(A1)}$$

where the term Q_{ch} is the chemical energy released during combustion, Q_w is the heat transfer to the cylinder wall, dW is the work done on the piston (which equals pdV) and $\sum h_i dm_i$ is the mass flux across the system boundary. Finally, U_s represents the sensible internal energy of the cylinder charge (changes in internal energy due to phase changes and chemical reactions are ignored). Rearranging equation (A1) and substituting pdV for dW, it follows that:

$$dQ_{ch} = dU_s + pdV - \sum h_i dm_i + dQ_w \qquad \text{(A2)}$$

The mass flux term can be expressed as:

$$\sum h_i dm_i = h_f dm_f - h_{cr} dm_{cr} \tag{A3}$$

with h_f being the sensible enthalpy associated with the fuel being injected into the cylinder and h_{cr} the enthalpy associated with the flow into and out of the crevice regions. Assuming ideal gas behaviour (the internal energy is a function of temperature only), the sensible internal energy of the cylinder charge can be expressed as:

$$U_s = mu(T) \tag{A4}$$

with T being the mean temperature of the cylinder charge and m the mass of the cylinder contents within the system boundary (Heywood, 1988). Differentiating equation (A4), gives:

$$dU_s = mdu(T) + u(T)dm \tag{A5}$$

As mentioned previously, the internal energy of an ideal gas is dependent on temperature alone. It therefore follows that the specific heat (c_v) of an ideal gas is also, at most, only a function of temperature. According to equation (4.23) in Boles & Cengel (2007), the differential change in internal energy can then be written as:

$$du = c_v(T)dT \tag{A6}$$

with c_v being the specific heat of air at constant volume.

Substituting equation (A6) into equation (A5) yields:

$$dU_s = mc_v(T)dT + u(T)\, dm \tag{A7}$$

Substituting equations (A3) and (A7) into equation (A2) yields:

$$dQ_{ch} = mc_v(T)dT + u(T)\, dm + pdV - (h_f dm_f - h_{cr} dm_{cr}) + dQ_w \tag{A8}$$

Neglecting the quantity of fuel that is injected into the cylinder ($h_f \sim 0$), dm is caused by flow into and out of the crevice regions (that is $dm = -dm_{cr}$) (Heywood, 1988). Equation (A8) then becomes:

$$\frac{dQ_{ch}}{d\theta} = \frac{mc_v(T)dT}{d\theta} + \frac{pdV}{d\theta} + (h_{cr} - u(T))\frac{dm_{cr}}{d\theta} + \frac{dQ_w}{d\theta} \tag{A9}$$

where all the terms have been expressed with respect to the crank angle (θ). Using the ideal gas law:

$$PV = mRT \tag{A10}$$

For a constant value of R (the universal gas constant) it follows that:

$$dT = \frac{VdP}{mR} + \frac{PdV}{mR} - \frac{PVdm}{m^2R} \tag{A11}$$

$$= \frac{VdP}{mR}\left(\frac{P}{P}\right) + \frac{PdV}{mR}\left(\frac{V}{V}\right) - \frac{PVdm}{m^2R} \tag{A12}$$

$$= \frac{TdP}{P} + \frac{TdV}{V} - \frac{Tdm}{m} \tag{A13}$$

Substituting equation (A13) into equation (A9) it follows that:

$$\frac{dQ_{ch}}{d\theta} = \frac{mc_v(T)}{d\theta}\left(\frac{TdP}{P} + \frac{TdV}{V} - \frac{Tdm}{m}\right) + \frac{pdV}{d\theta} + (h_{cr} - u(T))\frac{dm_{cr}}{d\theta} + \frac{dQ_w}{d\theta} \tag{A14}$$

Using equation (A10) to eliminate m from equation (A14) leads to:

$$\frac{dQ_{ch}}{d\theta} = \frac{PV}{RT}c_v(T)\frac{TdP}{Pd\theta} + c_v(T)\frac{PV}{RT}\frac{TdV}{Vd\theta} - c_v(T)\frac{Tdm}{d\theta}$$

$$+ \frac{pdV}{d\theta} + \left(h_{cr} - u(T)\right)\frac{dm_{cr}}{d\theta} + \frac{dQ_w}{d\theta} \tag{A15}$$

$$= \frac{c_v(T)}{R}\left(\frac{VdP}{d\theta}\right) + \left(1 + \frac{c_v(T)}{R}\right)\left(\frac{PdV}{d\theta}\right) - c_v(T)\frac{Tdm}{d\theta}$$

$$+\left(h_{cr} - u(T)\right)\frac{dm_{cr}}{d\theta} + \frac{dQ_w}{d\theta} \tag{A16}$$

The specific heat ratio (γ) is defined as:

$$\gamma = \frac{c_p(T)}{c_v(T)} \tag{A17}$$

With c_p and c_v being the specific heats at constant pressure and constant volume, respectively. For an ideal gas, the relationship between c_p and c_v is given by equation (4-29) in Boles & Cengel (2007) as:

$$c_p(T) = c_v(T) + R \tag{A18}$$

Substituting equations (A17) and (A18) into equation (A16), as well as utilizing the fact that $dm = -dm_{cr}$, yields:

$$\frac{dQ_{ch}}{d\theta} = \left(\frac{1}{\gamma-1}\right)V\frac{dP}{d\theta} + \left(\frac{\gamma}{\gamma-1}\right)P\frac{dV}{d\theta}$$

$$+[h_{cr} - u(T) + c_v(T)]\frac{dm_{cr}}{d\theta} + \frac{dQ_w}{d\theta} \tag{A19}$$

From equation (A19) it is clear that when crevice flow is neglected, the heat released during combustion can be calculated from knowledge of the changes in: the in-cylinder volume, the in-cylinder pressure and the heat transferred to the cylinder wall. Neglecting crevice flow yields the apparent heat release rate:

$$\frac{dQ_{ch}}{d\theta} = \left(\frac{1}{\gamma-1}\right)V\frac{dP}{d\theta} + \left(\frac{\gamma}{\gamma-1}\right)P\frac{dV}{d\theta} + \frac{dQ_w}{d\theta} \tag{A20}$$

which is equation (2.8) in Section 2.7.4.2.

Appendix B: Evaluation of Dynamometer Systems

Four different dynamometer systems were considered, each of which are discussed in detail in the sections to follow.

B.1 Hydraulic dynamometer system

Even though it was already determined that the Froude hydraulic dynamometer, that the test bench employed previously, would not be able to meet the needs of this project, a modern hydraulic dynamometer system was still considered as an option for the upgraded test bench. The technology employed to control modern day hydraulic dynamometers is far advanced when compared to the hand operated Froude dynamometer. Therefore, the use of a hydraulic dynamometer system was still considered an effective means of applying load to the test engine.

B.1.1 Suitability of dynamometer system

When it comes to measuring power with a dynamometer, it is the torque measurement that governs the accuracy of the system (speed can generally be measured to any desired accuracy) (Killedar, 2012). Considering the performance requirements stipulated in Table 1, it is clear that such a high level of accuracy will prove difficult to achieve with just a basic hydraulic dynamometer setup. The reason for this is that the load applied by a hydraulic dynamometer is largely dependent on the pressure of the supply water to the dynamometer being constant. Any fluctuation in the supply pressure of the water will cause a disturbance in the load applied to the engine. Therefore, in order to achieve the best possible control, when using a hydraulic dynamometer, the pressure of the supply water must be regulated. This is done using either a pressure regulator or by installing a header tank in the supply water line. Optimum control also requires that the dynamometer be fitted with a butterfly valve (on the outlet side of the dynamometer) which is controlled using a closed-loop electrohydraulic servo system, or alternatively by a DC electric servo motor (Killedar, 2012). This valve controls the load applied by the dynamometer, by regulating both the amount of water within the dynamometer casing and by varying the rate at which water flows through the dynamometer. The response of this valve thus has a major effect on the load control response of the entire dynamometer (Killedar, 2012).

A downside to installing a hydraulic dynamometer on the small test bench is that water is always present in the casing of the dynamometer. This means that the dynamometer is constantly exerting some drag force on the test engine. Even though this drag force is small, in terms of the overall output of the small test engine, it is considered substantial enough to have an effect on the test results. Furthermore, the hydraulic dynamometer also has no starting or motoring capability. The use of a hydraulic dynamometer thus limits the testing capability of the entire test setup in that it does not allow the motoring torque (and hence the friction losses associated with a particular test engine) to be measured.

B.1.2 Integration

Trunnion mounting the hydraulic dynamometer to a test stand requires the design and fabrication of pedestals (to house the trunnion bearings) which can be used to support the dynamometer. These pedestals have to be line bored to ensure that the bearings are concentric and hence that the dynamometer shaft runs true. Although an adequate water supply is available in the test facility, the test engine does not require any cooling water (the single-cylinder engine is air-cooled). Water supply and return lines will therefore have to be installed specifically for the hydraulic dynamometer.

In order to achieve the best possible control, additional equipment will also have to be installed to ensure that water is supplied to the dynamometer at constant pressure (although there is an adequate water supply available in the test facility, no hardware is in place to regulate the water pressure). This might prove difficult, as there is limited space available in the test cell where the engine test stand is to be installed. Provision will also have to be made for the mounting of a load cell and attachment of this load cell to the dynamometer in order to measure the torque absorbed by the dynamometer.

B.1.3 Cost

When it comes to purchasing a new dynamometer system, a hydraulic dynamometer is typically the most cost effective solution. The fact that this dynamometer can be set up using a relatively simple control system, is the main reason why it is so cost effective. When increased accuracy and control capability is required, cost will rise due to the requirement of additional equipment. In terms of overall operating cost, hydraulic dynamometers are very cost effective, with the only electrical power consumption being the small amount of electricity that is consumed by the dynamometer's control system (Killedar, 2012). Water is only circulated through the dynamometer, so the only cost involved here is the cost of supplying the water at constant pressure to the dynamometer.

Minimal maintenance is required throughout the dynamometer's life cycle as scale formation in the water and stator pockets occurs very slowly over time (Killedar, 2012). Being a trunnion-mounted machine, the trunnion bearings can be prone to brinelling. This problem can, however, be addressed by periodically rotating the trunnion bearings to prevent localised brinelling of the trunnion bearings (Martyr & Plint, 2007).

B.1.4 Operational lifetime and flexibility (future research)

Hydraulic dynamometers have an extremely long operational lifetime. Provided the small amount of maintenance (as mentioned above) is performed, the dynamometer can remain operational for years. The flexibility of the dynamometer system is, however, quite limited in terms of the types of engine testing for which it can be employed. If in the future, the need might exist to perform any sort of transient testing or if the need to be able to motor the test

engine becomes essential, the hydraulic dynamometer system will become obsolete and a new system will have to be installed to satisfy the testing requirements.

B.2 Dry gap eddy current dynamometer system

When it came to the eddy-current dynamometers, the wet gap machine was not considered, due to its inherent high inertia, high level of minimum torque and liability to corrosion if left static for longer periods of time (Martyr & Plint, 2007). The last mentioned point is of particular importance given the infrequent nature of the engine testing conducted at Stellenbosch University's Biofuel Test Facility. Consequently, the following section details the evaluation of the dry gap eddy-current dynamometer.

B.2.1 Suitability of dynamometer system

Although the dry gap eddy-current dynamometer also requires a water supply, unlike the hydraulic dynamometer, the torque and speed control of the eddy-current dynamometer is not affected by any fluctuation in the water pressure. This then eliminates the need for additional hardware to control the water supply pressure. In addition, since water only flows between the loss plates of the dynamometer and is never in contact with the machine's rotor, the eddy-current dynamometer has less drag and thus a lower level of minimum torque compared to the hydraulic dynamometer. This is particularly beneficial considering that the test engines will primarily be small capacity engines with low torque output.

Similar to the hydraulic dynamometer, the eddy-current machine also does not have the ability to motor or start the test engine. This shortcoming can, however, be overcome by installing an additional electric motor behind the dynamometer as part of the drive train. This electric motor then enables the operator to motor the engine when the dynamometer is not absorbing power. However, the addition of such a motor to the system does bring about its own challenges. Firstly, in terms of mechanical design (both the dynamometer and the motor has to be coupled to the engine utilizing two concentric driveshafts, the one running inside the other). Secondly, a more sophisticated control system is required, that makes provision for the control of the additional electric motor.

B.2.2 Integration

Trunnion mounting an eddy-current dynamometer has similar requirements to that of trunnion mounting a hydraulic dynamometer. However, compared to a hydraulic dynamometer of similar capacity, the eddy-current dynamometer is typically a heavier machine (Killedar, 2012). This might complicate the mounting of the dynamometer, although supporting the mass of the dynamometer is in general not a large concern in engine test setups as the test bench can easily be designed to accommodate the additional mass. Although the dynamometer does not require a constant supply water pressure to obtain good torque control, it is

crucial that an adequate water flow rate is maintained through the dynamometer during operation. A drop in the water flow rate will cause the loss plates to overheat and distort. In the event that these plates do distort, the air gap between the rotor and the loss plates will close up, leading to catastrophic failure of the dynamometer when the rotor comes into contact with the cooling plates (Martyr & Plint, 2007) (Killedar, 2012). If the eddy-current machine is selected, flow switches will have to be fitted to the dynamometer to ensure that a suitable water flow rate is maintained. Pressure switches alone will not suffice, as it is possible to have pressure in a closed system without having any flow of water (Martyr & Plint, 2007).

B.2.3 Cost

When it comes to the initial capital layout, the eddy-current dynamometer is slightly more expensive than an equivalent sized hydraulic dynamometer. Furthermore, since the eddy-current machine achieves load control through varying the current supplied to the field coils inside the dynamometer, it has higher electrical power consumption than a hydraulic dynamometer. This in turn, contributes to it having higher operating cost compared to a hydraulic dynamometer (Killedar, 2012).

The maintenance requirements for the eddy-current dynamometer are very similar to those of the hydraulic dynamometer. The fact that the eddy-current dynamometer also utilises a trunnion-mounted arrangement, similar to that of the hydraulic dynamometer, means that it is susceptible to similar complications in terms of brinneling of its trunnion bearings. The eddy-current dynamometer also requires that maintenance be performed on a more regular basis compared to a hydraulic dynamometer. This is due to scale formation occurring more rapidly in the loss plates of the eddy-current machine, then it does inside a hydraulic dynamometer (Killedar, 2012).

B.2.4 Operational lifetime and flexibility (future research)

As long as the required maintenance is performed and an adequate water flow rate is maintained through the dynamometer during testing (thus ensuring that the outlet water temperatures do not rise above the specified operating limits), eddy-current machines are very reliable and continue to perform satisfactory for years on end. However, if the dynamometer is not maintained properly and clogging of the water channels inside the loss plates occur, a substantial reduction in the power absorption capability of the dynamometer will be noticed.

Eddy-current dynamometers are limited to steady state testing and are not used to perform transient testing. Due to the load applied by these dynamometers only being a function of the amount of current that is supplied to field coils they are, however, capable of performing rapid load changes. They also have the capability of developing a substantial amount of braking torque at low operating speeds, which can be useful for future research projects (Martyr & Plint, 2007). Similar

to a hydraulic dynamometer, the eddy-current machine's biggest limitation is, however, still the fact that it lacks the ability to motor the test engine.

B.3 DC dynamometer system

Apart from the passive dynamometer systems discussed up until this point, active dynamometer systems were also considered. The first of which was the DC dynamometer system.

B.3.1 Suitability of dynamometer system

One of the most attractive features of these dynamometer systems is the fact that DC dynamometers are available in air-cooled versions (Killedar, 2012). The fact that the engines that will be tested on the particular test bench are also all air-cooled, makes the implementation of an air-cooled dynamometer system very attractive. If a DC dynamometer is selected, the requirement of coolant supply and return lines running to and from the test bench is thus eliminated. This not only reduces the amount of hardware to be installed, but also reduces the risk of any potential damage to electronic components due to accidental leakage of fluid in the test cell environment. A dynamometer that is not dependent on any cooling water, also lends itself to more accurate torque measurement, due to there being less external influences (such as fluid motion in the coolant lines that connect directly to the dynamometer casing) that can affect the measurement values. The absence of any fluid flowing to or from the dynamometer, therefore allows one to obtain more accurate and repeatable torque measurement results.

A further advantage of selecting a DC dynamometer is that apart from just being able to absorb the power generated by the test engine, the dynamometer will also be capable of driving the engine being tested. That is, unlike the dynamometers discussed previously, DC dynamometers have the ability to motor the test engine and can therefore be used to measure the frictional torque of the particular test engine (Salam Z, 2003) (Stone (1992). If the dynamometer is selected such that it is capable of developing enough start-up torque to be able to crank the test engine, then the dynamometer can be used to start the engine directly. This then eliminates the need for the presence of a starter motor on the engine.

Disadvantages of selecting a DC dynamometer system are that these systems tend to have high inertia, as well as limited maximum operating speed, when it comes to engine testing. The high inertia of these systems limits the transient response of the entire dynamometer setup and may lead to problems with torsional vibration (which is already a concern for the single-cylinder, compression-ignition engine) (Martyr & Plint, 2007).

B.3.2 Integration

When it comes to integrating the DC dynamometer with the existing test setup, the DC dynamometer allows for several mounting options. The simplest mounting arrangement, requiring the least amount of mechanical modification,

will be to use a foot-mounted DC electric motor and to mount it directly to the existing test bed (Killedar, 2012). Seeing that the dynamometer will be fixed to the test bed, proper alignment of the engine and dynamometer will be crucial during installation. If the DC dynamometer is mounted directly to the test bed, an inline torque transducer, such as a torque flange, will have to be employed to measure the torque output of the engine. Financially this might not be a viable solution, seeing that these transducers are quite expensive.

An alternative method of power measurement offered by a DC dynamometer is to calculate the power absorbed by the dynamometer (which operates as a generator when absorbing the power developed by the test engine) by measuring the voltage and current that the dynamometer outputs when absorbing power. However, when measuring the electrical parameters, the efficiency of the dynamometer at all of its operating speeds needs to be known in order to obtain an accurate indication of the power absorbed (Stone 1992). As the efficiency of the dynamometer is generally not known at all of its operating speeds, this method of power measurement is less accurate compared to when a load cell or inline torque transducer is used. The option is of course still available to trunnion mount the DC dynamometer and to measure the torque using a load cell - exactly like in the case of a hydraulic or eddy-current dynamometer. It should, however, be verified beforehand that the physical construction of the proposed electric motor allows for the required modifications to be made that will enable it to be trunnion-mounted.

Installing a DC dynamometer will furthermore also require the installation of additional hardware that is not required when using either a hydraulic or eddy-current dynamometer. This includes items such as the drive unit (used to control the dynamometer) that will need to be installed in a suitable enclosure. The enclosures that house these drive units can be quite large (especially for drive units with high power ratings) and mounting space can be difficult to accommodate in the engine test cell environment. Typically, these units have to be mounted outside of the test cell for noise and temperature reasons, but also as close as possible to the dynamometer in order to reduce the cost of cabling to the dynamometer (Martyr & Plint, 2007). In addition to the drive unit, other hardware such as a system to feed the generated power back to the electrical grid, or a load bank to dissipate the power generated in the form of heat, also needs to be installed.

B.3.3 Cost

In terms of initial capital layout, DC electric motors are quite expensive and really only economical at low (< 3,7 kW) and high (> 75 kW) power ratings (Killedar, 2012). As mentioned previously, when using a DC dynamometer operating in regeneration mode, the option is available to feed the electrical power generated back to the mains supply (in an effort to generate some revenue using the dynamometer system). This is, however, not an economic solution for the proposed small test engine setup. The developed test bench will primarily be used

to conduct fuel-to-fuel evaluations using small capacity engines consequently power will be generated infrequently and in small quantities at a time. The additional hardware (as mentioned in the previous section) that also requires installation will necessarily drive up the initial installation cost of the dynamometer system.

Operating a DC dynamometer will also require some periodic maintenance to be performed on the brushes and commutator that form part of the construction of the DC electric motor. As these components wear during normal operation of the dynamometer, their condition will have to be monitored so that they can be replaced when needed (Killedar, 2012).

B.3.4 Operational lifetime and flexibility (future research)

Apart from the brushes of the DC dynamometer that require periodic replacement, the DC dynamometer system is very robust and has a very long lifetime. In situations where the DC electric motor is trunnion-mounted, the pedestal bearings will need to be rotated from time to time in order to avoid localised brinelling of the bearings. This is, however, a general requirement for any trunnion-mounted dynamometer setup.

The DC dynamometer system is very flexible when it comes to satisfying possible future research needs, provided that, the power and speed rating of the test engine does not exceed that of the dynamometer. Unlike the previous dynamometers that were considered, due to its motoring capability, the DC dynamometer can also be used to perform transient testing (Atkins, 2009). This can considerably expand the future testing capability of the entire test setup.

B.4 AC dynamometer system

The second active dynamometer system considered was the alternating current (AC) dynamometer system.

B.4.1 Suitability of dynamometer system

Apart from the fact that an AC dynamometer operates on AC current and has an AC power supply, the dynamometer itself is very similar to the DC dynamometer considered in the previous section. Just like the DC dynamometer, an AC dynamometer is also air-cooled and does not require any cooling water (Killedar, 2012). Consequently, an AC dynamometer offers the same benefits that are associated with not having any cooling lines running to and from the dynamometer as was discussed for the DC dynamometer in the previous section.

As was previously mentioned, AC dynamometers also have the ability to motor and start the test engine. Therefore, as is the case with the DC dynamometer, the AC dynamometer can be used to measure the friction loss associated with a particular test engine while the engine is being driven by the dynamometer. It

should, however, be noted that AC dynamometers are also limited when it comes to their maximum operating speed.

B.4.2 Integration

Except for AC dynamometers weighing less compared to a DC dynamometer of the same power rating, there is no significant advantage in using an AC dynamometer over a DC dynamometer when it comes to physically mounting the dynamometer to the test stand (Killedar, 2012). All of the mounting and torque measurements options that are available for a DC dynamometer are also available for an AC dynamometer. Similar to a DC dynamometer system, an AC dynamometer system also requires extra space in the test facility to mount its drive unit and other additional hardware. In other words, in terms of mounting either a DC or an AC dynamometer, there is no real advantage in choosing one above the other.

B.4.3 Cost

Although the drive units for AC dynamometers tend to be slightly more expensive than for DC dynamometers, the AC motor itself is far cheaper than an equivalent sized DC motor. Furthermore, an AC dynamometer requires virtually no maintenance, while the brushes and commutator of a DC machine do require periodic replacement (Killedar, 2012). Therefore, in terms of maintenance cost, the AC machine is by far the preferred solution. The initial installation cost associated with the additional hardware requirements of an AC dynamometer is very much the same as for a DC dynamometer system.

B.4.4 Operational lifetime and flexibility (future research)

The design of the AC electric motor renders it essentially maintenance free. This makes the AC dynamometer even more robust than a DC dynamometer and consequently very reliable over its entire operational lifetime. The lower inertia of the AC dynamometer means that it is capable of faster load changes, which translates into it offering improved transient testing capability over the DC dynamometer. This makes the AC dynamometer more suitable for testing smaller capacity engines and allows for even more flexibility in terms of the future research projects that can be accommodated. Finally, the lower inertia of the AC motor is also beneficial in terms of not contributing towards torsional vibration, which is always a concern when testing single-cylinder engines.

Appendix C: Flexible Coupling Selection

The selection of an appropriately sized flexible coupling was performed by following the guidelines stipulated in the Fenaflex flexible tyre coupling catalogue from Fenner (Drive Design and Maintenance Manual, [S.a.]).

The first step in selecting the coupling was to identify a coupling capable of safely transmitting the required amount of shaft power at the applicable speed where the test engine outputs its maximum power. From Table 16 it can be seen that the maximum power output of the test engine is 7,4 kW at a speed of 3600 rpm. Furthermore, the operating conditions of the flexible coupling were also accounted for by applying a service factor to the maximum power developed by the engine. Multiplying the maximum power output of the engine with the selected service factor gives the design power, which was ultimately used to select the appropriate size coupling.

For the test setup configuration consisting of an internal combustion engine driving a dynamometer with a duty cycle of less than 10 hours per day, the table on page 113 of the flexible coupling catalogue indicates a service factor (S_F) of 1,3 (Drive Design and Maintenance Manual, [S.a.]). Applying the service factor to the maximum power output of the engine results in a design power of:

$$Design\ power = P_{E,max} \times S_F \quad \text{(C1)}$$

$$= 7{,}4 \times 1{,}3 \quad \text{(C2)}$$

$$= 9{,}62\ kW \quad \text{(C3)}$$

The power ratings table on page 114 of the flexible coupling catalogue shows that the first coupling capable of transmitting this amount of power at a speed of 3600 rpm is a F50 size coupling. The specifications of which are presented in Table 9 below.

Table 9: Fenaflex F50 flexible tyre coupling specifications

Specification	Unit	F50 Coupling
Nominal torque rating ($T_{F,nom}$)	N·m	66
Maximum torque rating ($T_{F,max}$)	N·m	160
Maximum speed rating	rpm	4500
Maximum parallel misalignment	mm	1,3
Maximum end float	mm	± 1,7
Maximum angular misalignment	°	4

(Source: Drive Design and Maintenance Manual, [S.a.])

Given the flexible coupling's nominal torque rating of 66 N·m, the factor of safety guarding against failure of the flexible coupling during normal operation is therefore:

$$n_{fc} = \frac{T_{F,nom}}{T_{E,max}} \quad \text{(C4)}$$

$$= \frac{66}{27,5} \quad \text{(C5)}$$

$$= 2,4 \quad \text{(C6)}$$

In addition to its continuous torque rating of 66 N·m, the flexible coupling also has a maximum torque rating of 160 N·m. As stipulated by the Drive Design and Maintenance Manual ([S.a.]), this rating is to be regarded as the short term overload rating of the particular flexible coupling. The maximum torque rating enables the coupling to cope with sudden spikes in the transmitted torque, which might occur due to torque pulsations from the engine, or due to a sudden torque reversal (for example when the engine comes to rest during shutdown) (Martyr & Plint, 2007).

These sudden spikes in the transmitted torque can be accounted for by applying service factors (for the applicable engine-dynamometer configuration) to the maximum torque output of the engine. This allows the design torque to be calculated using equation (C7) below:

$$T_{design} = T_{E,max}\ (K_1 + K_2) \quad \text{(C7)}$$

where T_{design} is the design torque and $T_{E,max}$ is the maximum nominal torque output of the test engine (obtained from Table 16). K_1 and K_2 are the service factors to account for the driving and driven machine, respectfully. For a single-cylinder, compression-ignition engine driving a generator, Cabris (Pty) Ltd. (1992) indicates values of 3 and 1,5 for K_1 and K_2 respectfully. Substituting the aforementioned values into equation (C7), leads to a design torque of:

$$T_{design} = 27,5\ (3 + 1,5) \quad \text{(C8)}$$

$$= 123,8\ Nm \quad \text{(C9)}$$

At this point it is worth noting that the majority of the engine tests will be conducted at partial load and that it is only during full load tests that the flexible coupling will have to transmit the maximum torque output of the engine. The factor of safety guarding against failure of the flexible coupling during torque spikes is therefore:

$$n_{ts} = \frac{T_{F,max}}{T_{design}} \quad \text{(C10)}$$

$$= \frac{160}{123,8} \quad \text{(C11)}$$

$$= 1,3 \quad \text{(C12)}$$

This result was considered acceptable, given the fact that it is on top of the already applied service factor of 4,5 and that it is only during full load tests and for only very short periods of time that the flexible coupling is likely to experience such high levels of torque.

Appendix D: Driveshaft Analysis

Once a suitable coupling was selected, the next step was to verify that the driveshaft itself would be capable of transmitting the required amount of torque after the proposed design changes to the driveshaft were implemented.

D.1 Driveshaft layout

The assembly drawing of the driveshaft components is shown in Figure 40. Moving from left to right in Figure 40, torque is transmitted from the engine to the driveshaft (component 1 in Figure 40), via the engine flange and constant velocity joint assembly (component 2). The driveshaft then transmits the torque to the dynamometer flange assembly (component 3) via the taper lock (component 9) and flexible coupling components (components number 4 and 5). The second flange of the flexible coupling has been bolted to the dynamometer flange to form the dynamometer flange assembly. Not shown in Figure 40 is the keyway which has been machined into the driveshaft (at point B) to aid in transmitting the torque between the driveshaft and the taper lock (component 9).

On the dynamometer side (at point D), the shaft is supported in a spherical bearing which was secured in the dynamometer flange using a slight press fit. The function of this bearing is to locate the shaft, as well as to accommodate angular misalignment of the shaft. This end of the driveshaft does not transmit any torque.

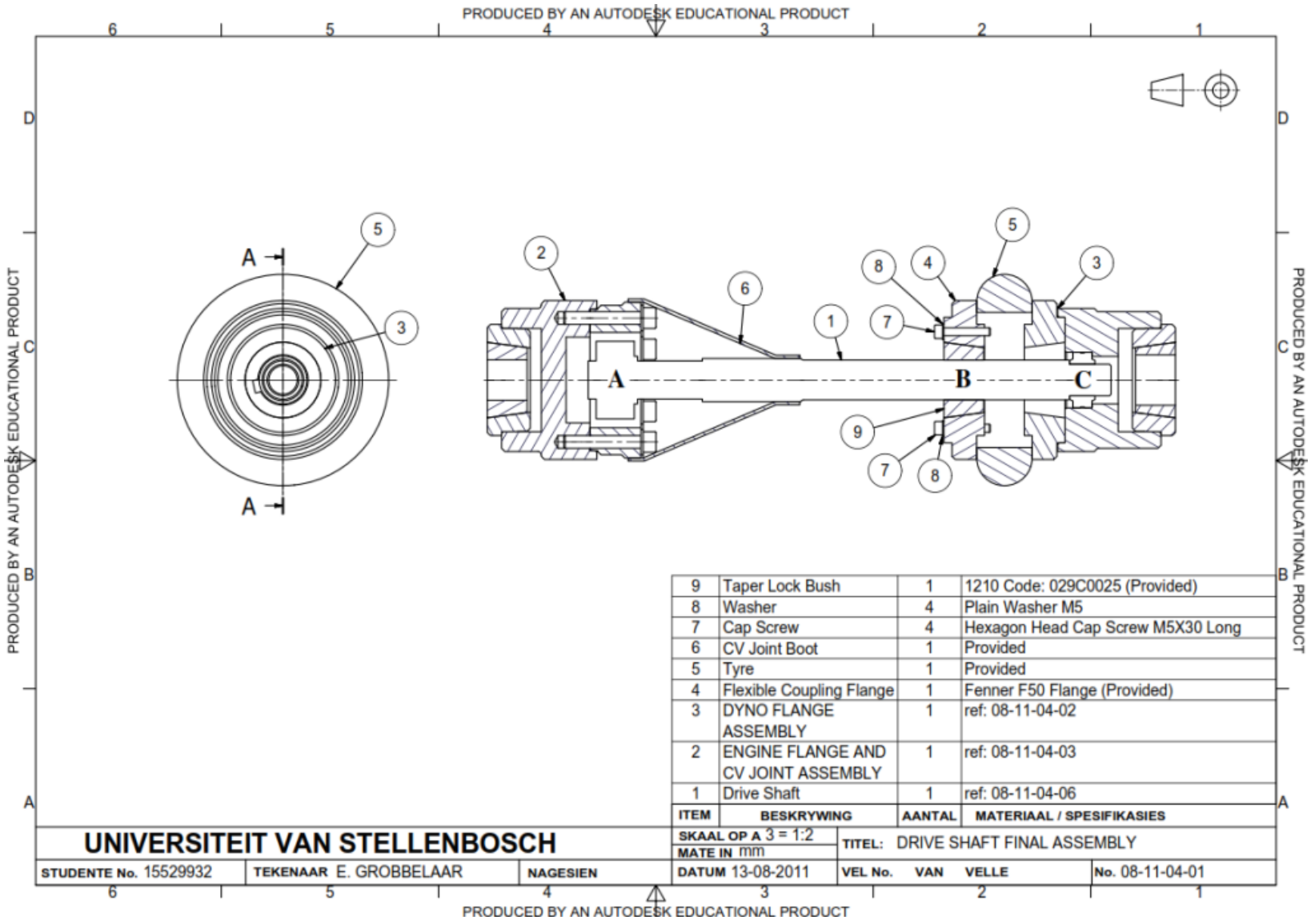

ITEM	BESKRYWING	AANTAL	MATERIAAL / SPESIFIKASIES
9	Taper Lock Bush	1	1210 Code: 029C0025 (Provided)
8	Washer	4	Plain Washer M5
7	Cap Screw	4	Hexagon Head Cap Screw M5X30 Long
6	CV Joint Boot	1	Provided
5	Tyre	1	Provided
4	Flexible Coupling Flange	1	Fenner F50 Flange (Provided)
3	DYNO FLANGE ASSEMBLY	1	ref: 08-11-04-02
2	ENGINE FLANGE AND CV JOINT ASSEMBLY	1	ref: 08-11-04-03
1	Drive Shaft	1	ref: 08-11-04-06

UNIVERSITEIT VAN STELLENBOSCH

SKAAL OP A 3 = 1:2
MATE IN mm
TITEL: DRIVE SHAFT FINAL ASSEMBLY

STUDENTE No. 15529932 | TEKENAAR E. GROBBELAAR | NAGESIEN | DATUM 13-08-2011 | VEL No. VAN VELLE | No. 08-11-04-01

Figure 40: Driveshaft assembly drawing

D.2 Driveshaft material

Due to the driveshaft being a repurposed half shaft of a vehicle powertrain, the exact material properties of the shaft was unknown. However, various literature sources indicated that a commonly used material for such shafts is AISI 4140 steel (AISI 4140 Chrome-Molybdenum High Tensile Steel, 2012) (High Strength Bars, [S.a.]) (4140 High Tensile, [S.a.]). The properties of 4140 steel differ significantly depending on the type of heat treatment applied to the material. Literature shows the yield strength varying from 415 MPa to 1735 MPa and the ultimate tensile strength ranging from 655 MPa to 1965 MPa (AISI 4140 Search Results, [S.a.]). The modulus of elasticity and poisson's ratio for all these material are the same though.

Following a conservative approach, the driveshaft material was assumed to be AISI 4140 steel, annealed at 815 °C, furnace cooled at 11 °C/hour to 665 °C and then air cooled. According to the literature, this produces 4140 steel with the lowest yield and ultimate tensile strength values (AISI 4140 Steel, Annealed at 815 °C, [S.a.]). The exact material properties used during all analysis of the driveshaft are presented in Table 10 below.

Table 10: Material properties for AISI 4140 steel in annealed condition

Property	Symbol	Unit	Value
Ultimate tensile strength	S_{ult}	MPa	655
Yield strength	S_y	MPa	415
Modulus of elasticity	E	GPa	205
Poisson's ratio	ν	-	0,29
Density	ρ	kg/m^3	7850

(Source of data: AISI 4140 Steel, annealed at 815°C, [S.a.])

D.3 Driveshaft loads

With reference to Figure 40 above: the driveshaft was modelled as having a roller support at point A (the constant velocity joint allows rotation, as well as a small amount of axial displacement of the shaft). Point C was also modelled as a roller support, but in addition the spherical bearing also constrains the shaft from moving to the right (in the direction of the dynamometer) in the axial direction. Axial movement of the shaft towards the engine is constrained by the flexible coupling.

Figure 41 below shows the free body diagram of the driveshaft, which was used to analyse the stresses in the shaft. The force (F_G) represents the mass of the shaft applied as a single force at the centre of the shaft. Note that the gravitational acceleration (g) is equal to 9,796 m/s^2 at the test cell location.

$$F_G = m_s g \tag{D1}$$

$$= 1{,}52 \times 9{,}796 \tag{D2}$$

$$= 14{,}88\ N \tag{D3}$$

The force F_{By} represents the mass of the taper lock, left flange of the flexible coupling and half the mass of the tyre coupling (the remainder of the flexible coupling's mass, as well as the mass of the dynamometer flange is regarded as being supported by the dynamometer's shaft).

$$F_{By} = m_B g \tag{D4}$$

$$= 1{,}55 \times 9{,}796 \tag{D5}$$

$$= 15{,}18\ N \tag{D6}$$

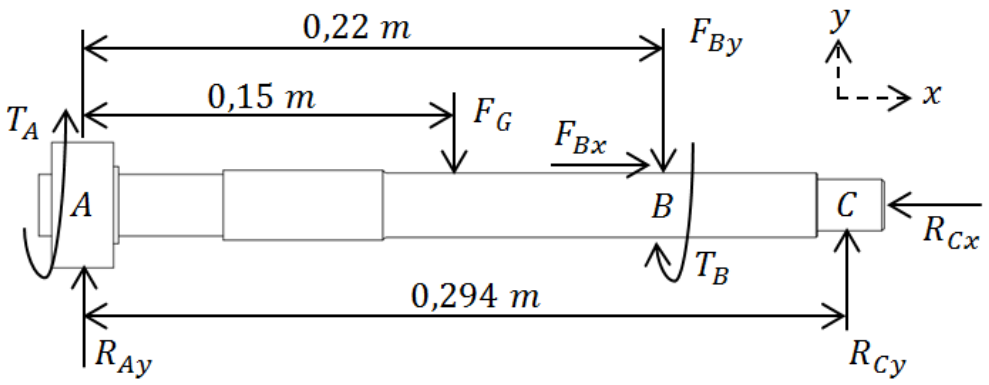

Figure 41: Free body diagram of driveshaft

The reaction forces were determined by summing the forces in the y-direction and setting them equal to zero.

$$\sum F_y = 0 \tag{D7}$$

$$\xrightarrow{yields} R_{Ay} + R_{Cy} - F_{By} - F_G = 0 \tag{D8}$$

$$\xrightarrow{yields} R_{Ay} = F_{By} + F_G - R_{Cy} \tag{D9}$$

Setting moments about point A equal to zero, yields:

$$\sum Moments_A = 0 \tag{D10}$$

$$\xrightarrow{yields} F_G(0{,}15) + F_{By}(0{,}22) - R_{Cy}(0{,}294) = 0 \tag{D11}$$

$$\xrightarrow{yields} R_{Cy} = \frac{F_G(0{,}15) + F_{By}(0{,}22)}{0{,}294} \tag{D12}$$

$$\xrightarrow{yields} R_{Cy} = 18{,}95\ N \tag{D13}$$

Substituting equation (D13) into equation (D9) yields:

$$R_{Ay} = 11{,}11\ N \tag{D14}$$

Setting the sum of the torques equal to zero, yields:

$$\sum Torque = 0 \tag{D15}$$

$$\xrightarrow{yields} T_B = T_A \tag{D16}$$

The exact torque values will be discussed later in this section. The shear force and bending moment diagrams were constructed, which indicated the worse stress due to combined loading occurring at point B. A section was then made at point B in order to determine the internal loads present at point B. The free body diagram is shown in Figure 42 below.

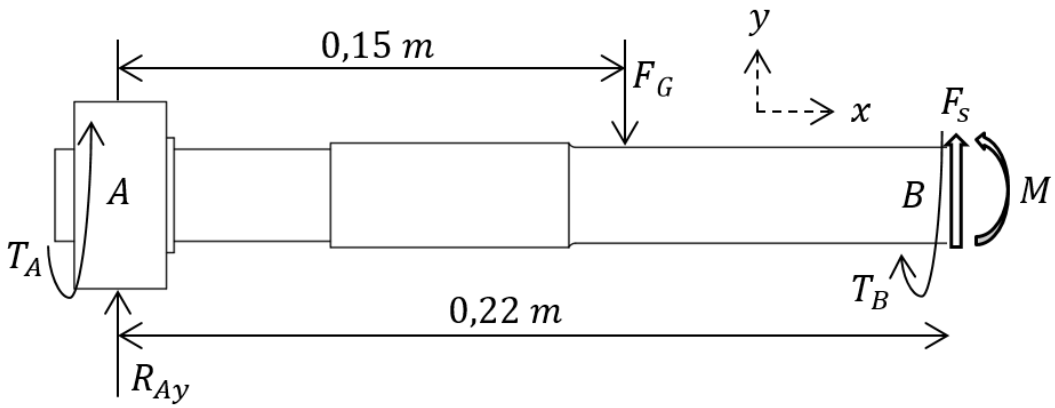

Figure 42: Free body diagram of sectioned shaft

Summing moments about point B yields:

$$\sum Moments_B = 0 \tag{D17}$$

$$\xrightarrow{yields} M + F_G(0{,}07) - R_{Ay}(0{,}22) = 0 \tag{D18}$$

$$\xrightarrow{yields} M = R_{Ay}(0{,}22) - F_G(0{,}07) \tag{D19}$$

Substituting equations (D3) and (D14) into equation (D19) yields:

$$M = 1{,}4\ N \cdot m \tag{D20}$$

The internal shear force (F_s) is not considered, due to its resulting shear stress being zero at the outer radius of the shaft where the bending and torsional stresses are a maximum.

D.4 Stress concentration factors for a keyway

The stress in a solid shaft with circular cross-section is given by equation (7.4) in Budynas & Nisbett (2008) as:

$$\tau = K_{ts}\frac{16T_x}{\pi d^3} \tag{D21}$$

with τ being the shear stress, K_{ts} the applicable shear stress concentration factor, T_x the applied torque and d being the diameter of the shaft. Popov & Balan (1999) recommends omitting the stress concentration factor (K_{ts}) from equation (D21) when calculating the maximum shear stress in the shaft. The increase in stress due to the keyway is then accounted for by reducing the value of the allowable shear stress by 25 %. As an alternative option, the literature was consulted further to obtain a more accurate indication of the stress concentration factor for the specific keyway dimensions. Figure 43 shows the dimensions of the end-milled keyway that was machined into the driveshaft. The dimensions in Figure 43 are: b = 8 mm, t = 5 mm, r = 0,3 mm and d = 25 mm.

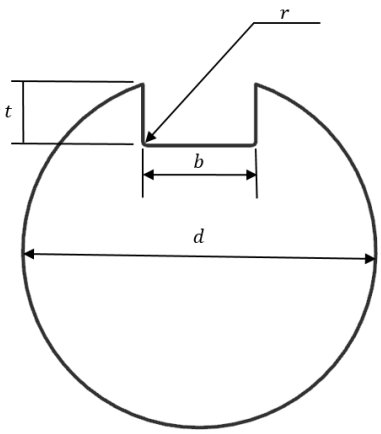

Figure 43: Keyway dimensions

The keyway in Figure 43 has a $\frac{r}{d}$ ratio of 0,012 for which Leven (1949), as cited by Pilkey (1997), recommends a stress concentration factor of $K_{ts} = 3$. The data presented by Leven (1949) is for a keyway with no key inserted. Pilkey (1997) also cites Okubo *et al.* (1968) who proposes stress concentration factors for a keyway where a key has been inserted into the keyway and where the key is used as primary means of transmitting the torque. However, given that the majority of the torque in the driveshaft being analysed is transmitted through the use of a taper lock (the key only acts as a backup to prevent the taper lock from slipping on the shaft during torque spikes), the stress concentration factors proposed by Leven (1949) was considered more representative. It is worth noting that the stress concentration factors proposed by Leven (1949) is for a keyway of width $b = \frac{d}{4}$ and depth $t = \frac{d}{8}$, which is slightly different from the analysed shaft's

keyway ratios of $b = \frac{d}{3{,}125}$ and $t = \frac{d}{5}$. However, in a study performed by Pedersen (2010), where the stress concentration factors proposed by Leven (1949) are compared to that obtained for a keyway with ratios of $b = \frac{d}{3{,}571}$ and $t = \frac{d}{10}$, it was found that Leven's (1949) data is conservative in that it slightly overestimates the value of the stress concentration factor. Nonetheless, a conservative approach was followed and the value proposed by Leven (1949) and Pilkey (1997) was implemented. That is:

$$K_{ts} = 3 \tag{D22}$$

Similar to the stress concentration factor for torsion, Chart 5.1 in Pilkey (1997) presents the stress concentration factor for a keyway subjected to bending load. For a $\frac{r}{d}$ ratio of 0,012, this chart indicates a bending stress concentration factor of:

$$K_t = 2{,}66 \tag{D23}$$

D.5 Fatigue analysis

The constant bending moment supported by the shaft results in cyclic loading of the shaft, due to the bending moment becoming completely reversed during rotation of the shaft. In addition, due to the cyclic nature of the torque output of the single-cylinder test engine, the torque transmitted by the shaft is also not constant and results in cyclic loading of the shaft. Due to the aforementioned, a fatigue analysis was performed on the shaft.

The DE-ASME Elliptic failure criteria (Budynas & Nisbett, 2008) was used to perform the fatigue analysis. This criteria neglects axial loads, as is commonly done in fatigue analysis, due to the axial loads being small and constant. Therefore, they contribute very little towards fatigue failure (Budynas & Nisbett, 2008). Using the DE-ASME Elliptic criteria, the factor of safety guarding against fatigue loading is given by equation (7.11) in Budynas & Nisbett (2008) as:

$$\frac{1}{n_F} = \frac{16}{\pi d^3}\left[4\left(\frac{K_f M_a}{S_e}\right)^2 + 3\left(\frac{K_{fs} T_a}{S_e}\right)^2 + 4\left(\frac{K_f M_m}{S_y}\right)^2 + 3\left(\frac{K_{fs} T_m}{S_y}\right)^2\right]^{0,5} \tag{D24}$$

with M_m and M_a being the midrange and alternating bending moments respectively. Similarly T_m and T_a are the midrange and alternating torsional loads. S_e is the endurance limit of the shaft and S_y is the yield strength of the material. K_f and K_{fs} are the fatigue stress concentration factors given by equation (6.32) in Budynas & Nisbett (2008) as:

$$K_f = 1 + q(K_t - 1) \tag{D25}$$

$$K_{fs} = 1 + q_s(K_{ts} - 1) \tag{D26}$$

Notch sensitivities q and q_s were determined from Figures (6.20) and (6.21) in Budynas & Nisbett (2008) as being 0,58 and 0,62 respectively. Substituting

equation (D23) into equation (D25) and equation (D22) into equation (D26) yields:

$$K_f = 1{,}96 \tag{D27}$$

$$K_{fs} = 2{,}24 \tag{D28}$$

The endurance limit S_e is defined by equation (6.18) in Budynas & Nisbett (2008) as:

$$S_e = k_a k_b k_c k_d k_e k_f S_{e'} \tag{D29}$$

with k_a through k_f being the Marin factors and $S_{e'}$ the endurance limit of the rotating test specimen. $S_{e'}$ is defined in equation (6.8) in Budynas & Nisbett (2008) as:

$$S_{e'} = 0{,}5(S_{ut}) \tag{D30}$$

$$= 0{,}5(655) \tag{D31}$$

$$= 327{,}5\ MPa \tag{D32}$$

Equation (6.19) in Budynas & Nisbett (2008) defines the surface factor k_a as:

$$k_a = a{S_{ut}}^b \tag{D33}$$

$$= 4{,}51(655)^{-0{,}265} \tag{D34}$$

$$= 0{,}81 \tag{D35}$$

Constants a and b were obtained from Table (6.2) in Budynas & Nisbett (2008). Equation (6.20) in Budynas & Nisbett (2008) defines the size factor k_b as:

$$k_b = \left(\frac{d}{7{,}62}\right)^{-0{,}107} \tag{D36}$$

$$= 0{,}88 \tag{D37}$$

with d being the diameter of the shaft (25 mm). Assuming a reliability of 99 % results in a reliability factor of:

$$k_e = 0{,}814 \tag{D38}$$

as given in Table (6.5) in Budynas & Nisbett (2008). The remaining Marin factors are all equal to one.

$$k_c = k_d = k_f = 1 \tag{D39}$$

Substituting the calculated values of the Marin factors back into equation (D29), along with the value of $S_{e'}$, results in an endurance limit of:

$$S_e = 189{,}89\ MPa \tag{D40}$$

For a rotating shaft, the bending moment is completely reversed and the bending moment's midrange component is zero (Budynas & Nisbett, 2008). The bending moment calculated in equation (D20) was considered to be the alternating

component of the bending moment load. The maximum nominal torque output ($T_{E,max}$) of the test engine (obtained from Table 16), was regarded as being the midrange torque component. The alternating torque component was then calculated by subtracting the maximum nominal torque output of the engine from the design torque (T_{design}) calculated previously in equation (C9). That is:

$$T_a = T_{design} - T_{E,max} \tag{D41}$$

$$= 123{,}8 - 27{,}5 \tag{D42}$$

$$= 96{,}3\ N \cdot m \tag{D43}$$

To summarise:

$$M_m = 0$$

$$M_a = 1{,}4\ N \cdot m$$

$$T_m = 27{,}5\ N \cdot m \tag{D44}$$

$$T_a = 96{,}3\ N \cdot m$$

Substituting equations (D44), (D40), (D27), (D28) and the yield strength from Table 10 into equation (D24) yields:

$$\frac{1}{n_f} = \frac{16}{\pi(0{,}025)^3}\left[4\left(\frac{(1{,}96)(1{,}4)}{189{,}89\times10^6}\right)^2 + 3\left(\frac{(2{,}24)(96{,}3)}{189{,}89\times10^6}\right)^2 + 3\left(\frac{(2{,}24)(27{,}5)}{415\times10^6}\right)^2\right]^{0{,}5} \tag{D45}$$

Solving for n_f yields:

$$n_f = 1{,}6 \tag{D46}$$

Considering the conservative selection of material properties and stress concentration factors during the fatigue analysis, the above factor of safety guarding against fatigue failure was considered satisfactory.

A separate check was also performed for first cycle yielding using the maximum von Mises stress given by equation (7.15) in Budynas & Nisbett (2008) as:

$$\sigma' = \left[\left(\frac{32K_f(M_m+M_a)}{\pi d^3}\right)^2 + 3\left(\frac{16K_{fs}(T_m+T_a)}{\pi d^3}\right)^2\right]^{0{,}5} \tag{D47}$$

$$= 156{,}5\ MPa \tag{D48}$$

The factor of safety guarding against first cycle yielding is therefore:

$$n_{yield} = \frac{S_y}{\sigma'} \tag{D49}$$

$$= \frac{415}{156{,}5} \tag{D50}$$

$$= 2{,}7 \tag{D51}$$

This result shows that the keyway and shaft is strong enough to prevent first cycle yielding during operation.

Appendix E: Driveshaft FEA

Due to the variance in stress concentration factors proposed in the literature, as well as not having more definitive data for the stress concentration factor for the particular dimensions of the keyway machined into the shaft, it was decided to also perform a finite element analysis of the driveshaft. The flexible coupling was already designed by catalogue as discussed in Appendix C and was not included as part of the finite element analysis. The finite element analysis thus only focuses on the stresses inside the driveshaft itself and therefore considers the flexible coupling to be a rigid element.

E.1 Model description

The finite element model was created in NX Nastran 10, using quadratic tetrahedral solid elements. General element size used was 4 mm over the majority of the model. A finer mesh (1 mm element size) was used at the fillet radii to capture the elevated stress at these points. Surface-to-surface gluing was employed to join the finer meshes at the fillet radii to the general coarser mesh of the model. The surface-to-surface gluing was performed sufficiently far from the fillet radii so as to not influence the stress distribution at the fillet radii themselves. Due to the elevated stress expected in the keyway, the inner surfaces of the keyway were meshed using an element size of 0,5 mm. The material properties used were those for AISI 4140 steel in the annealed state as presented in Table 10. Table 11 below summarises the properties of the finite element model.

Table 11: FEA model summary

Description	
Solver	NX Nastran
Time dependency	Steady state
Number of quadratic tetrahedral solid elements	85 380
Number of nodes in the model	130 701

E.2 Loads

During the stress analysis performed in Appendix D, it was found that the stress contribution from the bending load proved to be insignificantly small in comparison to the stress caused by the torsional load (the bending stress is less than 0,6 % of the torsional stress). Therefore, when performing the finite element analysis, the shaft was modelled as experiencing a pure torsional load. In Appendix C the design torque for the engine-dynamometer configuration was determined to be: T_{design} = 123,8 N·m. This is less than the maximum torque

rating of the flexible coupling, which is: $T_{F,max}$ = 160 N·m. Following a conservative approach, it was decided to use a maximum load of 160 N·m when performing the finite element analysis.

The load of 160 N·m was applied at the point A where the torque is transmitted from the constant velocity joint to the shaft. The applied torque can be seen in Figure 44 below where it is indicated with red arrows.

E.3 Constraints

A fixed constraint was applied across the face of the right-hand (dynamometer side) face of the driveshaft tip. This prevented the driveshaft from displacing in the z-direction (axial direction). All other degrees of freedom were left unconstrained at this point.

In addition, a fixed constraint was also applied in the tangential direction (θ-direction) where the taper lock (which secures the flexible coupling to the shaft) interfaces with the driveshaft. This constraint prevents the shaft from rotating and models the torque being transmitted to the flexible coupling.

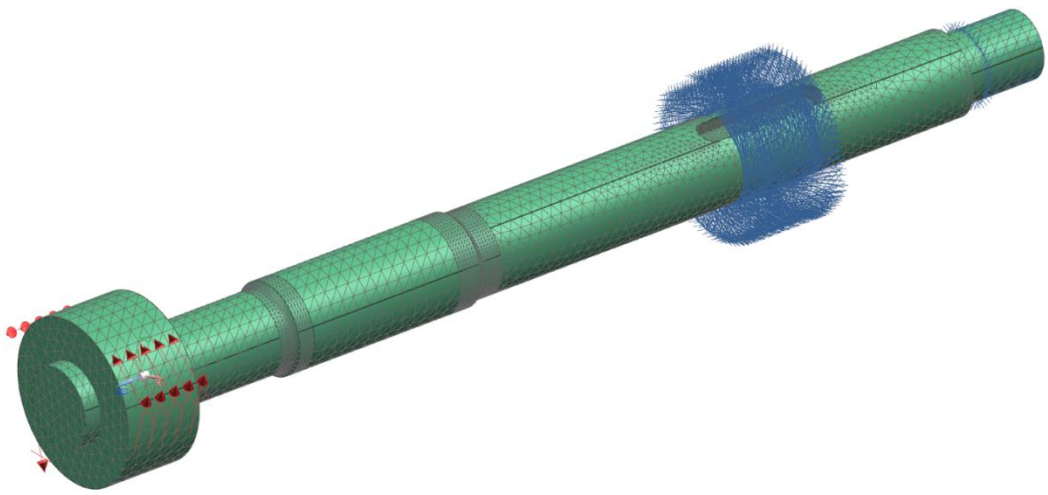

Figure 44: Model loads and constraints

E.4 Results

A linear static analysis was then performed and the maximum von Mises stress was extracted. The results obtained are presented in Figure 45 below.

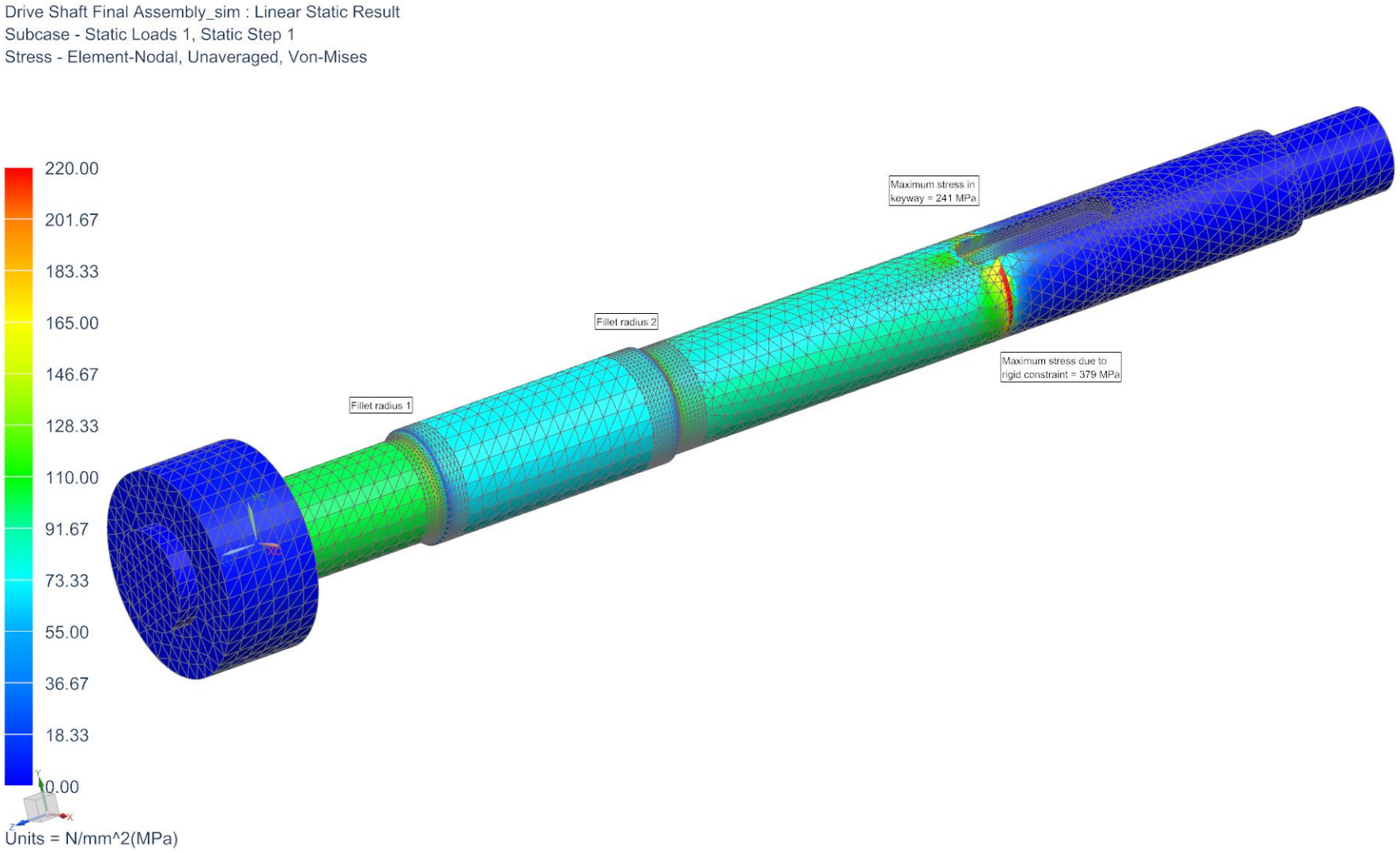

Figure 45: Von Mises stress distribution

The FEA results confirmed what was found with the hand calculations in that the stress inside the keyway is higher than at any of the two fillet radii. Furthermore, the FEA results show that the maximum stress (379 MPa) occurs right next to the taper lock where the fixed constraint was applied. This is in fact incorrect and is an artefact of the finite element model itself. This high stress occurs due to the rigid constrain that was applied in is not representative of the actual stress that the shaft experiences during operation. Neglecting the high stress next to the constraint, the results show that the second highest stress occurs at the fillet radius inside the keyway. The model was checked for convergence by refining the mesh over four iterations. Final results indicated correlation of the maximum von Mises stress, inside the keyway, to within 0,5 %. The final results show a maximum von Mises stress of 241 MPa at the fillet radius inside the keyway, as is shown in Figure 46 below.

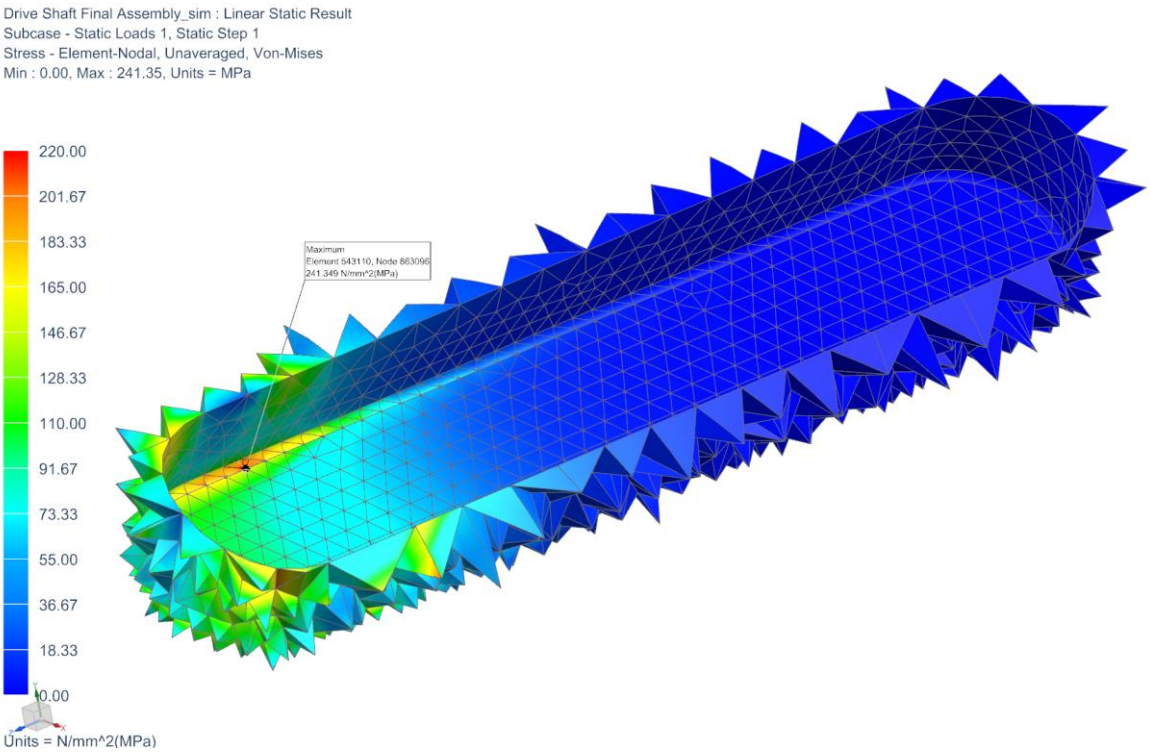

Figure 46: Maximum von Mises stress occurring in keyway

Performing a hand calculation using equations (D21) and (D22) to determine the maximum von Mises stress at the keyway for the case of the shaft experiencing pure torsion yields:

$$\tau = K_{ts}\frac{16T_x}{\pi d^3} \quad \text{(E1)}$$

$$= 3\frac{16(160)}{\pi(0{,}025)^3} \quad \text{(E2)}$$

$$= 156{,}46\ MPa \quad \text{(E3)}$$

$$= 156{,}5\ MPa \quad \text{(E4)}$$

The von Mises stress for this case of pure shear due to torsion is therefore (Budynas & Nisbett, 2008):

$$\sigma_{von\ Mises} = \sqrt{3}(\tau) \quad \text{(E5)}$$

$$= \sqrt{3}(156{,}5) \quad \text{(E6)}$$

$$= 270{,}98\ MPa \quad \text{(E7)}$$

$$= 271\ MPa \quad \text{(E8)}$$

Keeping in mind that the selected stress concentration factor has a significant influence on the final stress value, the result above shows good correlation with the result of 241 MPa obtained using the finite element analysis. Based on the FEA results, the factor of safety guarding against failure of the shaft is therefore:

$$n_{yield} = \frac{S_y}{\sigma'} \quad \text{(E9)}$$

$$= \frac{415}{241} \quad \text{(E10)}$$

$$= 1{,}7 \quad \text{(E11)}$$

Overall, the FEA results confirm (as was found with the hand calculations) that the stresses in the shaft is acceptably low for safe operation.

Appendix F: LabVIEW Software

A LabVIEW virtual instrument (VI) was developed to measure and record all engine indicating data. The VI consists of a front panel (which acts as graphical user interface) and a block diagram (where all the coding is performed). The VI was set up to use hardware triggering (obtained from the shaft encoder mounted to the crankshaft of the engine) to log both the in-cylinder and intake manifold pressures simultaneously. Apart from the pressure data, the software also records the rotational speed of the engine and then displays all measured parameters in real time on the front panel.

From the front panel the user can insert the calibration constants of both pressure transducers, control the number of cycles logged during each test, as well as define in what location and under which file name the recorded data is stored. The front panel also houses two push buttons (one button to restart the hardware triggering process and one button to stop the program). In addition, there is also a single latching button which is used to start the data logging process.

The incremental shaft encoder, which is used as a hardware trigger, outputs one trigger pulse (at TDC) per engine revolution. This means that two pulses are outputted during each four-stroke engine cycle. In the event that the wrong TDC pulse from the encoder is captured, the restart button on the front panel can be used to restart the software to shift to the next TDC pulse. The front panel and block diagram of the LabVIEW VI can be seen in Figure 47 and Figure 48 respectively.

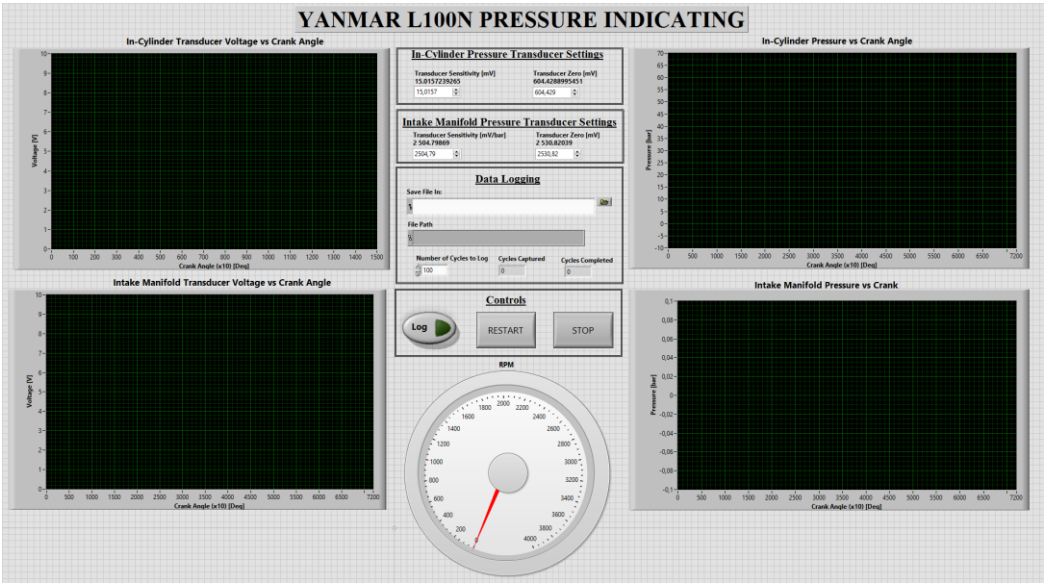

Figure 47: LabVIEW software front panel

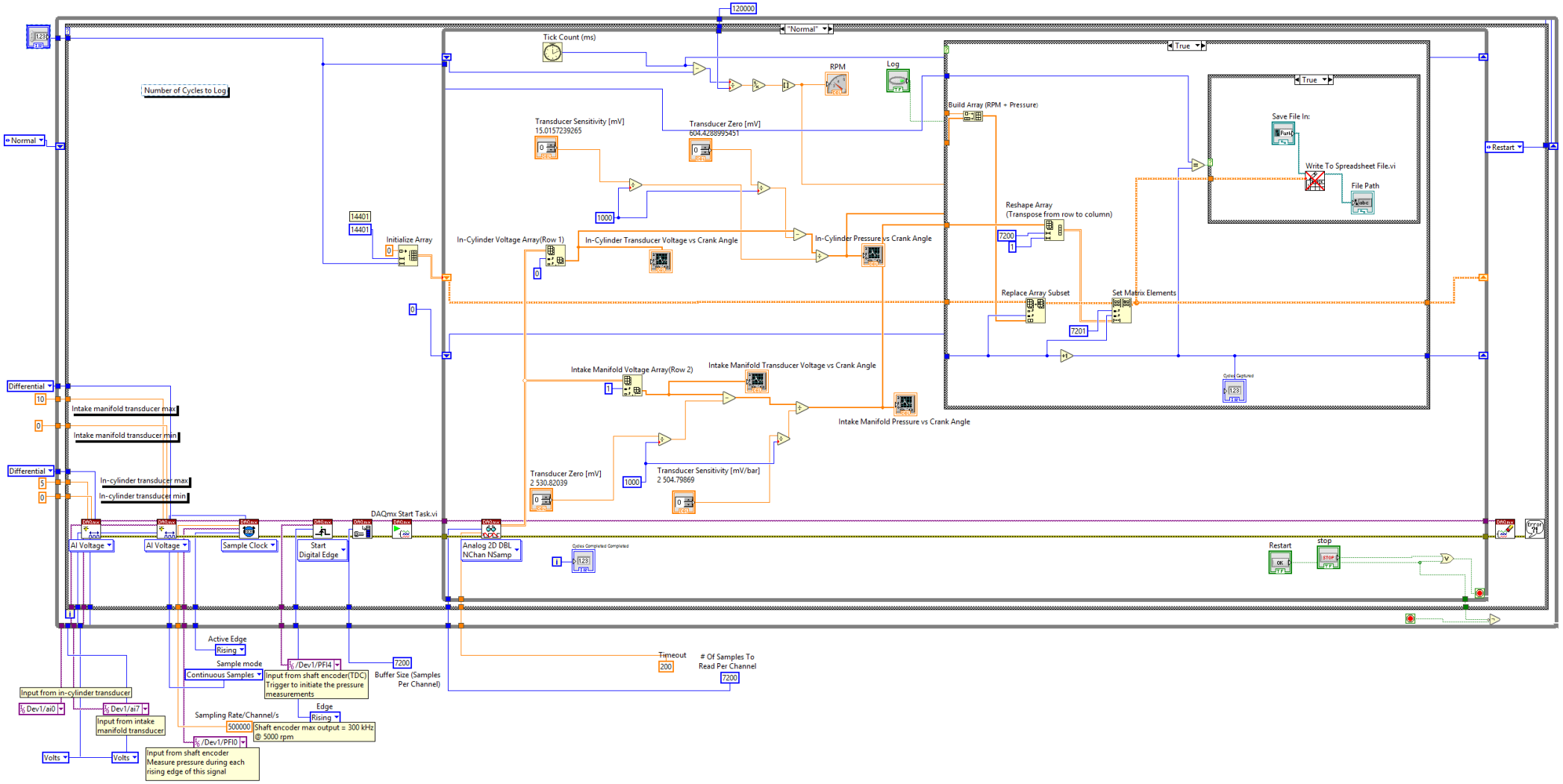

Figure 48: LabVIEW software block diagram

Appendix G: ETA Software

Figure 49 below shows the graphical user interface which was setup and configured to perform the engine testing. This interface was configured to allow complete control of the test setup, while at the same time enabling the operator to view all measured variables in real time. From within the ETA software, all the various tests were executed and the data of all measured variables were logged.

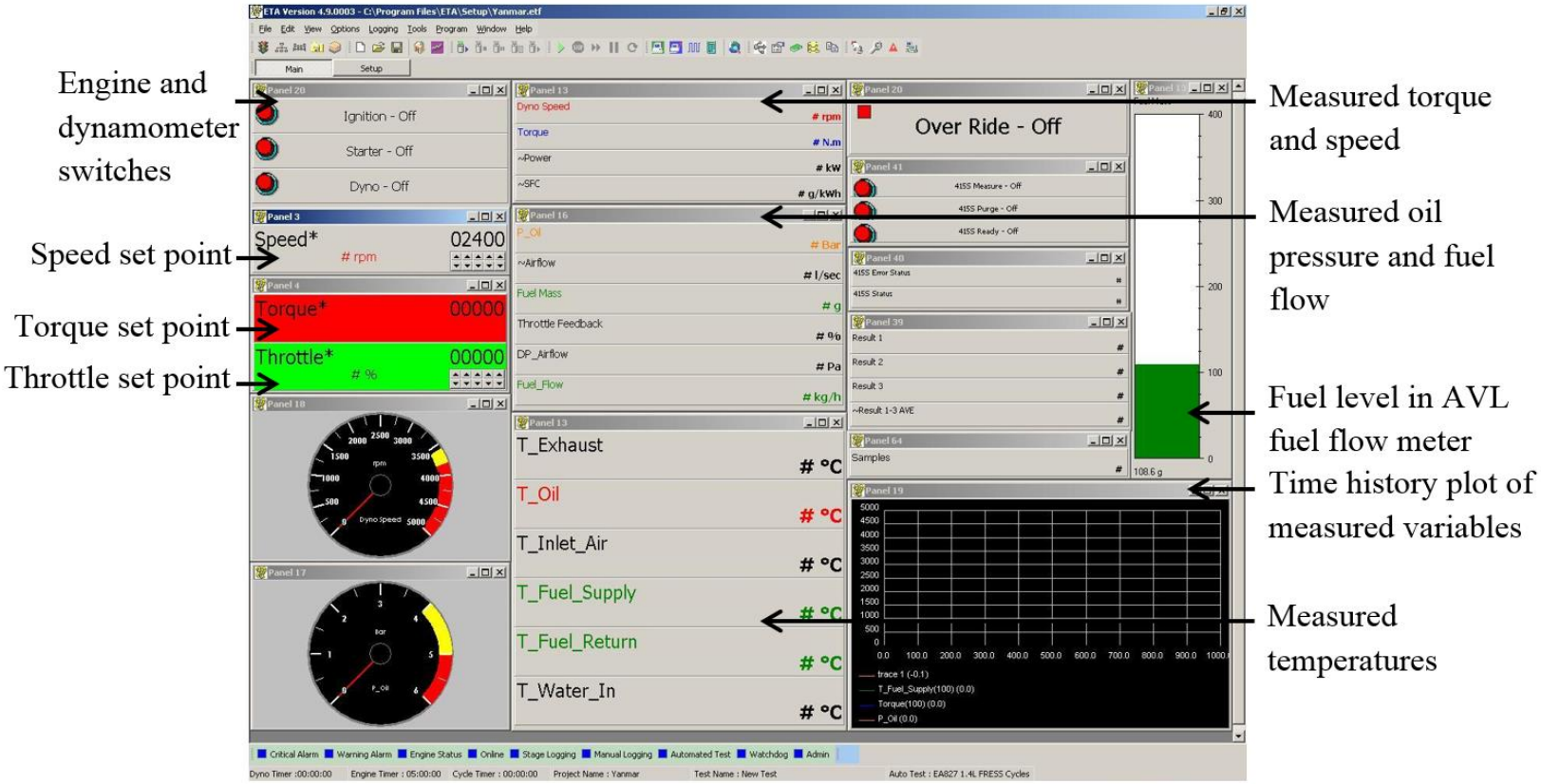

Figure 49: ETA (graphical user interface used to control the test setup)

Appendix H: Calibration Results

This section describes the calibration procedures of the various test setup instrumentation and presents the calibration results that were obtained.

H.1 Torque calibration

The calibration of the dynamometer was performed by installing the designed calibration arms onto the dynamometer and then suspending calibrating masses from the calibration arms in order to apply a known torque to the dynamometer. The output from the load cell's signal amplifier was logged (via the PLC) directly in ETA in order to include the entire measurement chain in the calibration process. The load cell output was recorded both while loading and unloading the dynamometer. This was done in order to determine if there was any hysteresis present in the system. The output during unloading of the dynamometer was consistently used to construct the torque calibration curve in ETA. Figure 50 shows the torque calibration being performed directly in ETA. The measured values are the bit values obtained from the PLC and the output values are the torque values applied to the dynamometer in N·m.

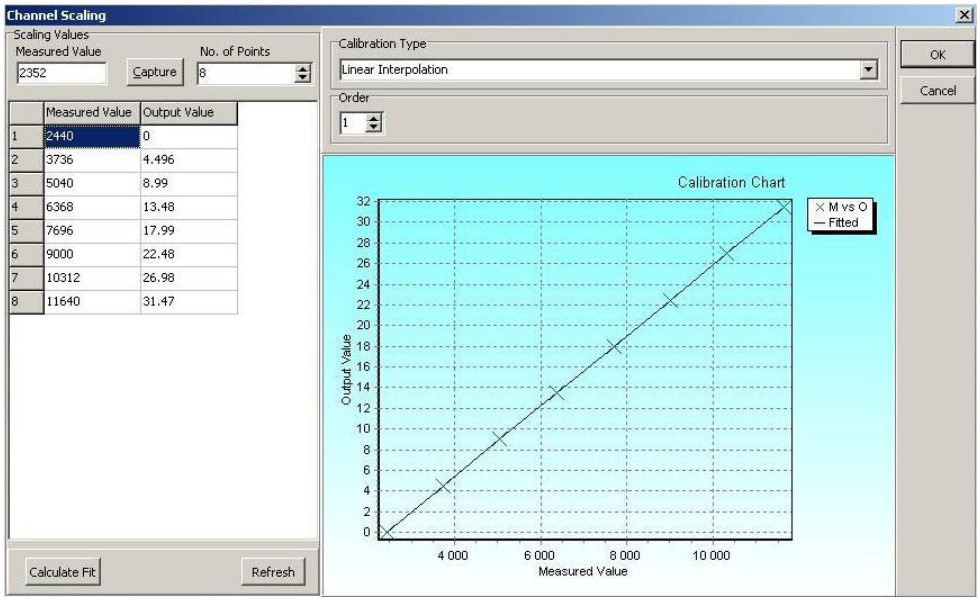

Figure 50: Dynamometer torque calibrated directly in ETA

Calibration of the dynamometer was consistently performed using a hot setup and the calibration values were recorded before and after each and every test that was performed. This was done to verify that the dynamometer output did not drift during the tests and also to confirm the repeatability of the dynamometer.

H.2 Engine indicating pressure transducers

Both the Optrand in-cylinder pressure transducer, as well as the intake manifold pressure transducer was calibrated, while connected to the NI 6351 USB data acquisition unit. The transducer outputs were then recorded in LabVIEW, thereby ensuring that the entire measurement chain was accounted for in the calibration process.

H.2.1 In-cylinder pressure transducer

During the calibration process, pressure was applied to the Optrand in-cylinder pressure transducer using a WIKA CPB 3000 dead weight tester. Differences in the local gravitational force and temperature was accounted for by applying the applicable correction factors (calculated using the equations provided in the dead weight tester's operating manual) in order to obtain the true applied pressure. The output of the in-cylinder pressure transducer was recorded both while loading (increasing the applied pressure) and unloading the transducer (decreasing the pressure applied to the transducer). This process was repeated three consecutive times to obtain the average output values for loading and unloading the transducer. The average of these two sets of data (one set representing the average output when loading the transducer and the other set the average when unloading the transducer) was then taken to construct the final calibration curve.

This calibration results are presented graphically in Figure 51, where a linear curve was fitted through the data. The gradient and y-intercept of this linear curve was then used to obtain the transducer's sensitivity and zero offset values respectively. These values are shown in Table 12 and were entered into the LabVIEW software described in Appendix F.

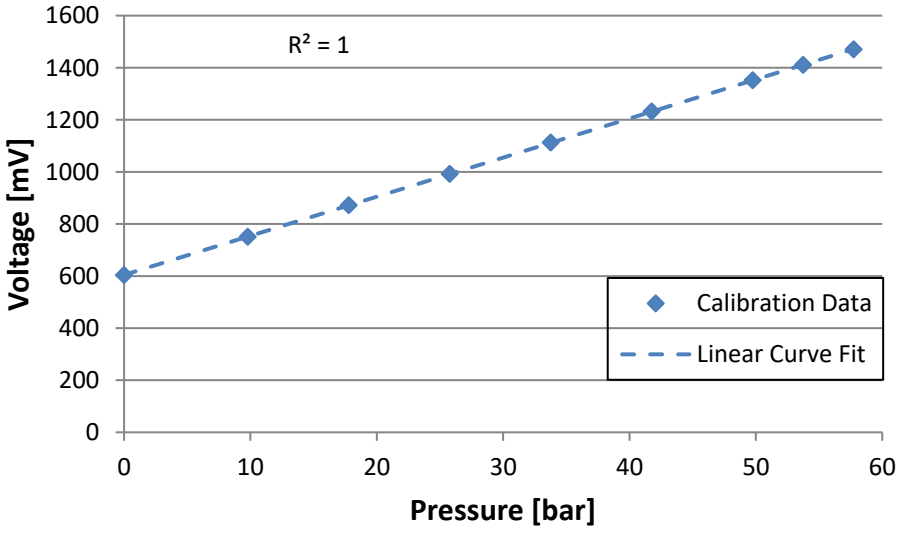

Figure 51: In-cylinder pressure transducer calibration

Table 12 below provides the average values obtained during the calibration process. Note that the transducer could only be calibrated to a maximum pressure of 57,7 bar (the dead weight tester has a maximum rating of 60 bar), even though the pressure transducer has a range of 0 - 200 bar. This is not ideal, however, given that the maximum pressure measured during all testing was 64,6 bar (see maximum pressure measured at test point 4 in Table 7), it was considered acceptable to assume that the output of the pressure transducer remains linear up to the maximum pressure measured.

Table 12: In-cylinder pressure transducer calibration values

Date		21/10/2013	
Time		17:00	
Sensitivity [mV/bar]		15	
Zero offset [mV]		604	
True Applied Pressure [bar]	**Loading Avg Voltage [mV]**	**Unloading Avg Voltage [mV]**	**Avg Voltage [mV]**
0,00	601	607	604
9,79	750	751	751
17,78	871	872	871
25,77	992	992	992
33,76	1112	1113	1113
41,75	1232	1232	1232
49,75	1352	1352	1352
53,74	1411	1411	1411
57,74	1470	1470	1470

H.2.2 Intake manifold pressure transducer

The intake manifold pressure transducer was calibrated using a pressure pump from SI Pressure Instruments, which was also capable of pulling a vacuum. The pressure applied to the pressure transducer was measured using a WIKA reference gauge. The output of the intake manifold pressure transducer was recorded both while loading and unloading the transducer (as was done for the in-cylinder pressure transducer). The calibration procedure of loading and unloading the transducer was repeated three times, after which the exact same procedure as described for the calibration of the in-cylinder pressure transducer was followed to obtain the average calibration values.

The calibration results obtained are presented graphically in Figure 52 below, where the transducer's output voltage is plotted against the applied pressure. The

output voltage is shown on the vertical axis in units of mV and the pressure is indicated on the horizontal axis in bar.

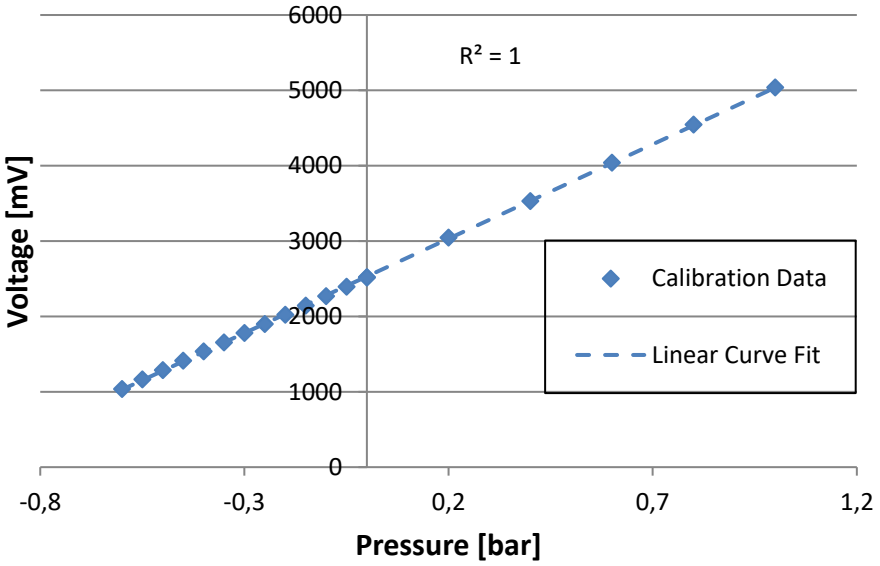

Figure 52: Intake manifold pressure transducer calibration

Figure 52 indicates that the transducer has a very linear output and a linear curve was therefore fitted to the data. The gradient and y-intercept of this linear curve was again used to obtain the transducer's sensitivity and zero offset values (see Table 13 which shows the raw calibration data). These sensitivity and zero offset values were also entered into the LabVIEW software described in Appendix F.

Table 13: Intake manifold transducer calibration values

Date		15/10/2013	
Time		12:00	
Sensitivity [mV/bar]		2505	
Zero offset [mV]		2531	
Applied Pressure [bar]	**Loading Avg Voltage [mV]**	**Unloading Avg Voltage [mV]**	**Avg Voltage [mV]**
-0,60	1035	1040	1037
-0,55	1160	1167	1163
-0,50	1284	1292	1288
-0,45	1410	1413	1412
-0,40	1534	1537	1535
-0,35	1656	1654	1655
-0,30	1779	1780	1780
-0,25	1898	1900	1899
-0,20	2021	2023	2022
-0,15	2145	2143	2144
-0,10	2270	2269	2269
-0,05	2394	2392	2393
0,00	2513	2515	2514
0,00	2517	2524	2520
0,20	3046	3046	3046
0,40	3518	3541	3530
0,60	4038	4041	4039
0,80	4554	4539	4546
1,00	5038	5038	5038

H.3 Thermocouples

All thermocouple sensors were calibrated using a Fluke 9142 field metrology well and a calibrated platinum resistance thermometer was used to indicate the reference temperature. The thermocouples were calibrated directly in ETA, in order to include the entire measurement chain in the calibration process.

Calibration was performed from 0 °C to 140 °C in increments of 20 °C, both while increasing and decreasing the temperature set point values. The average of the two data sets obtained (for each thermocouple sensor) was then used as the final calibration values for each particular sensor. The averaged calibration values are presented in Table 14 below.

Table 14: Thermocouple calibration results

Set Point [°C]	Exhaust [°C]	Oil [°C]	Inlet Air [°C]	Fuel Supply [°C]	Ambient [°C]
0,0	0,7	0,8	1,2	0,7	0,7
20,0	19,9	19,8	19,9	19,5	19,7
40,0	40,0	39,4	39,4	38,9	38,9
60,0	59,8	58,8	58,8	58,5	58,4
80,0	79,5	78,6	78,4	78,2	78,2
100,0	99,7	98,4	98,2	97,8	98,0
120,0	120,1	118,7	118,3	118,1	118,2
140,0	140,7	139,1	138,5	138,6	138,6

H.4 Fuel flow meter

The AVL dynamic fuel balance was calibrated upon installation following the detailed calibration procedure in the fuel flow meter's user manual. The fuel flow meter came supplied with a 50,00 g calibrating mass to be used during the automatic calibration sequence. During the first step of the calibration process the gain setting was verified as being correct by weighing the mass (using the fuel flow meter with the measuring vessel filled halfway) and ensuring that the error between the mass reported by the fuel flow meter and the actual mass of the calibrating mass was within the allowed tolerance band stipulated in the fuel flow meter's user manual. The user manual stipulates an allowable error of ± 0,06 g when measuring the mass. After making a fine adjustment to the gain, the measured mass obtained was 50,00 g.

Next, the fuel flow meter's linearity was verified by comparing the deviation in two calibration values, one obtained with the measuring vessel full and the other with the vessel almost empty. The allowable difference between the two measurements again had to be within 0,06 g. The calibration process was repeated a number of times to verify that repeatable measurements could be obtained, all of which were within the allowable deviation allocated for linearity. Finally, the output from the fuel flow meter's controller was calibrated directly in ETA to ensure that the fuel flow rate displayed in ETA was the same as that displayed by the fuel flow meter's control unit.

H.5 Equipment

The details of the various equipment used during testing and calibration are presented in Table 15 below.

Table 15: Equipment details

Equipment	Description	Serial #
Test setup hardware		
Test engine	Yanmar L100N	S29283
Electric motor	18,5 kW WEG 2-pole, 380 V, B3/B5T	No number
Fuel flow meter	AVL 730 dynamic fuel balance	1555
Load cell	500 kgf HBM U2A	C48422
Load cell amplifier	LCS/I/0350	No number
Engine shaft encoder	Leine Linde RHI 503	36967650
Dynamometer shaft encoder	Turck incremental rotary encoder	Ri-12H15E-2B500-H1181 (Catalogue #)
Engine indicating instrumentation		
In-cylinder pressure transducer	Optrand AutoPSI	7773B
Intake manifold pressure transducer	WIKA S-10	11044RY3
Signal converter	PR Electronics 3104	Not available
Data acquisitioning unit	NI 6351 USB	15F405E
VSD	AB PowerFlex 753	No number
Brake resistor	Penbro Kelnick 18 kW	61532 33E
PLC		
PLC base unit	MicroLogix 1500 (1764-24BWA)	Ser A, Rev A
DeviceNet scanner	DeviceNet (1769-SDN)	Ser A, Rev 1
DeviceNet adapter	DeviceNet (1794-ADN)	Ser B, Rev A01
Analog output module	Analog output (1794-OE4/B)	No number
Analog input module	Analog input (1794-IE8/B)	No number
Thermocouple input module	Thermocouple (1794-IT8)	No number
Throttle actuator system	TGS Posicon 1000	
Control unit	TGS 1001	1001.0401.016
Actuator	TGS 1003	1003.0401.018
Smoke meter	AVL 415 variable sampling	No number
Calibration equipment		
Dead weight tester	WIKA CPB 3000	30285
Pressure and vacuum pump	SI Pressure Instruments	165829
Reference gauge	WIKA master gauge	No number
Field metrology well	Fluke 9142	B53479

Appendix I: Test Engine Specifications

The specifications of the test engine used are presented in Table 16 below and the manufacturer's performance curves for the engine are shown in Figure 53.

Table 16: Test engine specifications

Specification		Unit	Yanmar L100N
Number of cylinders		-	1
Bore x stroke		mm	86 x 75
Displacement		L	0,435
Compression ratio		-	19,7:1
Continuous rated output	**Engine speed**	rpm	3600
	Output	kW	6,6
Maximum Rated Output	**Engine speed**	rpm	3600
	Output ($P_{E,max}$)	kW	7,4
Max speed/High idle		rpm	3800 ± 30
Max torque at 2200 - 2700 rpm ($T_{E,max}$)		N·m	27,5

(Data Source: Yanmar Industrial Engines - Operation Manual, [S.a.])

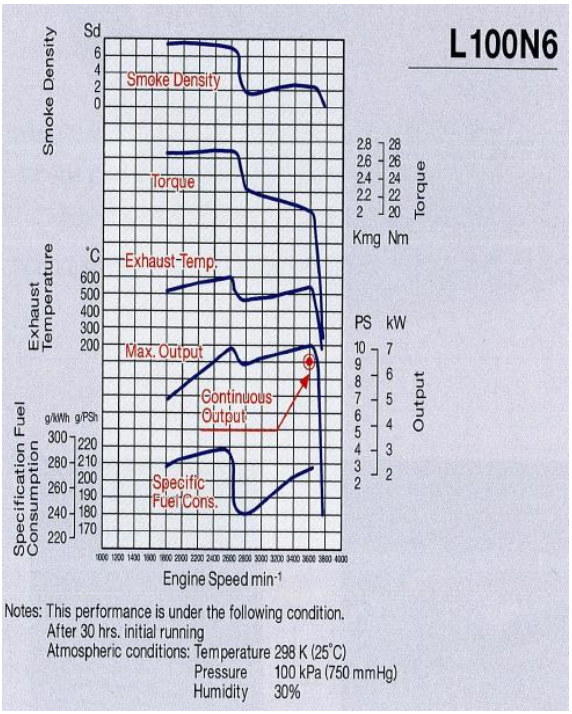

Figure 53: Yanmar L100N performance curves

(Source: Yanmar L100N Performance Curves [S.a.])

Appendix J: Engine Indicating Figures

For each of the engine indicating test points shown in Table 7, the complete heat release analysis was performed and the pressure, P - V, log P – log V and dP/dθ curves were generated. All of these curves were then plotted once more for the repeat tests of the test points in Table 7. Figure 54 and Figure 55 shows the P - V and dP/dθ curves, respectively for test point 4 in Table 7.

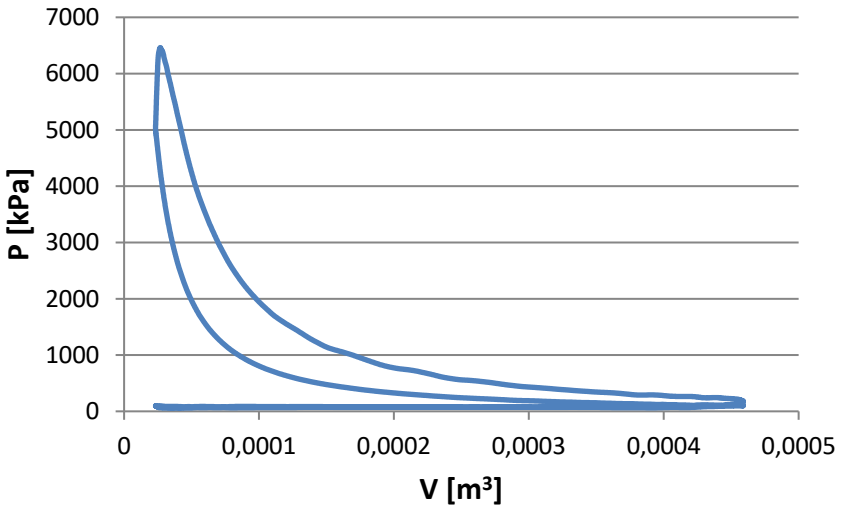

Figure 54: Pressure versus volume diagram for 20 N·m at 2400 rpm

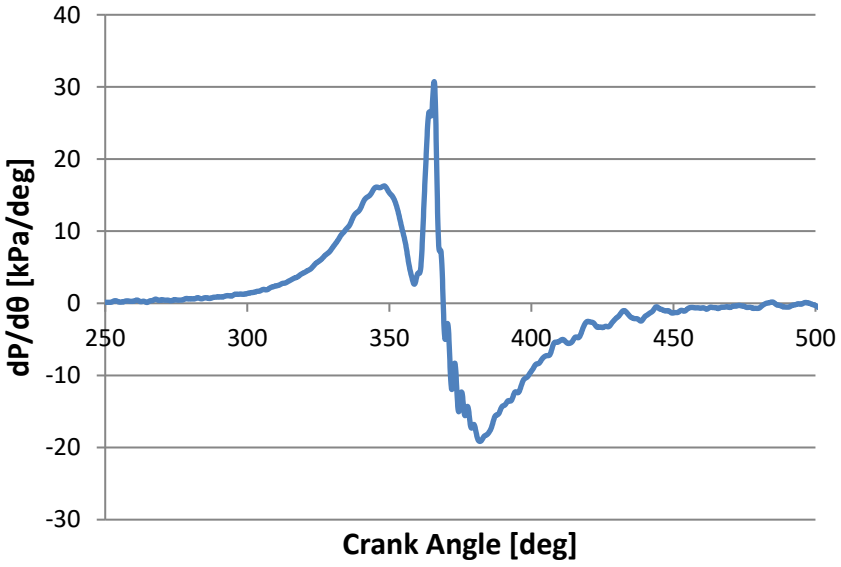

Figure 55: dp/dθ curve for 20 N·m at 2400 rpm

Appendix K: Test Data

Table 17: Numerical data used to produce Figure 23

x	x	Calculated using: y = 6,924x + 0,183	Calculated using: y = 6,962x - 0,139		
Voltage (Loading) [V]	**Voltage (Unloading) [V]**	**Torque (Loading) [Nm]**	**Torque (Unloading) [Nm]**	**Difference [Nm]**	**Difference [%]**
0,01	0,04	0,25	0,14	0,1	-
0,61	0,65	4,41	4,39	0,0	0,5
1,26	1,30	8,91	8,91	0,0	0,0
1,91	1,96	13,41	13,51	0,1	0,7
2,56	2,60	17,91	17,96	0,1	0,3
3,21	3,25	22,41	22,49	0,1	0,4
3,87	3,90	26,98	27,01	0,0	0,1
4,53	4,55	31,55	31,54	0,0	0,0
5,19	5,19	36,12	35,99	0,1	0,3
			Average Difference [%]:		0,3

Table 18: Numerical data used to produce Figure 24

x	x	Calculated using: y = 6,988x - 0,065	Calculated using: y = 6,984x - 0,001		
Voltage (Pre-Testing) [V]	**Voltage (Post-Testing) [V]**	**Torque (Pre-Testing) [Nm]**	**Torque (Post-Testing) [Nm]**	**Difference [Nm]**	**Difference [%]**
0,03	0,02	0,14	0,14	0,0	-
0,64	0,63	4,41	4,40	0,0	0,2
1,28	1,28	8,88	8,94	0,1	0,7
1,94	1,92	13,49	13,41	0,1	0,6
2,58	2,58	17,96	18,02	0,1	0,3
3,23	3,22	22,51	22,49	0,0	0,1
3,88	3,87	27,05	27,03	0,0	0,1
4,52	4,52	31,52	31,57	0,0	0,1
5,16	5,15	35,99	35,97	0,0	0,1
			Average Difference [%]:		0,3

Table 19: BSFC repeatability data for Figure 28

Test Point	Test 1		Test 2		BSFC Difference [%]
	BMEP [kPa]	BSFC [g/kWh]	BMEP [kPa]	BSFC [g/kWh]	
5 N·m at 2400 rpm	140,9	375,0	139,2	380,0	1,4
10 N·m at 2400 rpm	280,2	272,1	279,9	272,2	0,0
15 N·m at 2400 rpm	425,0	240,8	426,7	243,2	1,0
20 N·m at 2400 rpm	563,4	232,0	566,0	236,0	1,7
20 N·m at 2800 rpm	564,1	241,6	566,0	242,6	0,4
15 N·m at 2800 rpm	425,1	244,7	426,0	250,9	2,5
10 N·m at 2800 rpm	280,5	281,2	279,6	282,3	0,4
5 N·m at 2800 rpm	141,6	396,0	140,0	407,8	3,0
5 N·m at 3200 rpm	141,3	426,4	139,0	440,9	3,4
10 N·m at 3200 rpm	280,1	293,2	279,9	299,3	2,1
15 N·m at 3200 rpm	425,5	258,1	426,4	262,5	1,7
20 N·m at 3200 rpm	563,7	248,5	566,1	252,4	1,6
		Average Difference [%]:			1,6

Table 20: Exhaust gas temperature repeatability data for Figure 29

Test Point	Test 1		Test 2		T_Exhaust Difference [%]
	BMEP [kPa]	T_Exhaust [°C]	BMEP [kPa]	T_Exhaust [°C]	
5 N·m at 2400 rpm	140,9	165,8	139,2	171,2	3,3
10 N·m at 2400 rpm	280,2	228,9	279,9	238,9	4,3
15 N·m at 2400 rpm	425,0	307,0	426,7	321,2	4,6
20 N·m at 2400 rpm	563,4	397,4	566,0	413,2	4,0
20 N·m at 2800 rpm	564,1	438,5	566,0	454,2	3,6
15 N·m at 2800 rpm	425,1	345,5	426,0	357,0	3,3
10 N·m at 2800 rpm	280,5	262,1	279,6	270,0	3,0
5 N·m at 2800 rpm	141,6	191,6	140,0	196,5	2,5
5 N·m at 3200 rpm	141,3	221,6	139,0	226,0	2,0
10 N·m at 3200 rpm	280,1	293,0	279,9	299,9	2,3
15 N·m at 3200 rpm	425,5	381,0	426,4	389,9	2,3
20 N·m at 3200 rpm	563,7	486,7	566,1	502,2	3,2
			Average Difference [%]:		3,2

Table 21: Inlet air temperature data for section 7.4

Test Point	Test 1 [°C]	Test 2 [°C]	Difference [°C]
5 N·m at 2400 rpm	23,3	27,2	3,8
10 N·m at 2400 rpm	22,3	26,3	4,0
15 N·m at 2400 rpm	23,2	27,1	3,9
20 N·m at 2400 rpm	24,8	28,8	4,0
20 N·m at 2800 rpm	26,4	30,4	4,0
15 N·m at 2800 rpm	27,0	30,4	3,4
10 N·m at 2800 rpm	26,0	28,8	2,8
5 N·m at 2800 rpm	24,7	27,1	2,4
5 N·m at 3200 rpm	24,1	25,8	1,7
10 N·m at 3200 rpm	24,8	26,0	1,3
15 N·m at 3200 rpm	26,4	27,1	0,7
20 N·m at 3200 rpm	28,7	29,0	0,3
		Average Difference [°C]:	2,7

Table 22: BSFC data for Figure 32

Test Point	Diesel		B10		BSFC Difference [%]
	BMEP [kPa]	BSFC [g/kWh]	BMEP [kPa]	BSFC [g/kWh]	
5 N·m at 2400 rpm	157,9	334,5	159,2	340,1	1,7
10 N·m at 2400 rpm	296,6	254,5	299,1	262,7	3,2
15 N·m at 2400 rpm	440,8	234,6	446,4	234,5	0,0
20 N·m at 2400 rpm	577,8	230,1	585,1	232,6	1,1
20 N·m at 2800 rpm	577,7	233,2	584,8	238,2	2,1
15 N·m at 2800 rpm	441,0	240,6	446,0	245,1	1,9
10 N·m at 2800 rpm	296,7	266,5	299,1	275,4	3,3
5 N·m at 2800 rpm	157,7	360,3	159,0	368,8	2,4
5 N·m at 3200 rpm	157,7	378,6	157,9	394,7	4,3
10 N·m at 3200 rpm	297,0	276,0	299,4	285,1	3,3
15 N·m at 3200 rpm	440,7	248,4	445,9	254,5	2,4
20 N·m at 3200 rpm	578,2	242,4	585,0	248,5	2,5

Table 23: Smoke data for Figure 33

Test Point	Diesel		B10	
	BMEP [kPa]	Smoke [FSN]	BMEP [kPa]	Smoke [FSN]
5 N·m at 2400 rpm	156,6	0,09	152,1	0,09
10 N·m at 2400 rpm	295,4	0,27	292,2	0,28
15 N·m at 2400 rpm	440,2	0,72	438,0	0,70
20 N·m at 2400 rpm	577,6	1,63	576,7	1,52
20 N·m at 2800 rpm	577,7	1,29	575,8	1,78
15 N·m at 2800 rpm	440,5	0,72	438,0	0,61
10 N·m at 2800 rpm	295,6	0,31	291,9	0,26
5 N·m at 2800 rpm	156,5	0,09	152,1	0,10
5 N·m at 3200 rpm	156,5	0,11	151,7	0,11
10 N·m at 3200 rpm	295,6	0,35	292,4	0,30
15 N·m at 3200 rpm	440,3	0,69	437,5	0,66
20 N·m at 3200 rpm	577,6	1,69	576,7	1,42

Table 24: Heat release data for section 9.6

Test Point	Test 1				Test 2			
	SOI [°]	SOC [°]	Ignition Delay [°]	Max ROHR [J/0,1°]	SOI [°]	SOC [°]	Ignition Delay [°]	Max ROHR [J/0,1°]
5 N·m at 2400 rpm	347,3	359,2	11,9	3,2	347,2	359,2	12,0	3,2
20 N·m at 2400 rpm	348,2	358,7	10,5	3,65	348,0	358,7	10,7	3,6
5 N·m at 3200 rpm	347,3	360,8	13,5	2,7	347,3	360,8	13,5	2,7
20 N·m at 3200 rpm	348,5	360,1	11,6	3,9	348,8	360,1	11,3	3,9

References

4140 High Tensile. [S.a.]. [Online]. Available: http://www.ssm.co.nz/sitefiles/4140.pdf. [2012, November 12].

AISI 4140 Steel, annealed at 815°C. [S.a.]. [Online]. Available: http://www.matweb.com/search/DataSheet.aspx?MatGUID=7b75475aa1bc41618788f63c6500d36b&ckck=1. [2012, November 12].

AISI 4140 Chrome-Molybdenum High Tensile Steel. 2012. [Online]. Available: http://www.azom.com/article.aspx?ArticleID=6116#18. [2012, November 12].

AISI 4140 Search Results. [S.a.]. [Online]. Available: http://www.matweb.com/search/QuickText.aspx?SearchText=aisi%204140. [2012, November 12].

Annand, W. J. D. 1963. Heat Transfer in the Cylinders of Reciprocating Internal Combustion Engines. *Proceedings of the Institution of Mechanical Engineers*, 1963 177:973.

Atkins, R.D. 2009. *An Introduction to Engine Testing and Development.* Third Edition. Warrendale: SAE International.

AutoPSI Pressure Sensor Operating Instructions. 2009. [Online]. Available: http://www.optrand.com/autopsi_man091809.pdf. DOC #: OD-002 REV E. [2013, January 01].

AVL. 2002. *Engine Indicating - AVL User Handbook.* Austria.. PA0671E.

Aziz, A.A., Said, M.F., Awang, M.A., Said, M. 2006. *The Effects of Neutralized Palm Oil Methyl Esters (NPOME) on Performance and Emission of a Direct Injecton Diesel Engine.* [Online]. Available: http://eprints.utm.my/3383/1/The_Effects_of_Neutralized_Palm_Oil_Methyl_Esters__NPOME__on.pdf. [2015, July 14].

Balistrou, M., Loubar, K., Lounici, M.S. & Tazerout, M. 2010. Investigation on heat transfer evaluation for a more efficient two-zone combustion model in the case of natural gas SI engines. *Applied Thermal Engineering 31*, 2-3 (2010) 319.

Baranescu, R. & Challen, B. 1999. *Diesel Engine Reference Book*. Second Edition. Oxford: Butterworth-Heinemann. ISBN 0 7506 2176 1.

Biofuels Industrial Strategy of the Republic of South Africa. 2007. [Online]. Available: http://www.energy.gov.za/files/esources/petroleum/biofuels_indus_strat.pdf(2).pdf. [2016, October 12].

Blair, G.P. 1999. *Design and Simulation of Four-Stroke Engines.* SAE International. ISBN: 978-0-7680-0440-3.

Boles, M.A. & Cengel, Y.A. 2007. *Thermodynamics: An Engineering Approach*. Sixth Edition (SI Units). Singapore: McGraw-Hill.

BP Statistical Review of World Energy. 2016. [Online]. Available: http://www.bp.com/content/dam/bp/pdf/energy-economics/statistical-review-2016/bp-statistical-review-of-world-energy-2016-full-report.pdf. [2016, October 12].

Budynas, R.G. & Nisbett, J.K. 2008. Shigley's Mechanical Engineering Design. 8th Edition in SI Units. Singapore: McGraw-Hill. ISBN: 978-007-125763-3.

Bueno, A.V., Velásquez, J.A., Milanez, L.F. 2012. *Internal Combustion Engine Indicating Measurements*. [Online]. Available: http://www.intechopen.com/books/applied-measurement-systems/internal-combustion-engine-indicating-measurements. [2013, November 15].

Cabris (Pty) Ltd. 1992. *Flexible shafts*, page 128. Fax communication 2 December 1992.

Chapman, S.J. 2005. *Electric Machinery Fundamentals*. Fourth Edition. Singapore: McGraw-Hill.

Corbett, J.H. 2017. *Application of an Engine Management System to a Stationary Spark Ignition Engine.* Stellenbosch. (unpublished thesis)

Drive Design and Maintenance Manual. [S.a.]. [Online]. Available: http://www.fptgroup.com/dss/docs/708_05_Fenner_Couplings.pdf [2012, July 15].

Dynamometer Comparison. [S.a]. [Online]. Available: http://www.dynesystems.com/what-is-a-dynamometer.htm [2012, December 15].

Dynamometer Engine Testing. 2011. [Online]. Available: http://www.pcc-sterling.com/Pages/dynamometer-testing.html. [2013, January 01].

Dynamometer Review. [S.a.]. [Online]. Available: http://www.engineersedge.com/industrial-equipment/dynamometer-review.htm. [2014, January 24].

Encoder Technology - Details and Descriptions. 2014. [Online]. Available: http://www.leinelinde.com/ support/downloads/. Part no: 1073559-01, ver. 03. [2014, November 19].

EPA. 2015. *Renewable Fuel Standard Program: Standards for 2014, 2015, and 2016 and Biomass-Based Diesel Volume for 2017.* Final Rule. [Online]. Available: https://www.gpo.gov/fdsys/pkg/FR-2015-12-14/pdf/2015-30893.pdf. [2016, October 5].

Engine Combustion Analysis. 2012. [Online]. Available: https://www.kistler.com/fileadmin/files/divisions/automotive-research-test/engines-research-and-development/pruefstand-indizieren/100-459e-08.12.pdf. [2015, April 12].

Engine Combustion Modelling – An Introduction. [S.a.]. [Online]. Available: http://www.me.ua.edu/me418/lecture_notes/Engine%20combustion%20modeling.pdf. [2013, October 09].

Engine Testing Overview. [S.a.]. [Online]. Available: http://www.sussex.ac.uk/Users/tafb8/eti/eti_03_EngineTestingOverview.pdf. [2013, January 01].

Ferguson, C.R. & Kirkpatrick, A.T. 2001. *Internal Combustion Engines Applied Thermosciences.* Second Edition. New York: John Whiley & Sons.

Finol, C.A. & Robinson, K. 2006. *Thermal modelling of modern engines: A review of empirical correlations to estimate the in-cylinder heat transfer coefficient*. [Online]. Available: http://pid.sagepub.com/content/220/12/1765.full.pdf. [2013, November 4].

Goering, C.E. 1998. Engine Heat Release Via Spreadsheet. *Transactions of the ASAE.* Vol. 41(5): 1249-1253.

Gopinath, D. & Sundaram, E.G. 2015. *Experimental Studies on Performance and Emission Characteristics of Diesel Engine Fuelled with Neem Oil Methyl Ester Blends*. [Online]. Available: http://www.rericjournal.ait.ac.th/index.php/reric/article/viewFile/1348/463. [2015, July 20].

Grobbelaar, E. 2011. *The Development of a Small Diesel Engine Test Bench for Biodiesel Testing.* Final Year Mechanical Project. Stellenbosch University.

Grobbelaar, E. & Haines, R.W. 2012. *The Development of a Small Diesel Engine Test Bench Employing an Electric Dynamometer – Proposal Document.* Document Provided to Outside Contractor Installing Drive Unit. Stellenbosch University.

GX670 Engine Adjustment Information. 2010. [Online]. Available: http://cssportal.css-club.net/honda/PowerProducts/contents/1071132en.pdf. [2012, March 24].

Heywood, J.B. 1988. *Internal Combustion Engine Fundamentals*. USA: McGraw-Hill. ISBN 0-07-028637-X.

High Strength Bars. [S.a.]. [Online]. Available: http://www.associatedsteel.com/high-strength-steel-bars/alloys-kromite3.shtml. [2012, November 12].

Honda Owner's Manual - GX670. 2007. [Onine]. Available: http://cdn.powerequipment.honda.com/engines/pdf/manuals/00X37Z6C6030.pdf. [2012, March 24].

How to Test Engine Compression. [S.a.]. [Online]. Available: http://www.agcoauto.com/content/news/p2_articleid/287. [2014, October 14].

Huang, D., Haining, Z., Li, L. 2012. Biodiesel: An Alternative to Conventional Fuel. *Energy Procedia* 16 (2012) 1974-1885.

Induction Motor Speed Torque Characteristics. 2006. [Online]. Available: https://www.yaskawa.com/pycprd/download/home#tab1. [2015, February 18].

Killedar, J.S. 2012. *Dynamometer - Theory and Application to Engine Testing*. USA: Xlibris. ISBN 978-1-4771-2006-4.

Klein, M. 2007. *Single-zone Cylinder Pressure Modeling and Estimation for Heat Release Analysis of SI Engines*. [Online]. Available: http://www.vehicular.isy.liu.se/Publications/PhD/07_PhD_1124_MK.html. [2013, September 10].

Lancaster, D.R., Krieger, R.B. & Lienesch, J.H. 1975. Measurement and Analysis of Engine Pressure Data. *SAE Technical Paper*. DOI: 10.4271/750026

Martyr, A.J. & Plint, M.A. 2007. *Engine Testing Theory and Practice.* Third Edition. Oxford: Butterworth-Heinemann.

McCormick, R.L. & Parish, R. 2001. Milestone Report: Technical Barriers to the Use of Ethanol in Diesel Fuel. *Advanced Petroleum Based Fuels Program and Renewable Diesel Program.* NREL/MP-540-32674.

Merker, G.P., Schwarz, C., Teichmann, R. 2012. *Combustion Engines Development – Mixture Formation, Combustion, Emissions and Simulation.* London: Springer. ISBN 978-3-642-02951-6.

Milton, B.E. 2005. *Thermodynamics, Combustion and Engines*. Australia: School of Mechanical and Manufacturing Engineering, UNSW.

Ozsezen, A.N. & Canakci, M. 2011. Determination of performance and combustion characteristics of a diesel engine fueled with canola and waste palm oil methyl esters. *Energy Conversion and Management*. Volume 52, Issue 1, Pages 108–116.

Pedersen, N.L. 2010. *Stress concentrations in keyways and optimization of keyway design.* The Journal of Strain Analysis for Engineering Design. Vol 45, No 8. November 2010.

Pilkey, W.D. 1997. *Peterson's Stress Concentration Factors*. Second Edition. New York: John Wiley & Sons.

Piston Kit for Yanmar L100 Engine. [S.a.]. [Online]. Available: http://www.carbydoctor.com.au/piston-kit-for-yanmar-l100-engine-86mm-rings-circl. [2015, October 11].

Popov, E.P. & Balan, T.A. 1999. *Engineering Mechanics of Solids*. Second Edition. New Jersey: Prentice Hall. ISBN: 0-13-081534-9.

Pressure Sensors for Combustion Analysis. 2013. [Online]. Available: https://www.avl.com/documents/10138/885965/AVL+Pressure+Sensors+for+Combustion+Analysis/6c844a54-7a84-429d-8e57-4f34e948f95d. [2016, August 05].

Pulkrabek, W.W. 1997. *Engineering Fundamentals of the Internal Combustion Engine*. New Jersey: Prentice Hall.

Randolph, A. 1990. Methods of Processing Cylinder-Pressure Transducer Signals to Maximize Data Accuracy. *SAE Technical Paper.* DOI:10.4271/900170

SAE J1349 Standard. 2004. *Engine Power Test Code - Spark Ignition and Compression Ignition - Net Power Rating.* Rev: August 2004. Warrendale: SAE International.

Salam, Z. 2003. *DC Motor Drive.* [Online]. Available: http://www.scribd.com/doc/240632341/Problemas-Con-Motores. [2014, September 24].

Self-aligning ball bearings. [S.a.]. [Online]. Available: http://www.skf.com/africa/en/products/bearings-units-housings/ball-bearings/self-aligning-ball-bearings/index.html. [2015, March 29].

Shaw, B. [S.a.]. *Dynamometer = Dyno.* [Online]. Available: http://www.currysauto.com/services/curry-car-care-tips/dynamometer.aspx. [2014, January 29].

Smoke value measurement with the filter-paper-method. 2005. Application Notes. AT1007E, Rev: 02. June 2005.

Stone, R. 1992. *Introduction to Internal Combustion Engines*. Second Edition. London: MacMillan.

Van Basshuysen, R. & Schäfer, F. 2004. *Internal Combustion Engine Handbook.* Warrendale: SAE International. ISBN 0-7680-1139-6.

Why You Need an Engine Dynamometer. [S.a.]. [Online]. Available: http://www.pwrtst.com/news-and-articles/why-you-need-an-engine-dynamometer.htm. [2013, January 02].

Wlodarczyk, M.T. 2012. Fiber optic-based in-cylinder pressure sensor for advanced engine control and monitoring. [Online]. Available: http://www.combustion-engines.eu/entityfiles/files/articles_published/PTNSS-2012-SS4-401.pdf. [2016, August 05].

Wlodarczyk, M.T., Poorman, T., Xia, L., Arnold, J. & Coleman, T. 1998. In-Cylinder Fiber-Optic Pressure Sensors for Monitoring and Control of Diesel Engines. [Online]. Available: http://www.optrand.com/Papers/sae98/sae98paper.htm. [2015, June 08].

Woschni, G. 1967. A Universally Applicable Equation for the Instantaneous Heat Transfer Coefficient in the Internal Combustion Engine. *SAE paper* 670931.

Yanmar Industrial Engines - Operation Manual. [S.a.]. [Online]. Available: http://powerlite.com.au/wp-content/uploads/Yanmar_Engine_L48N_L100N_User_Manual.pdf. [2012, February 16]

Yanmar L100N Performance Curves. [S.a.]. [Online]. Available: http://www.powerequipment.com.au/wp-content/uploads/2014/05/l100n-performance-curve.pdf. [2016, August 14].

Zhoa, H & Ladammatos, N. 2001. *Engine Combustion Instrumentation and Diagnostics*. United States: SAE International. ISBN 0-7680-0665-1.